Brittle faulting and fluid flow in basement rocks of coastal Otago (South Island, New Zealand)

Madison Frank

a thesis submitted for the degree of

Master of Science

at the University of Otago, Dunedin,

New Zealand.

May 3, 2016

Abstract

Fault and fracture networks in foliated basement rocks control the strength, fluid flow properties and seismogenic behaviour of the crust in many areas worldwide. Understanding faulting patterns in foliated basement rocks is important because much seismicity (e.g. in the south island of New Zealand) occurs within basement rocks and basement faults are commonly linked to the formation of major ore bodies (e.g. in central Otago). Strongly foliated schists (and greywackes) are well exposed across extensive, clean outcrops along coastal sections in Otago, providing an important opportunity to study the nature of brittle deformation and faulting in the outboard region of the Otago reverse-fault province. Furthermore, it offers an opportunity to evaluate the extent to which pre-existing anisotropy in the basement schist (foliation and joints) has influenced the patterns of brittle deformation along the coastal platform.

Using high-resolution aerial photography, lineaments (n=6625) with lengths of ∼3 m to c. 200 m were mapped along the 16.5 km-long coastal platform between Taieri Mouth and Chrystalls Beach, Otago. Significant patterns noted in the lineament data include strong preferred orientations trending 50-70°and 120-140°. Comparison to regional-scale faults in the Otago region (as recognised on GNS QMAP) shows a strong correlation between the coastal lineaments trending 120-140°and a set of NW-SE striking regional faults. However, many faults in the Otago region, including the nearby Akatore Fault, trend NE-SW (30-40 ± 10°), an orientation that is conspicuously absent in our coastal lineament analysis.

Detailed structural mapping has showed that SE-NW (120-140°) lineaments correspond to first-order faults (≤ 2 m wide) hosting breccias and small

sinistral strike-slip faults that nucleated on continuous, planar, steeply-dipping joints. The latter are associated with paired quartz-calcite veins and small breccia pods developed in dilational jogs between adjacent joint tips. ENE-WSW (50-70°) lineaments correspond to a second (often dextral) strike-slip fault set hosting thin, continuous breccia layers formed within intact schist. Both fault sets host shallowly plunging lineations and form a conjugate set. Inversion of kinematic indicators, primarily from the conjugate fault set, indicates the paleostress field during faulting was similar to the modern-day stress field in Canterbury and Otago, characterized by subhorizontal σ_1 trending c. 114°and subvertical σ_2, i.e. a strike-slip stress regime. From this, we infer that the faults are post-Miocene (< 25 Ma) in age and formed in the modern-day stress regime.

From cross-cutting relationships in the field and thin section, relative chronology of formation can be inferred as follows; 1) establishment of a slaty cleavage during Jurassic metamorphism, 2) formation of a joint network during Late Cretaceous exhumation of the schist, 3) reactivation of exhumation joints in the past 25 Ma as conjugate SE-NW (sinistral) and E-W (dextral) striking faults hosting quartz and calcite veins and breccias, 4) opening of extensional fractures parallel to foliation and precipitation of fibrous calcite veins, and 5) deposition of botryoidal calcite in unconfined voids.

Estimated depth-temperature conditions of faulting during stages 3 – 5 above are ≤ 2 km and $\simeq 50$ °C. Calcite veins and calcite-bearing breccia matrix formed during these stages show wide ranging δ^{18}O and δ^{13}C values that are paired with tightly clustered ^{87}Sr/^{86}Sr values of $\simeq 0.7062$. A decoupled fluid model is proposed where shallow fluids circulating down through the Cenozoic sedimentary sequence interacted primarily with limestone and a smaller volume of fluid interacted with coal to acquire a mixture of δ^{13}C values with relatively heavy δ^{18}O values. ^{87}Sr/^{86}Sr values may reflect the breakdown of Ca-rich (low ^{87}Rb) minerals in the schist.

The orientations and kinematics of the basement fault fabric documented in coastal Otago mimics aspects of the faulting pattern from the 2010-2011 Canterbury earthquake sequence documented from seismological data. In particular, dextral E-W striking strike-slip faults (e.g. the Greendale Fault) ruptured during the Canterbury earthquake sequence and SE-NW

striking sinistral strike-slip faults are inferred from aftershock alignments. In addition the Darfield mainshock nucleated on a steeply dipping, NE-SW striking reverse fault similar to several regional Otago faults. Our observations therefore suggest that there may be a common basement fault fabric developed throughout Otago and Canterbury that plays an important role in controlling earthquake sequences developed within the contemporary stress field.

Graphical abstract

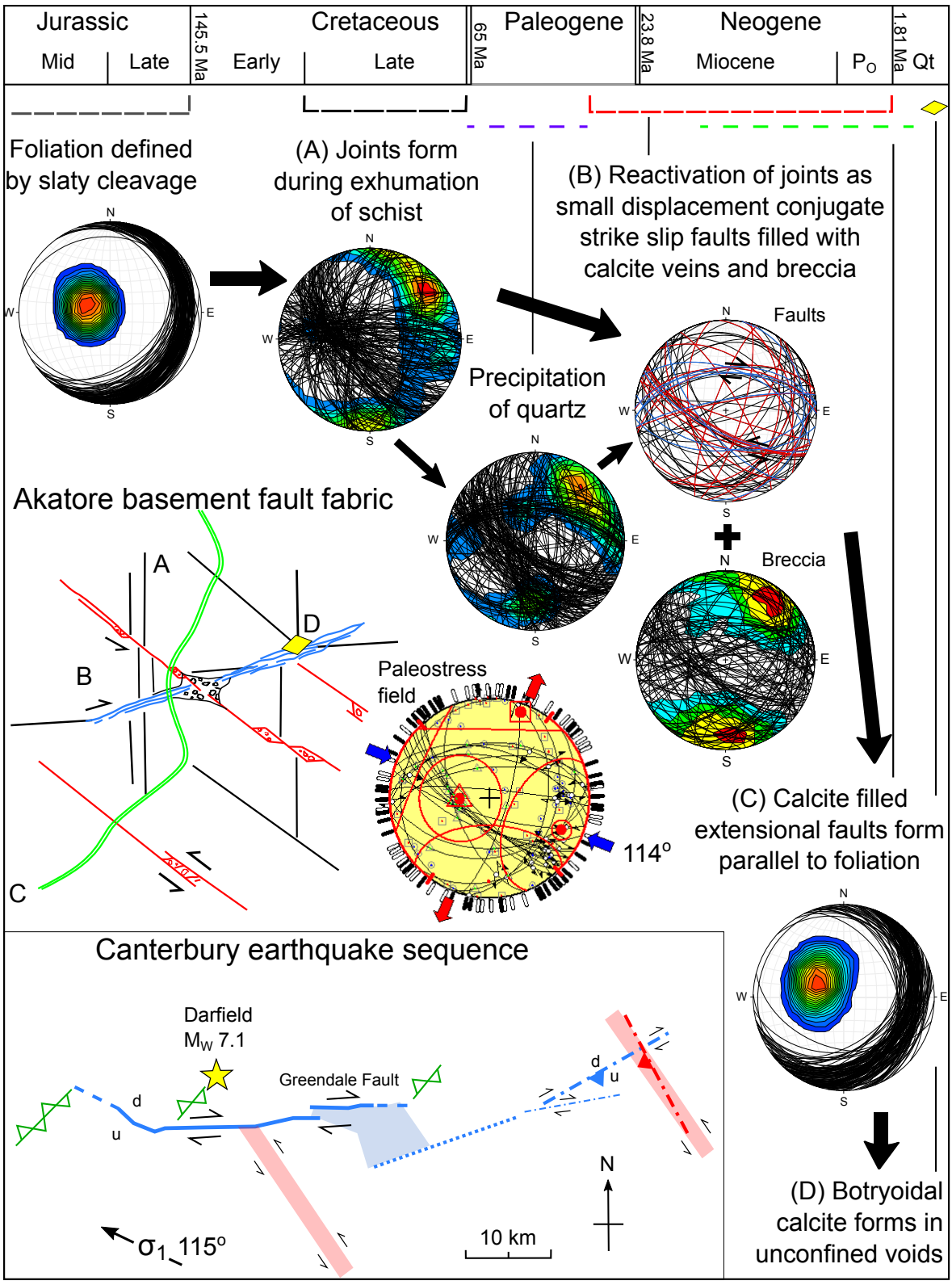

Acknowledgements

Thank you to the many people who helped me through this thesis;

Braden Mitchell for allowing access to the field site through his property. Nick Mortimer for getting me started with early resources and a field introduction to the regional geology. Luke Easterbrook for proving that problems with LaTeX and ArcGIS can always be solved. And, along with Hamish Bowman, for their patience and technical support despite the multitude of programs I insisted on trying. Christina Riesselman, Daphne Lee, Dave Craw, Dave Prior, James Scott, and Jon Lindqvist who all provided advice and resources when I decided to dabble outside the field of structural geology. Mike Palin for his support, assistance, and advice with my foray into the world of geochemistry. The one and only Katrin Wellnitz for help with isotope data collection and modelling. For patiently answering all my geochemistry questions, and then going through it again every time I forgot! My fellow geology students for all the help, discussion, and encouragement over tea. My friends and family around the world for the laughter, commiseration, and distractions! Jack, for making certain I did more than just procrastinate, for all of his encouragement and support, and for adjusting his plans to accommodate being dragged across the country so I didn't have to do this alone. And finally my supervisor Steve Smith for his untiring patience, assistance, and conviction that things were never quite as bad as I imagined them.

Contents

List of Tables

List of Figures

Chapter 1

Introduction

The structure and network characteristics of brittle fault zones in the middle- to upper-crust are topics of intense ongoing research. Mid- to upper-crustal fault zones in basement rocks control the strength (Suppe, 2007; Townend and Zoback, 2000), architecture (Gracia *et al.*, 2003; Mortimer *et al.*, 2002), fluid flow properties (Sibson, 1994; Townend and Zoback, 2000) and seismogenic potential (Ghisetti and Vezzani, 2002; Sibson, 1989; Valoroso *et al.*, 2014) of the crust. In particular, the coupling between brittle fracture and fluid flow has profound implications for understanding crustal earthquake sequences and the nature of hydrothermal mineralization (Sibson, 1987, 1992, 1996). Furthermore, host rock properties may have significant influence on both fluid flow in brittle fracture zones (Faulkner and Armitage, 2013) and patterns of faulting (Butler *et al.*, 2008; Yin and Ranalli, 1992). Classic Andersonian faulting models have long been used to describe fault mechanics but studies have shown that, in strongly anisotropic rocks, the kinematics and evolution of faults may follow non-Andersonian stress states (Lacombe *et al.*, 2013; Yin and Ranalli, 1992). Patterns of brittle deformation should therefore reflect the effect of pre-existing anisotropy on fault zone characteristics and must be considered when evaluating potential seismic hazard and further evolution of the fault system.

The geology of New Zealand, particularly the South Island, is dominated by basement schist and greywacke that host complex faulting patterns (Beanland and Berryman, 1989; Craw and Norris, 1991; Fagereng, 2011a; Mortimer, 2004). Understanding these faulting patterns in the basement rocks of this area is critical for several reasons: 1) reactivation of basement faults influences the patterns of faulting in overlying cover sequences (Higgins and Harris, 1997; Saltzer and Pollard, 1992). 2) Basement faults are linked to the formation and timing of major ore bodies in central Otago, most

notably gold ores (Higgins and Harris, 1997; Pitcairn *et al.*, 2006). 3) Most seismicity in the South Island of New Zealand - including the destructive 2010-2011 Canterbury earthquake sequence (Ghisetti and Sibson, 2012; Sibson *et al.*, 2011, 2012) - occurs within basement rocks, thus understanding fault zone processes and associated fluid flow is important to seismic hazard analysis in New Zealand (Dorn *et al.*, 2010).

Despite the importance of basement faulting in New Zealand, there have been few studies performed with the aim of establishing a detailed structural framework of faulting patterns in regional basement rocks. The purpose of this project is to develop such a framework including, but not restricted to: dominant fault orientations, kinematics, slip histories, cross-cutting relationships, fault rock associations and fluid flow histories. The study region is composed of greywacke and schist exposed across extensive, clean outcrops along coastal sections in Otago (south of the city of Dunedin). The site is thus an ideal place to characterize brittle faulting and fluid flow in New Zealand's dominant, strongly anisotropic basement rocks.

A number of important scientific questions will be addressed throughout the project, including: what are the sources of fluids in basement rocks of coastal Otago? How does pre-existing anisotropy (e.g. foliation) influence brittle faulting? Do brittle faults in exhumed mid- to upper-crustal basement rocks represent ancient seismic slip events? Does fault structure and mineralization depend on fault orientation? And what role, if any, could basement fault fabric play in Otago seismicity?

Chapter 2

Background Geology

2.1 Field Area

The study region for this project is located in the Otago region (Fig. 2.1), 40 km south of Dunedin city, and extends roughly 16 km along the coast from Taieri Mouth (WGS84 170° 12' 7.965" E, 46° 4' 11.08" S) to Chrystalls Beach (WGS84 170° 6' 37.104" E, 46° 11' 29.713" S) hereafter described as the "Akatore coast" (after Akatore Creek). This area was chosen due to the clean expanse of basement Otago Schist exposed across the coastal platforms. This coastal section runs approximately parallel to the active Akatore reverse fault for most of the section until the fault travels offshore at Taieri Mouth (Fig. 2.2).

2.2 Regional Geology

2.2.1 Basement Terranes

Basement rocks of the Otago region, and much of the Eastern Province, include greywacke and schist belonging to the Rakaia (Torlesse composite) and Caples tectonostratigraphic terranes with minor belts of Dun Mountain-Maitai, and Murihiku terranes (GNS, 2012; Mortimer, 2004). These terranes were deposited during the Permian to Late Triassic (Adams *et al.*, 2007; MacKinnon, 1983; Mortimer, 2004) and then progressively accreted along the Gondwana margin during the Mid Jurassic (Mortimer, 2004) to Early Cretaceous (Gray and Foster, 2004). The quartzofeldspathic, turbidite-rich Rakaia Terrane formed from deposition along an active continental margin while the remaining terranes, including the Caples, are derived from a volcanic island arc

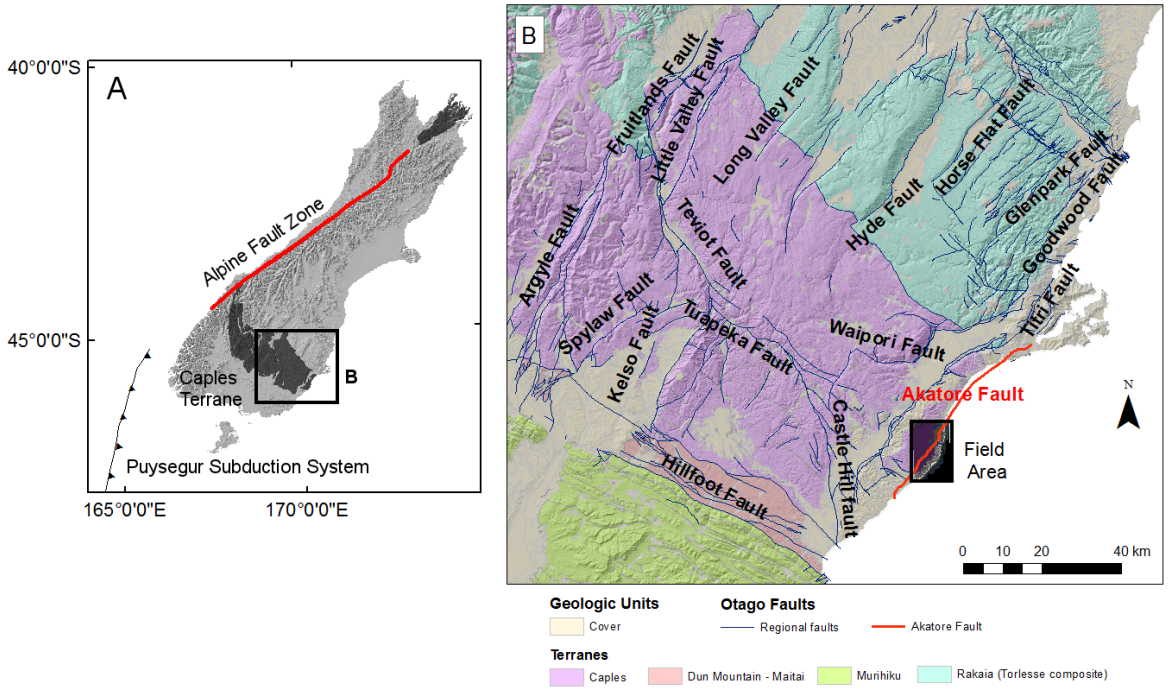

Figure 2.1: A) Geological setting of New Zealand showing the Caples Terrane (dark grey), B) geologic and tectonic setting of the Otago region.

and are dominated by different volcanoclastics (MacKinnon, 1983; Mortimer, 1993, 2004). The study region lies within a unique section of the Caples Terrane known as the Chrystalls Beach Complex (Fagereng, 2009) and is bounded by the Caples-Rakaia suture zone to the NE and the Livingstone Fault to the SW (Fagereng, 2009; Fagereng and Cooper, 2010a; GNS, 2012). It represents the back-most section of the Caples-Rakaia accretionary prism with the Livingstone Fault as the accretionary wedge backstop (Mortimer, 2003).

Metamorphic overprinting seen in the sections of the Caples and Rakaia terranes adjacent to the Caples-Rakaia suture zone, including the study region, indicate the area has undergone low grade metamorphism and deformation. The metamorphic equivalent of the Caples and Rakaia terranes have historically been recognized in literature as the Haast Schist Terrane (MacKinnon, 1983), and more recently as the Otago region part of the Haast schist belt known as the Otago Schist (Fagereng and Cooper, 2010a; Mortimer, 1993, 2004). The Otago Schist displays gradational metamorphism from prehnite-pumpellyite facies to greenschist facies but is lithologically monotonous so changes in metamorphic grade are generally distinguishable only by geochemical changes (Bishop, 1972; Mortimer, 1993; Turnbull *et al.*, 2001). It is instead mapped using a metamorphic texture scale from Textural Zone 1 (TZI), unfoliated greywacke,

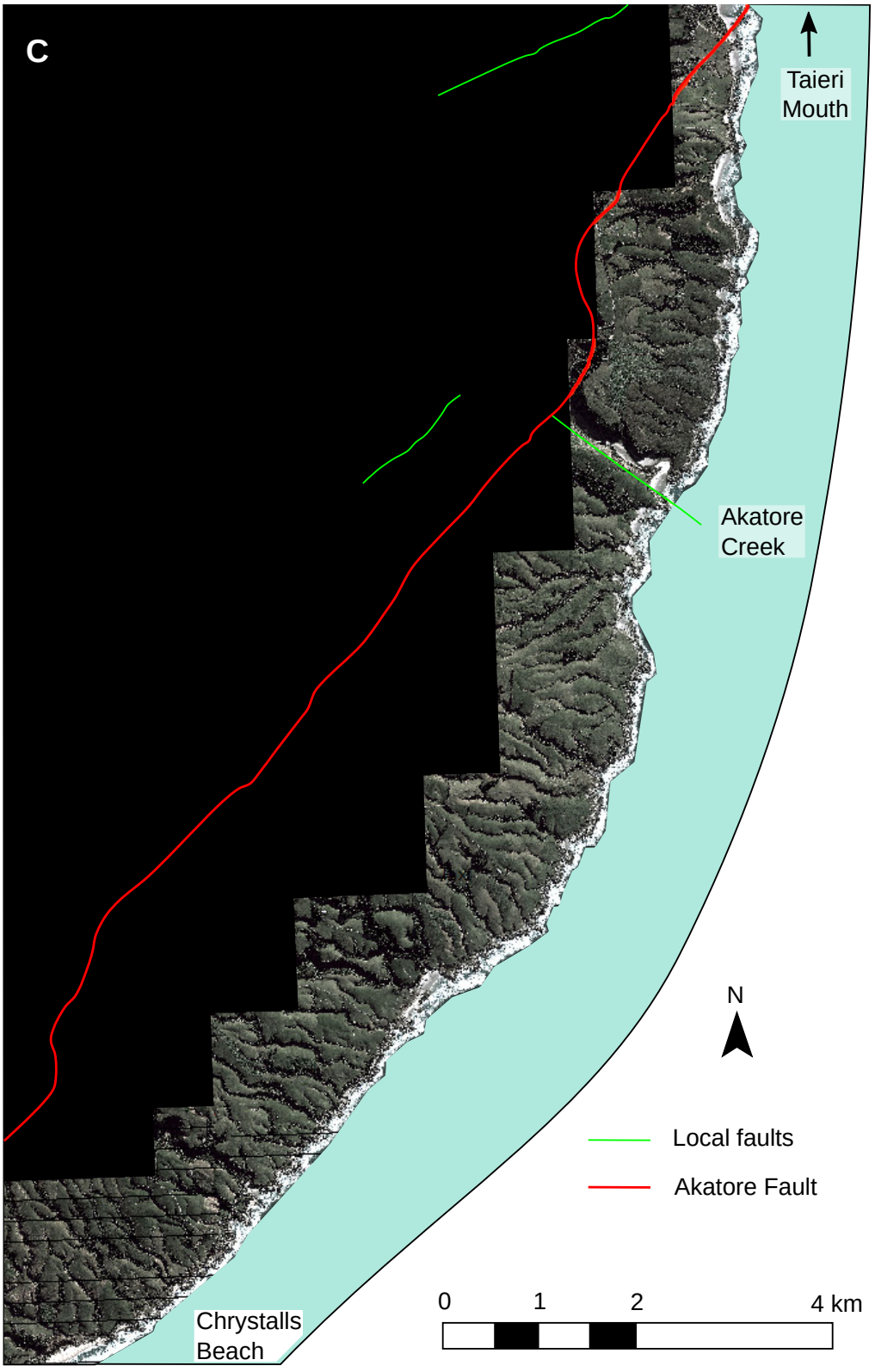

Figure 2.2: Map of the field region (the Akatore coast) and local faults including the Akatore Fault (red).

to Textural Zone 4 (TZIV), "pervasively foliated schist with ubiquitous, laterally continuous, mineral segregation veins" (Fagereng, 2009; Mortimer, 1993; Turnbull *et al.*, 2001). Metamorphic temperatures are estimated to have reached up to a maximum of 350-410°C (Gray and Foster, 2004; Mortimer, 2000) during the Middle to Late Jurassic (Adams and Robinson, 1993; Adams and Graham, 1997; Nishimura *et al.*, 2000) with metamorphism continuing into the Early Cretaceous (Gray and Foster, 2004; Nishimura *et al.*, 2000).

Broad folds denoting the Otago antiform and Taieri-Wakatipu synform can be seen across east Otago from changes in subhorizontal foliation. Variations in metamorphic grade across the Otago antiform indicate this fold was post-metamorphic while constant metamorphic grade across the Taieri-Wakatipu synform indicate pre- or syn-metamorphic folding (Fagereng, 2009, 2011a; Mortimer, 1993, 2003). Deformation occurred during Mesozoic thickening of the accretionary wedge (Mortimer, 2003) and was followed by relatively rapid exhumation of the Otago Schist by extension and normal faulting (Fagereng, 2011a; Mortimer, 1993, 2003) through the Early Cretaceous, and again during the Middle Eocene-Oligocene extension related to the Moonlight Tectonic Zone and affiliated extensional faults (Fagereng, 2009; Norris and Turnbull, 1993). Exhumation throughout this period was accompanied by extensive mineralization (Haast Schist overprint) mainly in vein systems (Craw and Norris, 1991). With initiation of the Alpine Fault in the Early Miocene the region experienced compressional inversion forming reverse faults in the Otago Schist (Norris *et al.*, 1990) and reactivating normal faults from the Cretaceous extensional regime as high-angle reverse faults (Fagereng, 2009; Norris and Turnbull, 1993). The Otago Schist has continued to undergo deformation related to convergence on the Alpine Fault up to present day.

2.2.2 Chrystalls Beach Complex

Akatore Coast lies within a unique section of the Otago Schist known as the Chrystalls Beach Complex. The Chrystalls Beach Complex contains some of the oldest rocks of the Otago Schist but does not correlate well with neighbouring Caples or Rakaia Terrane rocks; it is interpreted as either an atypical sequence of the Caples Terrane or having sourced sediments outside of the nearby terranes (Fagereng, 2011a; Fagereng and Cooper, 2010b). The complex is dominated by TZIIa schist and, in the vicinity of Chrystalls Beach, has a unique texture comprised of floating cohesive sandstone blocks in an intensely sheared mudstone matrix (Fagereng, 2009; Fagereng and Cooper, 2010a; Fagereng, 2011b,a). This section has been interpreted as a shear zone within

or at the base of an accretionary melange that experienced concentrated deformation and fluid flow due to subduction under the Gondwana margin during the Jurassic (Fagereng, 2009; Fagereng and Cooper, 2010a). It is uncertain exactly how far NE along the Akatore coast the Chrystalls Beach Complex extends as the distinctive texture of Chrystalls Beach lenses out before Akatore Creek. The entire complex exhibits overprinting by later stage vein and fracture networks (Fagereng and Cooper, 2010a) which are the focus of this study.

2.3 Neotectonic history

The continuing active deformation related to plate convergence across the South Island has formed what is described as the Otago reverse fault province within the Otago region. This province displays typical basin and range morphology (Beanland and Berryman, 1989; Berryman and Beanland, 1991) and contains a suite of NE and SE striking faults, several of which are currently considered active (Beanland and Berryman, 1989; Litchfield, 2001; Litchfield and Norris, 2000). Faults in this province are characterized by intermittent seismic behaviour with episodic bursts of activity resulting in sub-equal slip increments occurring between periods of extended quiescence (Berryman and Beanland, 1991). Recurrence intervals of individual faults and fault systems in the Otago Region vary between several to tens of thousands of years (Beanland and Berryman, 1989; Berryman and Beanland, 1991). Kinematically the region is dominated by high angle reverse faults dipping northwest, including reactivated pre-existing extensional structures, connected at 10-15 km depth to an imbricated basement decollement zone that accommodates overall shortening from plate convergence (Fig. 2.3; Beanland and Berryman, 1989; Litchfield, 2001; Norris *et al.*, 1990).

The Akatore Fault represents the easternmost onshore member of the leading edge of the Otago reverse fault province. Offshore faults parallel to the Akatore Fault have been imaged in geophysical surveys (Litchfield and Norris, 2000). The Akatore Fault strikes NE-SW and lies immediately west of the Akatore coast. The Akatore and Titri faults both dip steeply to the southeast forming antithetic faults to the decollement zone (Fig. 2.3 Litchfield, 2001). Paleoseismic studies show that the Akatore Fault has hosted at least two ruptures during the Holocene, at post-3800 yr before present and 1150-1000 yr before present, each accommodating an average of 3 m displacement (Litchfield and Norris, 2000). The Titri, Akatore, and offshore faults parallel to the Akatore Fault are inferred to extend into the Dunedin urban area, onshore and offshore respectively,

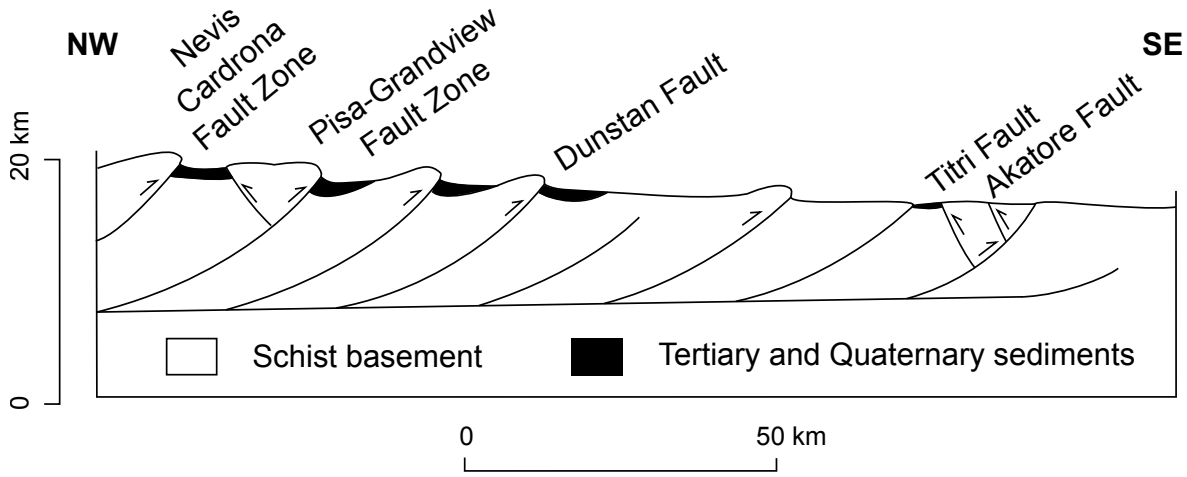

Figure 2.3: Cross section of the Otago reverse fault province from Beanland and Berryman (1989) showing the imbricated nature of large reverse faults in the basement schist of the Otago region.

representing potential near-source seismic hazard to Dunedin City (Glassey *et al.*, 2003; Litchfield and Norris, 2000). The Dunedin Earthquake, a magnitude 5.0 event in 1974, resulted in widespread minor damage to the city that was concentrated in areas of deep alluvium and/or reclaimed land (Bishop, 1974). The earthquake is believed to have been hosted on either the Akatore Fault or, more likely, on the offshore Akatore-parallel faults (Bishop, 1974; Glassey *et al.*, 2003). Models of future ruptures show that these faults may host up to magnitude 7 earthquakes (Glassey *et al.*, 2003).

Chapter 3

Methodology

This chapter describes the various methodologies used to collect, prepare, and analyse the different datasets used during this project.

3.1 Lineament Analysis

Lineaments were picked from high resolution (∼0.5 m) aerial photography images. Lineament picking was done in ArcGIS using a polyline shapefile. Linear features within solid rock sections of the coastal platform were traced using straight lines. Curving or kinked features that were recognized as a single lineament were traced using a number of line sections. Lineaments within solid rock were preferentially picked, whereas lineaments that extended beyond the edges of shore platform sections (either out to sea or inland) were not selected unless they continued into a lineament identified on the solid rock platform. Open channels across shore platforms were defined by two lineaments, one at each edge of the channel except in cases where the channel aperture was relatively narrow or where one side of the channel could not be defined due to shadow. Lineaments were not continued through sand or open water except in cases where the adjacent rocky section was relatively close and the feature had a strong expression with excellent linear correlation. Consideration was given to topographic changes, where possible linear features perpendicular to incised sections of hillside were selected as well as linear features aligned with the edges of more broad slip features in the hillside. In sections of the coastal platform where the texture of the schist was highly fractured (cross-hatched appearance) lineaments were required to pass through at least one section of texturally smoother schist. In the case of uncertainty due to intense shadow effects in narrow aperture channels, adjacent weaker lineaments of

similar orientation were chosen instead.

The complete dataset from coastal rock exposures includes 6625 lineaments. Once all lineaments had been picked, orientation was determined using the ArcGIS spatial statistics tool "linear directional mean" (LDM). LDM is calculated as

$$LDM = \arctan \frac{\sum_{i=1}^{n} \sin \Theta_i}{\sum_{i=1}^{n} \cos \Theta_i} \tag{3.1}$$

where Θ_i are the directions of polyline features from a single origin. No directional data was assigned to lineaments so the range of possible orientations is restricted to 0-180°. Nearby active and inactive faults in the Otago region, including the Akatore Fault, were identified and selected from the GNS QMAP database and LDM for these features were also calculated.

Lineaments orientations in different regions along the coast were analysed by subdividing the total lineament dataset in two different ways: 1) by subdividing a line roughly parallel to the coast that was broken into 10 segments of equal length (10 x 1.64 km length of coastline), and 2) by using natural breaks in the coastal platform, typically corresponding to large inlets or bays.

Lineament attributes were imported into the statistical modelling program R for analysis. Rose diagrams of lineament orientation were created using the circular package with a bin size of 10°. Rose diagrams are displayed using the convention that segment radius is linearly related to relative frequency (modifier *radii.scale="linear"* within the *rose.diag()* call), allowing the radii of segments to be directly compared in order to assess relative frequency (Pewsey *et al.*, 2013). See appendix A for all R code.

Two sets of rose diagrams were generated for i) the complete lineament dataset in each region and ii) all lineaments > 30 m in length in each region. Lineaments > 30 m in length were chosen under the assumption that continuous lineaments could be picked with greater confidence and thus offer a way to remove the background "noise" potentially introduced by shorter lineaments. Each rose diagram set (presented in Chapter 4) includes; all lineament orientations, lineaments grouped by natural breaks in the coastal platform and lineaments grouped in to 1.64 km long segments. A rose diagram of Otago regional faults was also generated.

3.2 Digital Field Mapping

Given the huge variety of hardware and software available for digital fieldwork, from professional geoscientist tools to generic open-source mobile apps, a pilot study was undertaken to evaluate the individual benefits, disadvantages, and capabilities of a variety of hardware/software combinations. Six hardware/software combinations were tested during the course of the pilot study (Table 3.1);

Table 3.1: List of the software and hardware combinations tested.

Software	**Source**	**Hardware**
ArcPad	ESRI	Toshiba tablet
FieldMove	Midland Valley	Toshiba tablet
Geopaparazzi	Open source	Samsung tablet
Collector	ESRI	Samsung tablet
ArcPad	ESRI	Nomad unit
TerraSync	Trimble	GeoExplorer (GeoXT) unit

The study was conducted on coastal platform segments where key fault rock assemblages were noted in earlier reconnaissance. (See Appendix C for full discussion of individual hardware and software performances.)

3.2.1 Set-up and processing

Local aerial photograph basemaps were clipped from aerial photography of the entire field region in ArcGIS and exported as either TIFF or JPEG2000 files. A clipped shapefile of lineaments overlying local regions was also generated. These files were loaded as background files on all software packages being tested. Empty shapefiles of joints, foliation, lineations, faults, general points, and general line features were created and loaded along with a matching data dictionary for Terrasync.

Devices were trialled on coastal platform segments immediately north of Akatore Creek. Structural point measurements of joints, foliation, lineations and faults were taken. Associated photographs were taken to test the camera quality and ease of linking photographs to field sites. Sites were located using internal GPS readings and accuracy assessed by comparison to recognizable features on the aerial photography.

Collected data was then exported to a desktop computer through the necessary software before being converted back to ArcGIS shapefiles. For example, data collected

on Terrasync was uploaded to GPS Pathfinder Office, a differential correction applied, then exported to a shapefile for viewing in ArcGIS.

3.2.2 Hardware and software performance for digital mapping

See Table 3.2 for hardware specifications of each device, Table 3.3 for hardware performance, and Table 3.4 for software performance.

3.2.3 Pilot outcome

As shown in Tables 3.3 and 3.4, TerraSync on the GeoXT offers the best combination of hardware and software capabilities for this project.

The GeoXT unit, designed by Trimble, has a very ruggedized design including a waterproof and shock resistant case with built in hand straps, stylus, and keyboard. The unit is 23.4 x 9.9 x 5.6 cm. The display (10.7 cm) is excellent but the screen occasionally struggles with glare in full sun. The most significant feature with the GeoXT is the GPS accuracy with a reported accuracy of 0.75 m. In the field the unit was accurate to 0.2-0.3 m after differential GPS corrections.

Terrasync is specifically designed for mobile devices and can easily be adapted for any type of data collection. Set-up of a data dictionary prior to commencing fieldwork can be time intensive, however the process is relatively simple and intuitive. The Terrasync data dictionary offers an intelligent design where users can create nested fields based on 'either or' questions. There is no built in capability for creating new files in the field but generic point, line, and polygon fields are automatically generated and may act as a safety net. The program is also capable of including a photo field within feature generation automatically linking photos taken on the GeoXT to the correct data point.

Terrasync experiences some loss of efficiency when negotiating the various screens in the user interface. This is mostly negated by the fact that the GeoXT has such high locational accuracy that repeated verification of location on the basemap is unnecessary. With such confidence in the spatial accuracy a user may stay in the data collection screen for the majority of data collection and only deal with refreshing the basemap when comparison to imported features is desired.

The main aims of structural mapping in this project were to 1) collect orientation measurements from individual locations and 2) link these measurements to field photos and notes. Given the results of the software and hardware evaluation, Terrasync

Table 3.2: Comparison of the key features of the hardware devices that have been tested in the pilot study.

Device	Size (cm)	Screen Size (cm diagonal)	Battery Life (hrs)	GPS Accuracy (± m)	Weight (kg)
Windows 8 tablet	21.3 x 13.6 x 1.1	20.3	14	3*	0.43
Samsung tablet	21.3 x 12.5 x 0.7	21.4	12	3*	0.29
Nomad GPS	17.6 x 10.0 x 5.0	8.9	15	1-3	0.56
GeoXT GPS	23.4 x 9.9 x 5.6	10.7	10	0.75	0.925

* Generic minimum locational accuracy of smartphones and tablets from Shaner (2013)

Device	Storage (GB)	External Storage Capacity (GB)	Ruggedized	Orientation Sensors	Camera (MP)
Windows 8 tablet	32	64	N	Y	5
Samsung tablet	16	128	N	Y	8
Nomad GPS	6	Y	Y	N	-
GeoXT GPS	2	32	Y	N	5

* Y = yes, N = no, - = data not available

Table 3.3: Ranking using a scale of 1 (poor) to 5 (excellent) of some aspects of the hardware devices (e.g. user-friendliness) based on the experiences of the author during the pilot study.

Device	Developer	Operating System	Screen Size	Robustness	Efficiency	GPS Accuracy	Total
Encore Tablet	Toshiba	Windows 8	5	1	3	2	11
Galaxy Tablet	Samsung	Android 4.4	5	3	5	3	17
Nomad	Trimble	Windows Mobile 6.1	3	5	4	4	15
GeoXT	Trimble	GeoXT	3	5	5	5	**18**

Table 3.4: Ranking using a scale of 1 (poor) to 5 (excellent) of some aspects of the software devices (e.g. user-friendliness) based on the experiences of the author during the pilot study.

Developer	Software	Setup Time	User Interface	Efficiency	Versatility	Total
ESRI	ArcPad	1	1	2	5	9
Midland Valley	FieldMove*	5	1	3	1	10
geopaparazzi	Geopaparazzi	3	5	5	3	**16**
ESRI	Collector^{+}	1	-	-	5	6
Trimble	TerraSync	2	4	5	5	**16**

* FieldMove was unable to recognize the internal GPS unit in the field so only a few manually picked points were taken to test feature generation.

$^{+}$ The aerial photography basemap was not able to be uploaded to ArcGIS Online for use by Collector.

- Data not available

running on the GeoXT was the preferred software-hardware combination for fieldwork. This combination outstrips any of the competition in terms of usability and accuracy. The versatility, ruggedness, and high precision of the GeoXT offers users a degree of flexibility and confidence in data quality which is unmatched.

3.3 Field Data Acquisition

All field data were collected using TerraSync on the Trimble GeoXT. Prior to fieldwork, background files of aerial photography and GIS-derived lineaments (see above methodology and Chapter 4) were uploaded and a data dictionary was set up using GPS Pathfinder Office software.

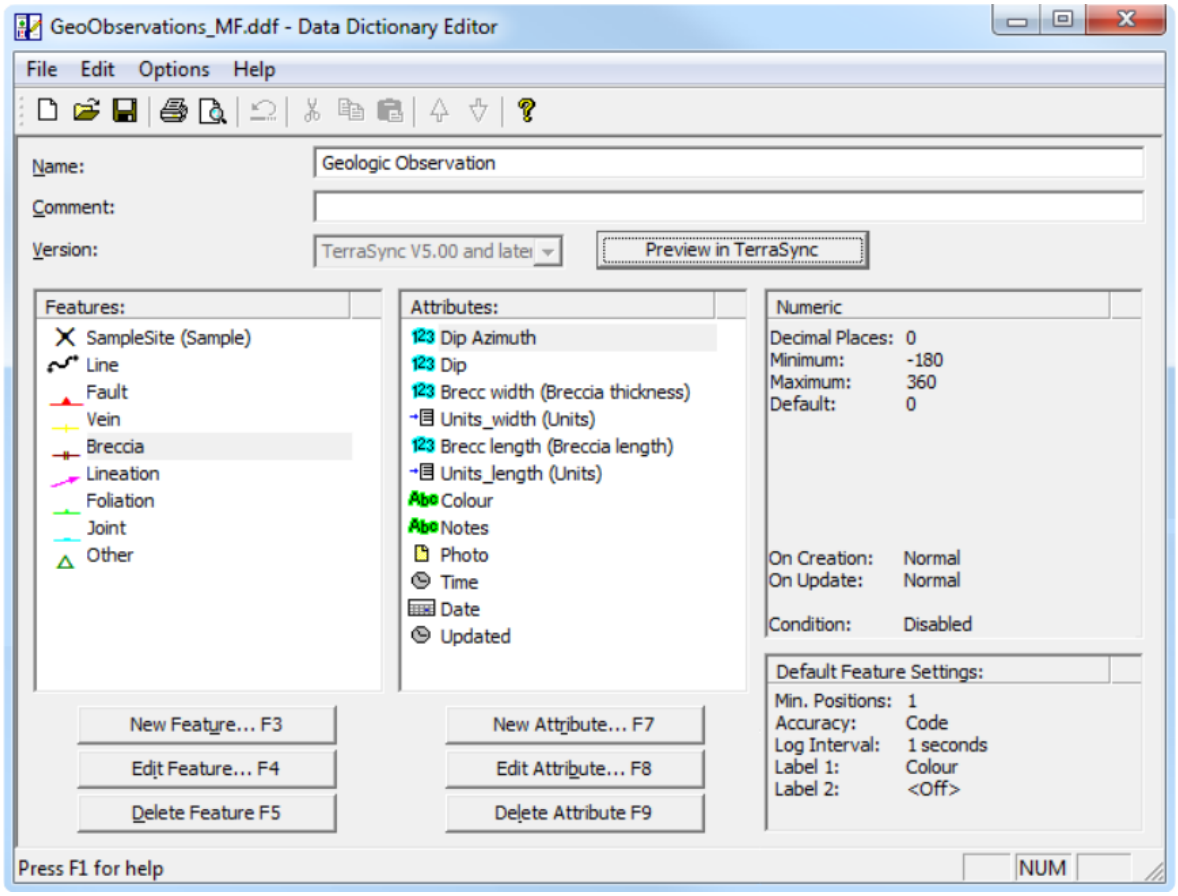

Figure 3.1: Final version of the TerraSync data dictionary used for fieldwork showing the attributes of a breccia feature.

The data dictionary included 9 features that were measured in the field; sample site, fault, vein, breccia (Fig. 3.1), lineation, foliation, joint, general 'other' (all point features), and general 'line' feature. A set of standard attributes was created for every

feature including orientation (dip/dip azimuth for planar features and plunge/trend or rake for linear features), notes, and associated photos. The time, date and update time were automatically logged on feature generation and modification respectively. Unique attributes for features included vein material (quartz, calcite, both, or other), breccia dimensions (length and width) and colour, and the type of lineation (slickenline, slickenfibre, or other). For fault and line features a set of nested attributes were used, the fill type (vein, breccia, vein and breccia, or joint) was required and, depending on the type of fill selected, attributes for vein material and/or breccia dimensions would appear. In later iterations fault features also included the nested option to include a lineation attribute that would then lead to the lineation attributes. Depending on the requirements of individual field days the full merged dataset of specific features was uploaded as background files onto the GeoXT (e.g. if the focus of fieldwork was to collect lineation measurements then a background file showing all fault and lineation features collected to date was uploaded).

Data collected on the GeoXT was downloaded into GPS Pathfinder Office and differentially corrected using the Land Information NZ continuous GNSS base station located at the Otago University Survey School. The differential correction process automatically selects the better position from the carrier and code solution using smart automatic rover filtering and re-correcting real time positions. The corrected file was then exported as a shapefile for analysis in ArcGIS. The data dictionary was updated six times during the period of field data collection. Data collected using previous data dictionary iterations was updated to the most recent format and merged into a master shapefile in ArcGIS using the Merge (Data Management) tool.

3.4 Microstructural Analyses

3.4.1 Thin section preparation

All thin sections were prepared at the University of Otago with assistance from Brent Pooley. Rock samples were cut perpendicular to vein boundaries and hand polished with 600 μm grit. Polished samples were glued to glass slides using epoxy resin before being re-cut and polished down using 3 μm and 1 μm grit. Final slide thickness was approximately 30 μm.

3.4.2 Scanning electron microscopy

Thin sections for use in the scanning electron microscope (SEM) were polished and coated with a 10 nm thick layer of carbon prior to analysis. Scanning electron and energy dispersive spectroscopy (EDS) analyses on the SEM were done using 15 kV accelerating voltage, a working distance of 6.5 - 8.5 mm, and 120 micron aperture. Beam performance was calibrated before EDS analysis using a cobalt standard. Images and EDS data were collected, processed and analysed using the Aztec software package.

3.4.3 Cathodoluminescence

Cathodoluminescence (CL) analysis of thin sections was performed in the University of Otago's optical darkroom using a cold cathode system in conjunction with an optical microscope. Samples were imaged within a vacuum with voltage $\simeq$ 20 V using an electron beam with current $\simeq$ 600 kV.

3.5 Geochemical Analyses

3.5.1 δ^{13}C and δ^{18}O isotopes

Thirty-one samples of fault-related calcite veins and breccia fill (described in Chapter 5) were selected for carbon and oxygen isotope analysis in the Isotope Ratio Mass Spectroscopy Unit laboratory, Department of Chemistry, University of Otago. Calcite rich zones in each sample were targeted for crushing. Calcite grains were hand-picked and ground to $< 100\ \mu m$ using a mortar and pestle then weighed and placed in a sealed "exetainer" vials. Samples of pure carbonate (including standards) were weighed to $200 \pm 20\ \mu g$, the weight for 'dirty' samples was adjusted relative to the percentage of non-calcite material to ensure a constant carbonate:total sample ratio. Ideally this would ensure that the signal intensity was consistent across all samples. Samples were also duplicated in order to test the homogeneity of each sample.

Air was flushed from the closed vials with helium by a Thermo "GasBench" automated preparation system then samples were covered by anhydrous 104 % phosphoric acid by Katrin Wellnitz. Acid and carbonate were reacted for 24 hours at 23°C to form carbon dioxide. Ten replicate 100 μl aliquots of the CO_2+helium headspace were injected into a Thermo Advantage stable isotope ratio mass spectrometer (IRMS) bracketed by pulses of CO_2 monitoring gas. The raw delta values of the 10 sample injections, were filtered by removing any result more than one standard deviation from

the mean. The mean of the filtered raw deltas were normalised to international delta scales using three standard carbonate materials measured at the beginning and end of each batch of samples; drift control materials were analysed at every 12th position. The standard materials were used to correct the raw delta values (vs. monitoring gas) to the international scale (vs. VPDB and VSMOW) by 3-point calibration; the drift control material was used to calculate instrumental drift per unit time by linear regression. The standards were comprised of an international standard (NBS-18) and two laboratory standards (UCL-BORBA and IRU-Marble) which have been repeatedly standardised against international standards (Table 3.5). Initial processing and corrections were overseen by Robert Van Hale who also flagged any anomalous data points. [Hale 2014]

Table 3.5: Standards and the respective accepted isotopic values used to correct Akatore samples to the international $\delta^{13}C$ (PDB) and $\delta^{18}O$ (SMOW) scales.

	$\delta^{13}C_{PDB}$, ‰	$\delta^{18}O_{SMOW}$, ‰	Mineral
NBS-18	-5.01 ± 0.03	-23.01 ± 0.22	Calcium carbonate
UCL-BORBA	2.89 ± 0.04	-6.15 ± 0.09	Calcium carbonate
IRU-Marble	2.14 ± 0.10	-2.41 ± 0.27	Calcium carbonate

3.5.2 Trace elements

Seven of the samples analysed for carbon and oxygen isotopes were selected for analysis of trace elements. Calcite rich zones in the original whole rock sample were selected and chips of > 2 mm width were placed in two epoxy mounts. The mounts were then polished to expose the sample surfaces by Brent Pooley.

Trace elements analysis was performed in the Centre for Trace Element Analysis laboratory, Department of Chemistry, University of Otago using the laser ablation inductively coupled plasma mass spectrometer (LA-ICP-MS). Two standards, a glass standard from the National Science Foundation and a standard of compressed carbonate grains, were analysed before, midway, and after the Akatore samples. Laser ablation was conducted at 10 Hz using a spot diameter of 75 μm. Ablated material was then transferred from the LA chamber to the ICP-MS using He gas. The ICP-MS analyses background levels for the first 20 s of each run before firing the laser. Three tracks were taken on each sample for roughly 40 s (200 μm track length) as well as 2

long runs on sample AK-34 (a fibrous calcite); one approx. 620 μm long parallel to fibre direction and the second approx. 346 μm long perpendicular to fibre direction.

3.5.3 $^{87}Sr/^{86}Sr$ isotopes

The same seven samples mounted in epoxy blocks for trace element analysis (above) were analysed for $^{87}Sr/^{86}Sr$ isotope analyses. As with trace element analysis, samples were analysed at the Centre for Trace Element Analysis laboratory, Department of Chemistry, University of Otago using a multi-collector ICP-MS under the supervision of Dr. Mike Palin. The six collector chambers collected atomic masses 84 - 89. A Tridacna (marine clam shell) standard was analysed between Akatore samples as well as before and after the full sample suite. Five tracks per sample were ablated at 10 Hz using a spot diameter of 90 μm over 450 μm ($\sim$ 90 s). A 2 Hz pre-ablation run was conducted prior to sample ablation to clean the sample surface and check variations in ^{88}Sr signal strength. Cleaning runs were followed by a 20 s delay before ablation, if signal strength was too high ($^{88}Sr > 20$ V) or low during pre-ablation the spot size was adjusted at this time. ^{88}Sr signal strength was too high for the second and third tracks from sample AK-34 and all tracks from sample AK-24, spot size for these runs was reduced to 50 and 75 μm respectively. Signal strength was too low for the first and fifth track from sample AK-34 and spot size was increased to 130 μm for these runs. Empty runs to re-zero background electron noise in each collector chamber were performed before beginning $^{87}Sr/^{86}Sr$ analysis and after any samples with signal strength greater than the detector limit.

Data was processed with assistance from Dr. Mike Palin. Data processing aims to correct for radiogenic decay of ^{87}Rb to ^{87}Sr and the overlap of ^{87}Rb and ^{87}Sr peaks in the mass 87 collector chamber by using the ^{85}Rb trend to infer the ^{87}Rb trend. A subset of each full run with a MSWD < 3 (or MWSD < 5 in runs with $^{88}Sr \geq 10$ V) was selected for use. The signal from pre-ablation and regions within the selected subset that had very high ^{85}Rb signals (proportional ^{87}Rb signal were assumed to be within the ^{87}Sr signal) were excluded at this point. In addition to the MSWD values, the selected subset of data was evaluated using scatter of corrected $^{87}Rb/^{86}Rb$ compared a moving average and any changes in the $^{84}Sr/^{86}Sr$ ratio. Finally, the weighted average of the Rb corrected $^{87}Sr/^{86}Sr$ signal $\pm$ 2 s.e. was calculated for each run and age corrected for ^{87}Rb to ^{87}Sr decay.

Chapter 4

Lineament Analysis

Geomorphological lineaments are mappable patterns of naturally occurring linear features in an image that relate to the underlying architecture of the geology (Davis and Sampson, 2002; Hobbs, 1904; Hung *et al.*, 2005; O'Leary *et al.*, 1976). Multiple studies have shown that lineaments may be correlated to fault and fracture networks when considered in conjunction with the tectonic evolution of a region (Cortes *et al.*, 2003; Gabrielsen *et al.*, 2002; Hung *et al.*, 2005). Furthermore, in areas where reactivated basement faults are present, such as the Otago region, the fracture orientation in overlying sediments relative to the host fault can be linked to the host fault kinematics (Cortes *et al.*, 2003). Lineament patterns may therefore offer insight into the relationships between brittle deformation structures across the entire field region and also, when considered with regional faulting, give regional context to brittle faulting.

Analysis of lineament patterns can be undertaken with a variety of remote sensor imagery using manual or computer based automatic techniques. Lineament analysis of remote sensor imagery is a powerful technique for characterizing large areas given the wide ground coverage and relatively high resolution of images taken by modern instruments including satellite imagery, LiDAR, and aerial photography (Suzen and Toprak, 1998). Detailed geologic mapping using conventional techniques is often impractical at this scale given the time required for regional scale field mapping. Lineaments can be picked manually or automatically to further reduce the time spent on analysis. However, it must be considered that the accuracy of lineament picking and the efficiency of the technique chosen is generally inversely related; conventional geologic mapping is the most accurate method of defining lineaments while automatic lineament picking from remote sensed imagery is the quickest but least accurate (Suzen and Toprak, 1998). In this study, manual lineament mapping using high-resolution aerial photography was

chosen and linked to detailed field measurements (Chapter 5) to "ground-truth" results. Detailed methodology can be found in Chapter 3.1.

4.1 Lineament Trends

See appendix B for a complete list of lineament orientation trends.

4.1.1 Regional fault lineaments

Regional faults in Otago show two strong preferred orientations (Fig. 4.1) at high angles to one another. The dominant orientation lies between 30-40° ± 10° (NEbN-SWbS) and a second, weaker orientation between 120-130° ± 10° (SEbE-NWbW).

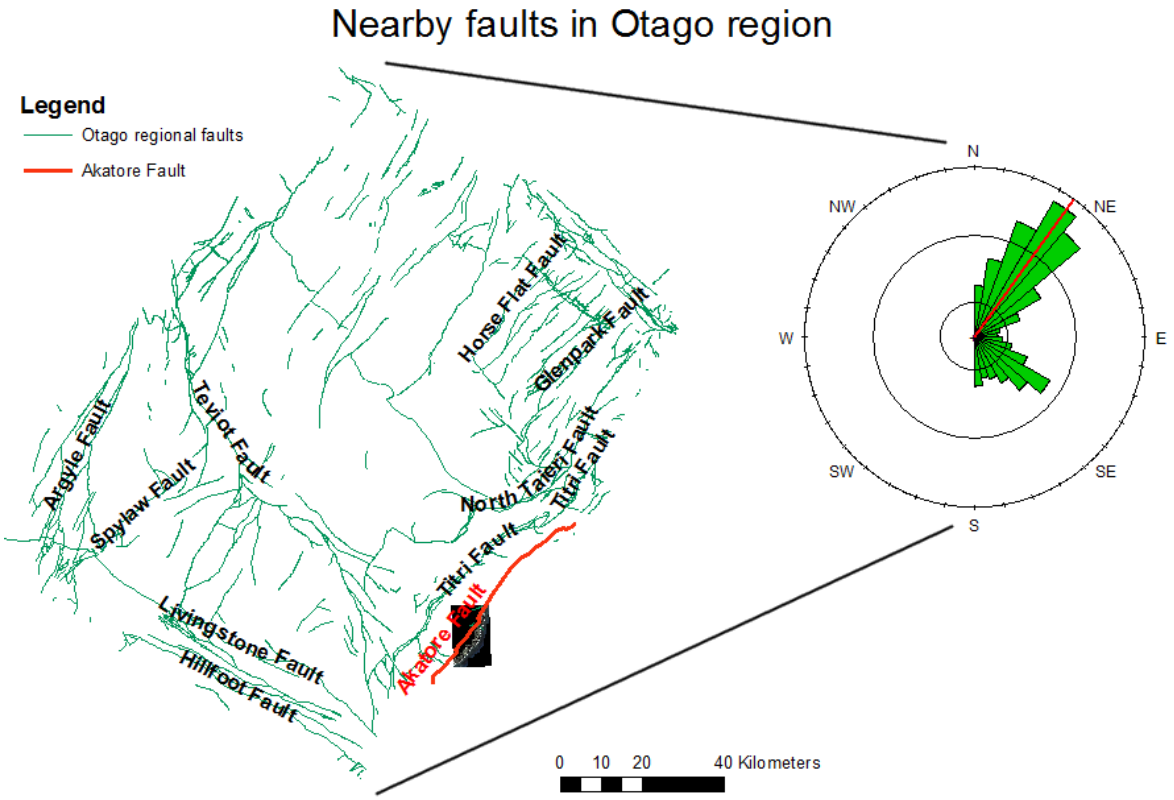

Figure 4.1: Active and inactive faults in the Otago region and associated rose diagram showing preferred orientations. The field region is shown as a black box and the Akatore Fault is highlighted in red in both fault overview and rose diagram.

4.1.2 Complete dataset of coastal lineaments

Orientations from the complete dataset of lineaments along the Akatore coast (Fig. 4.2) show a slight preference for 120-140° orientation, with weaker preferences towards 0-10°, 60-70°, 90-120°, and 140-150°. When the dataset is restricted to lineaments > 30 m in length, 60-80° and 120-140° were equally dominant with lesser preference towards 0-10°, and 90-100°. The most striking feature in both datasets is the absence of data between 30-40° ± 10°.

4.1.3 Coastal lineaments subdivided by assigned groups – 1.6 km long coastal sections

When broken into assigned groups along the coastline, major trends in both lineament datasets (all lineaments and those > 30 m long) can be picked out (Figs 4.5a, 4.5b). In Groups 1 – 6 with all lineaments the primary orientation was consistently 120-140° with secondary orientations of 0-10°, 60-70°, 90-120°, and 140-150° as shown in Fig. 4.3. The 0-10° and 100-110° trends became very weak in Groups 4 (Fig. 4.3b) and 5.

The lower half of the coastline showed more variation in preferred orientation. Group 7 was somewhat transitional with the same primary orientation but secondary trends of 0-10°, 60-70°, 110-120°, 140-160°, and 170-180° although 110-120° and 150-160° were comparatively weak. In Groups 8 to 10 (Fig. 4.4) the dominant orientation shifted from 130-140° to 140-150° with secondary preferred orientations of 0-10°, 60-70°, 110-130°, 140-160°, and 170-180° in Groups 8 and 9 (Fig. 4.4a, 4.4b) and 0-10°, 50-70°, 90-100°, 130-140°, and 150-180° in Group 10 (Fig. 4.4c). Group 9 displayed a broader spread of preferred orientations, 130-160°, with weaker segment peaks compared to Groups 8 and 10. In both Group 9 and 10 orientations 160-180° were weak compared to other secondary trends. In all groups the relative absence of data between 30-40° ± 10° was apparent.

Orientations of assigned groups restricted to lineaments > 30 m showed similar primary orientation trends to the unrestricted groups but had a second primary orientation, 60-80°, in addition to 120-140° (Fig. 4.6). The 0-10° and 90-120° orientations were still the main secondary trends with a weaker 50-60° trend appearing in Groups 3 to 5 (Fig. 4.6b). The primary peaks tightened to 60-70° and 130-140° from Group 6 onwards although 70-80°and 120-130° remained relatively strong (Fig. 4.6c). In addition to the relatively stable secondary peak of 90-100°, trends of 0-10° and 100-120° progressively phased out while a strong 150-160° and a weak 170-180° trend appeared

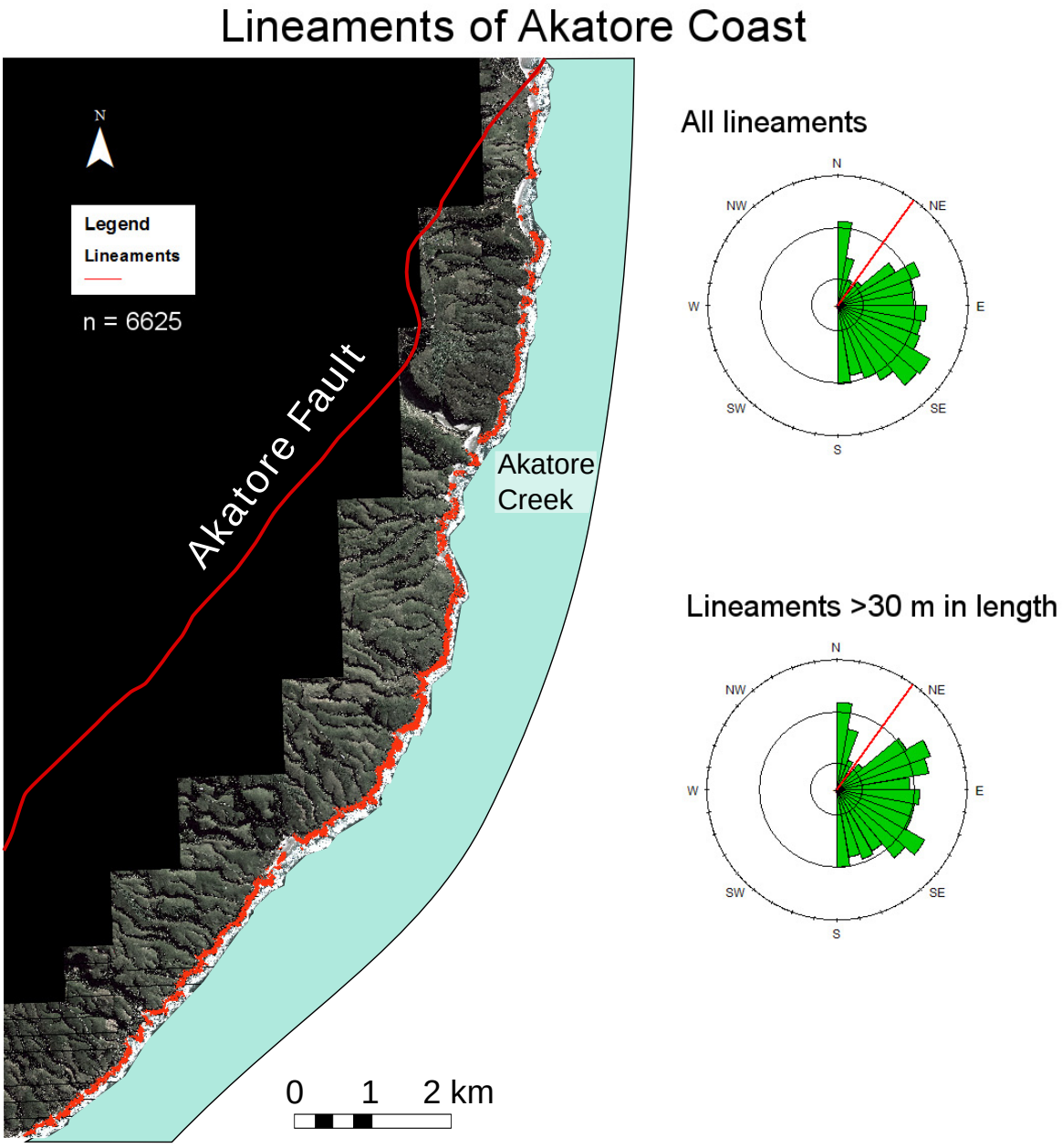

Figure 4.2: Lineaments picked along Akatore coast and associated rose diagrams showing the complete dataset (upper), all lineaments with length > 30m (lower), and trend of the Akatore Fault (red).

in the southern groups (Fig. 4.6d). Again the most constant feature throughout the entire section was the absence of data between 30-40° ± 10°.

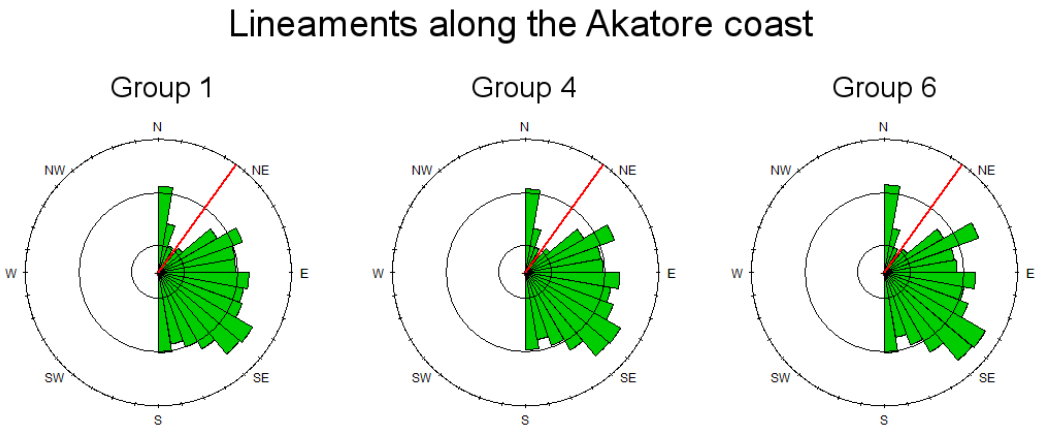

Figure 4.3: Lineaments in a) Group 1, b) Group 4, and c) Group 6 show consistent preferred SEbE orientation with slight variation in subsidiary orientations. Trend of the Akatore Fault is shown in red.

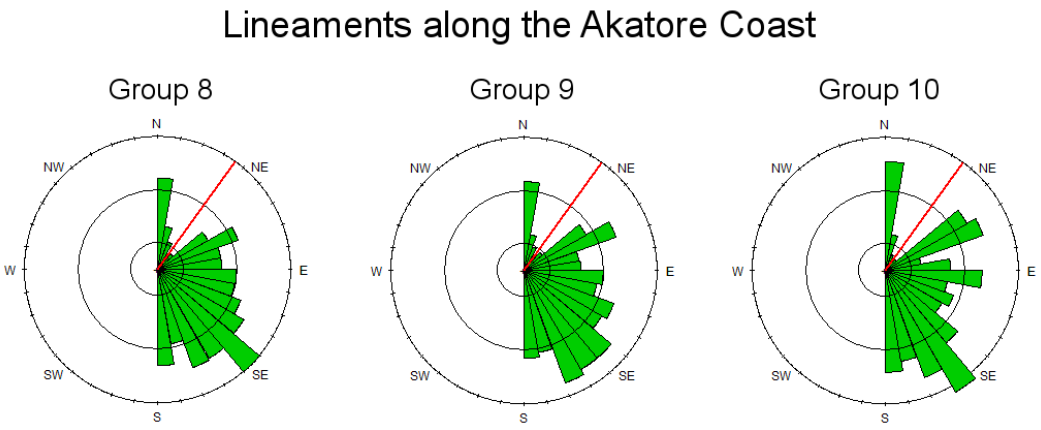

Figure 4.4: Lineaments in a) Group 8, b) Group 9, and c) Group 10 show the variability of preferred orientation in the southern extent of the field area. Trend of the Akatore Fault is shown in red.

Assigned groups along the Akatore coast

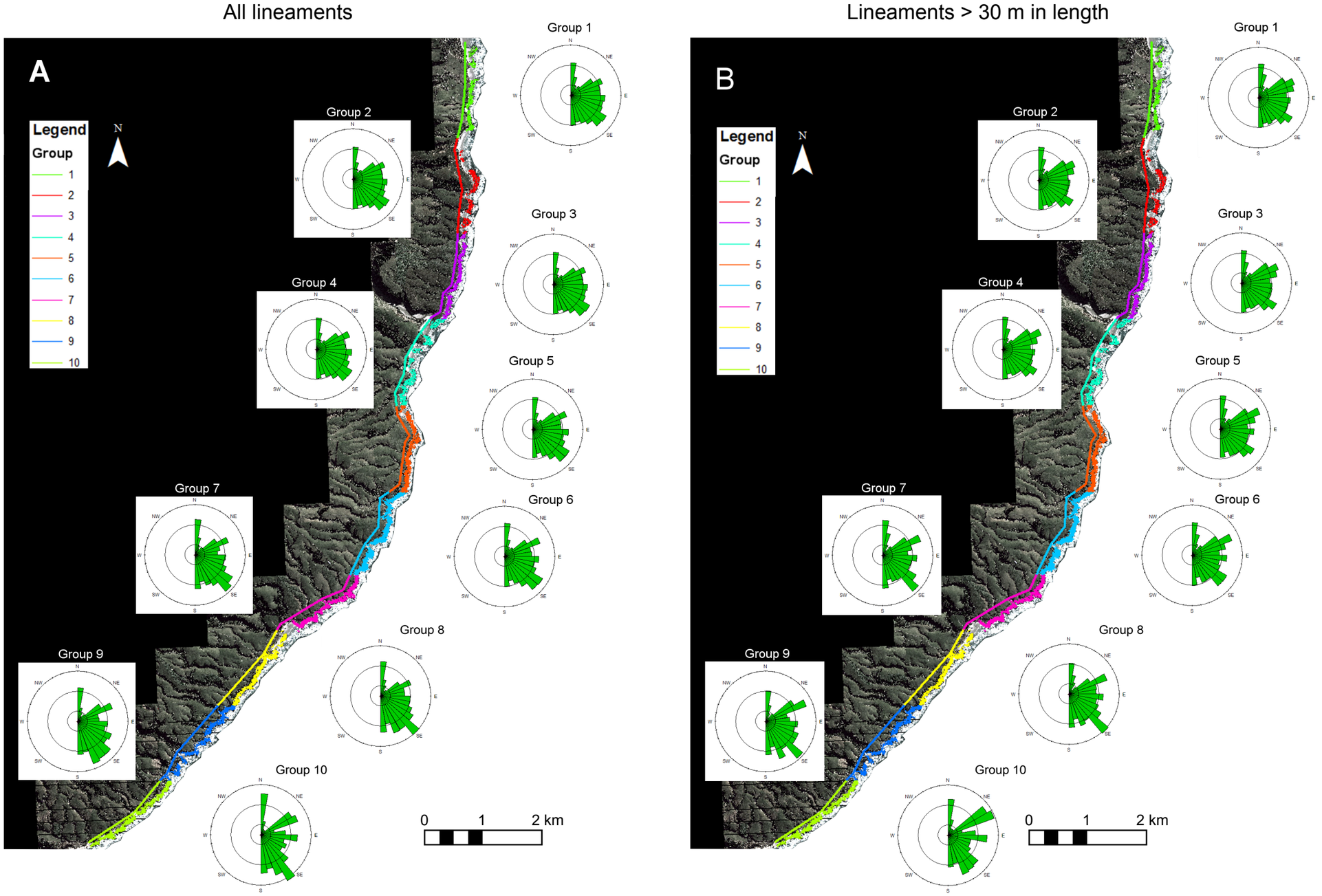

Figure 4.5: Lineaments divided in 10 groups of equal distance along the Akatore coastline using A) the complete dataset and B) all lineaments with length > 30 m.

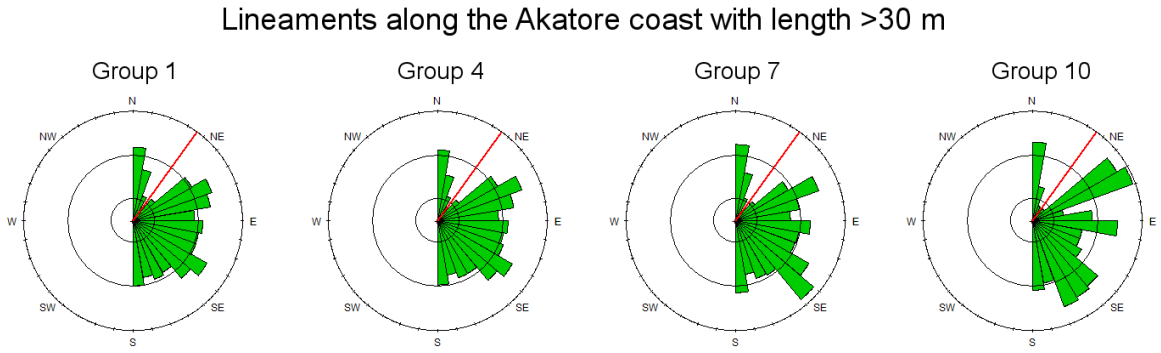

Figure 4.6: Lineaments > 30 m in a) Group 1, b) Group 4, c) Group 7, and d) Group 10 show key preferred orientation changes across the field area. Trend of the Akatore Fault is shown in red.

4.1.4 Coastal lineaments subdivided by natural breaks

Preferred orientation of lineaments divided by natural breaks (21 sections in total) along the coastal platform showed similar trends to lineaments grouped by distance along the coast (Fig. 4.9). With the complete dataset the primary orientation was 120-140° shifting through to 140-150° in the south of the section (Fig. 4.7). Secondary orientations included 0-10°, 60-70°, 90-120°, and 140-150°. The 0-10° and 110-120° orientations were very weak in the northern half of coastline, 0-10° became progressively stronger in the southern half of the section while 100-110° phased out. 60-70° ± 10° also became a strong secondary trend in the southern half of the section. Finally 170-180° was a weak secondary trend apparent in the lower half of the sequence except in Section 21 where it was the dominant secondary trend and the 60-70° became weak. As always the 30-40° ± 10° trend captured almost no lineaments.

Preferred orientation of lineaments > 30 m grouped by natural breaks was primarily bimodal (Fig. 4.8). The dominant trends were 60-70° and 120-130° shifting to 50-70° and 130-140° in the southern part of the section. The only major exception was Section 21 which had primary orientations of 0-10° and 50-70° and 130-140° as a secondary peak. In general, secondary orientation trends included 0-10°, 70-80°, a weak 90-120°, and 130-140° in the upper half of the section with 100-120° dropping out and a weak 170-180° appearing in the lower half of the section. Lineaments trending 30-40° ± 10° were relatively absent. Particularly in the last few sections, dominant orientation trends were very strong compared to sections in the upper half that had a second (120-140°) peak within a set of relatively strong secondary trends.

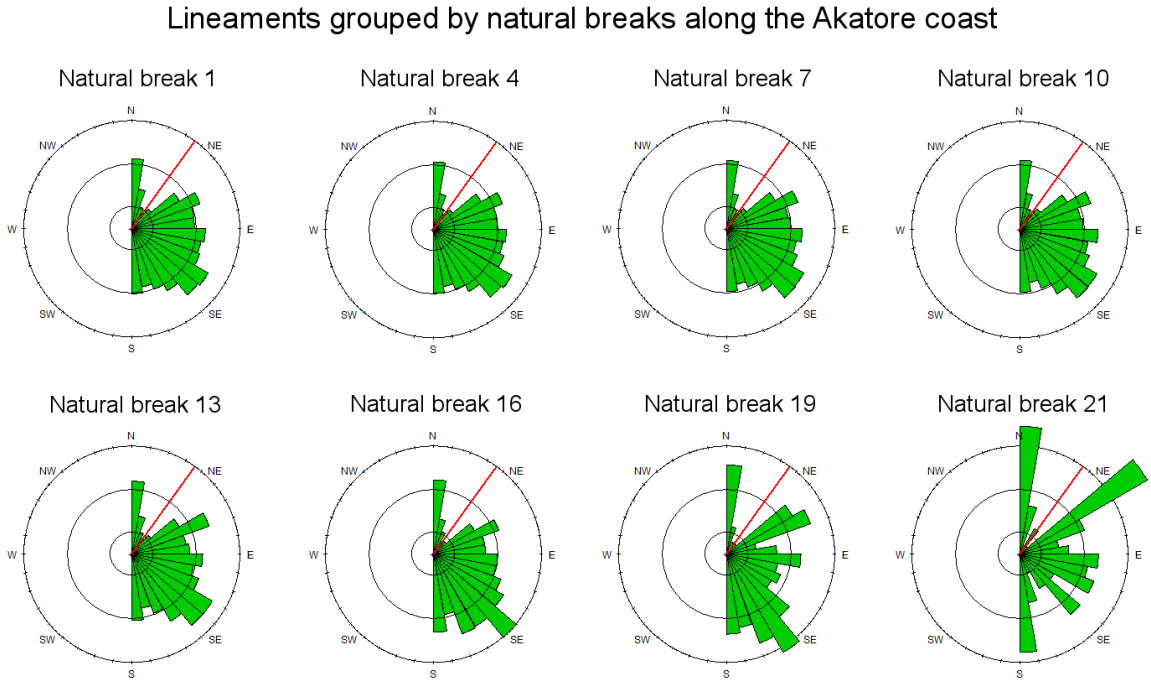

Figure 4.7: Lineaments divided by natural breaks in the coastal platform show key preferred orientation changes across the field area. Trend of the Akatore Fault is shown in red.

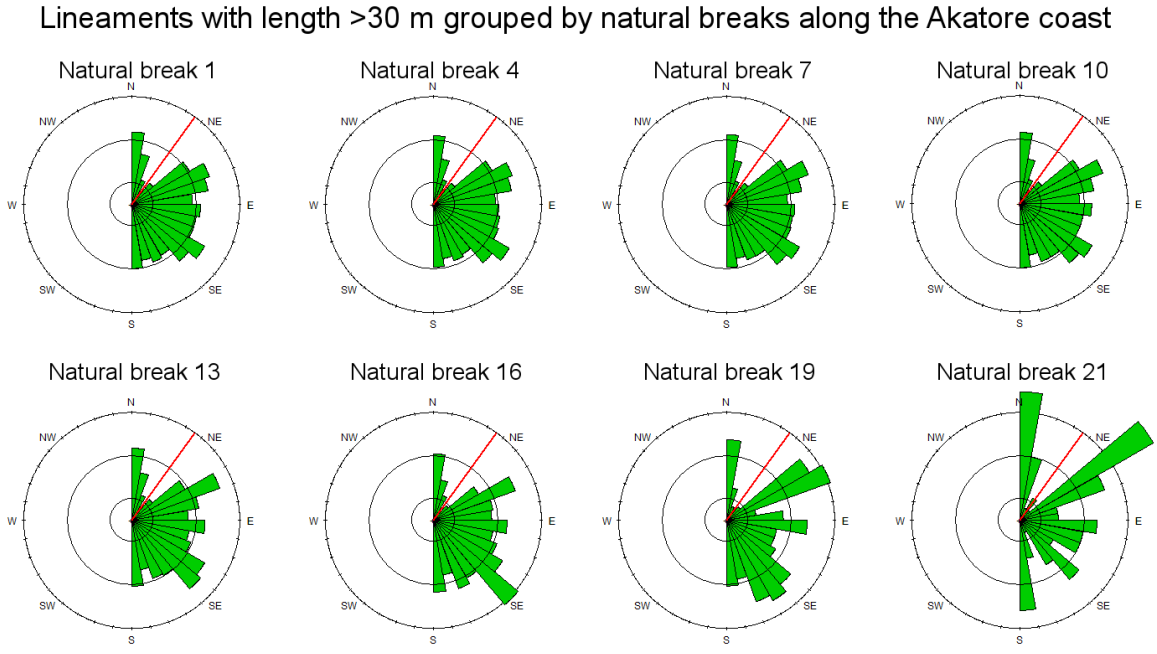

Figure 4.8: Lineaments with length > 30 m divided by natural breaks in the coastal platform show key preferred orientation changes across the field area. Trend of the Akatore Fault is shown in red.

Natural breaks along the Akatore coast

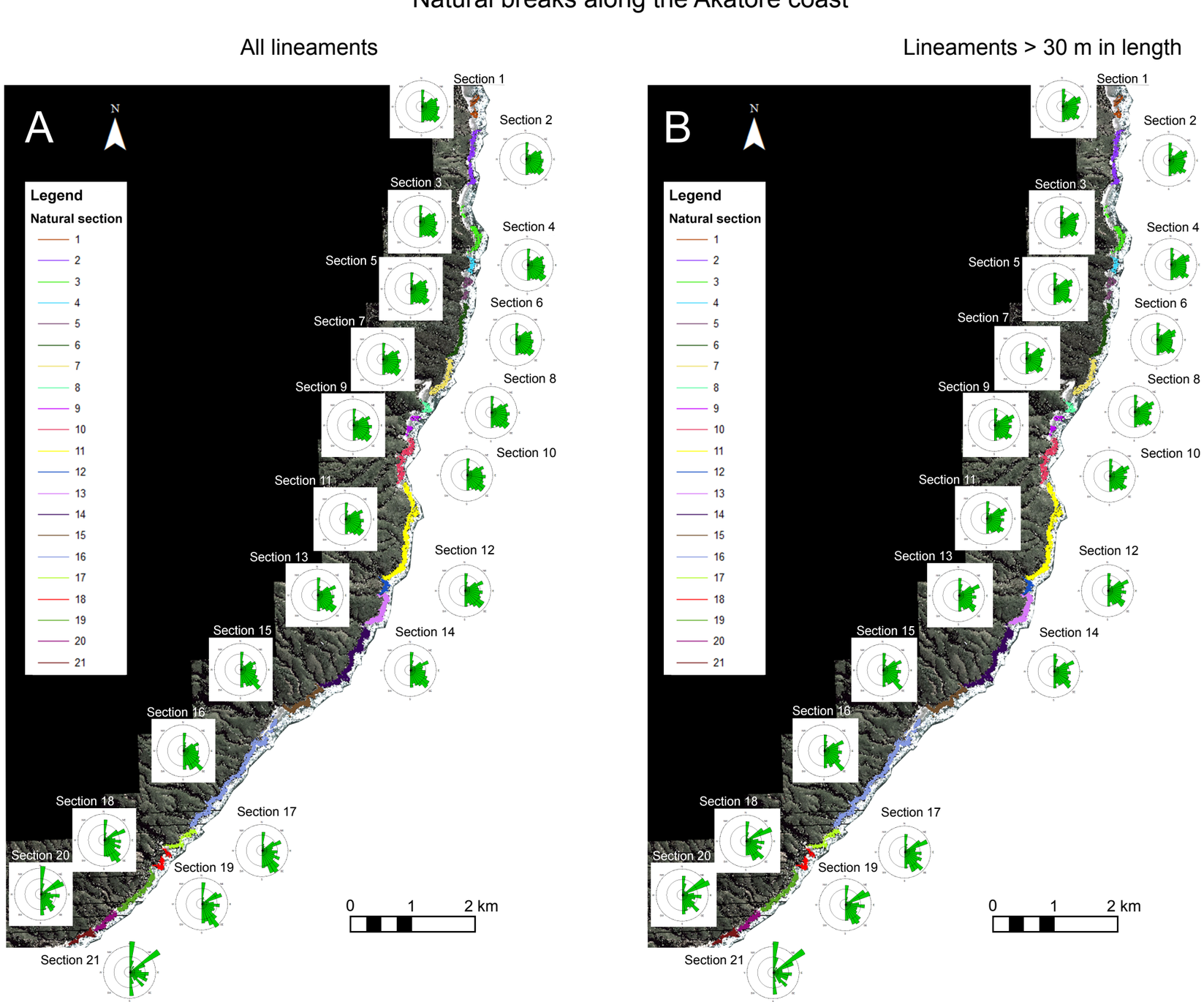

Figure 4.9: Lineaments divided in 21 sections based on natural breaks within the Akatore shore platform using A) the complete dataset and B) all lineaments with length > 30 m.

4.2 Discussion

Lineament orientations along the Akatore coast have distinct preferred orientations that can be drawn out of the data. Across all the data sets principle orientations of 50-70°, 120-140°, and occasionally 0-10° could be seen (Fig. 4.10). The first two primary orientations were often obscured by a range of lower magnitude secondary orientations, particularly around 120-140°, and may be a function of the anisotropic character of the host schist. Nearby regional faults contain a well-defined SEbE-NWbW preferred orientation (Fig. 4.1) that clearly correlates with the main preferred orientation of coastal lineaments. This may indicate that features with linear surface expression trending 120-140° are kinematically or chronologically related to SEbE-NWbW regional faults. This is further explored in Chapter 5.

Unexpectedly, the clear correlation between regional faults and lineaments along Akatore coast does not hold true for the primary NEbN-SWbS preferred orientation of regional faults. The most persistent trend seen in the Akatore coastal dataset is the absence of lineaments with a 30-40° ± 10° alignment. Given the close proximity of the Akatore Fault, which trends NEbN, and the regional dominance of these features, aligned smaller features were expected along the coastal section. This absence is interpreted as a reflection of the inability to capture shallowly dipping features in the lineament analysis.

Additionally, there is no indication of a preference in regional faults for the 0-10° orientation which is a variable, but at times significant, orientation seen along the coast. Strong preferred orientation for 0-10° appears to be restricted to the southernmost extent of the field area within the Chrystalls Beach complex. This orientation likely reflects structures related to the unique deformation history (subduction mélange) of the complex compared to the rest of the field area.

Overall, two preferred orientations can be identified in both regional faults and lineaments identified along the Akatore coastal platform. Regional faults show a strong preference for a NEbN-SWbS trend and weaker preference for an SEbE-NWbW trend. Lineaments along Akatore coast show a moderate, but persistent, preference for a SEbE-NWbW orientation, a weaker preference for an ENE-WSW orientation, and a strong, but locally confined to the Chrystalls Beach complex, N-S preferred orientation. The most pervasive trend in the lineament dataset is the absence of features with an NEbN-SWbS orientation, broadly parallel to the regional Akatore fault.

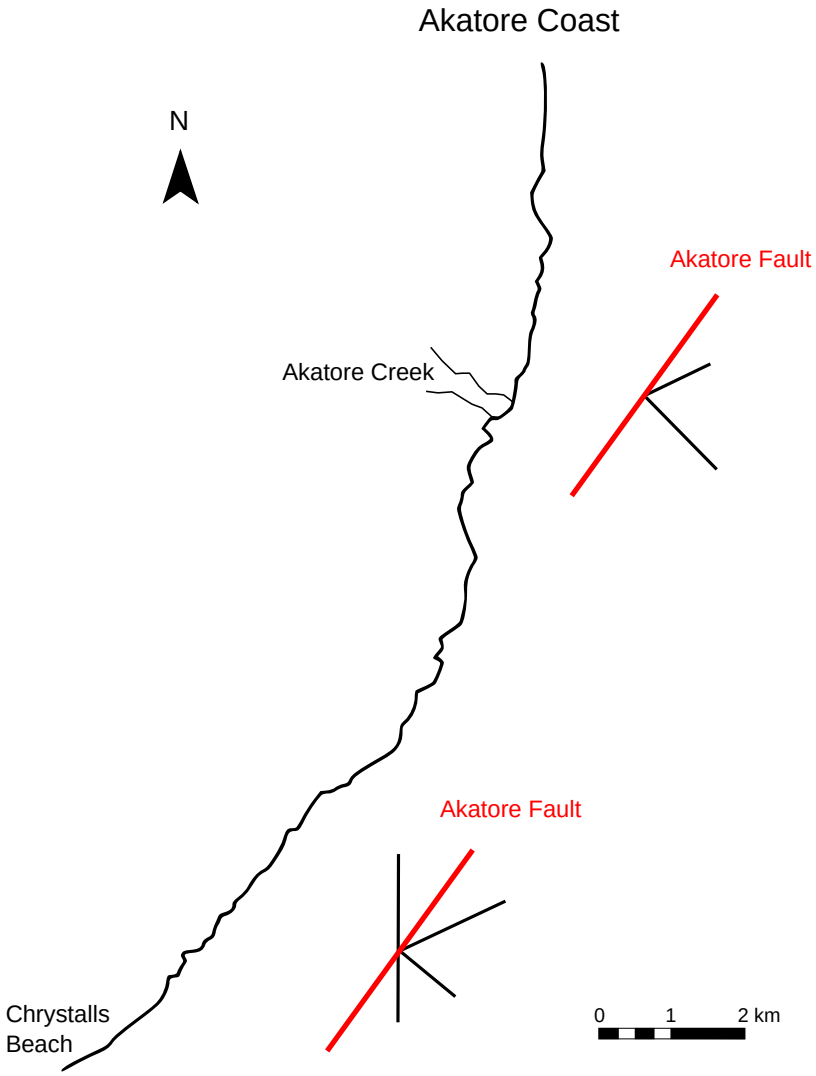

Figure 4.10: Schematic summary showing the main orientation of the lineaments in the north and south with respect to the Akatore fault (red).

Chapter 5

Macro-scale Patterns of Brittle Deformation

Extensive structural mapping allows for characterization of the location, cross-cutting relationships, and fluid flow history of fault rocks and veins throughout the field area. Given the limited number of access points and access time (± 3 hrs. from low tide), mapping the full extent (c. 16 km long) of the coastal platform was not feasible. A c. 2 km long stretch of coastline was selected for detailed structural mapping; the clean coastal platform running north from Akatore Creek was chosen because it best exposes the brittle fault-vein networks of interest and is outside the area that preserves ductile deformation features associated with the Chrystalls Beach subduction mélange (Fagereng, 2009; Hada *et al.*, 2006). Despite restricting the field area, the density of deformation features and constrained access time meant traditional mapping techniques were an inefficient method of collecting the necessary information. In addition, the comprehensive nature of the georeferenced lineament dataset (Chapter 4) across the field area was a valuable resource that offered benefits in terms of locating and relating local-scale features to regional-scale features. It was therefore decided that digital field mapping represented the most efficient and logical method of data collection. A pilot study (Appendix C) was undertaken to field test the different devices and software available at the University of Otago and assess the optimal combination for this study. Following the pilot study orientation measurements of foliation, joints, faults, fault-related veins and breccias, and any kinematic indicators were collected and georeferenced. Particular care was taken to identify structures associated with well-defined lineaments noted from aerial analysis (Chapter 4). Representative samples were also collected for microstructural (Chapter 6) and geochemical analyses (Chapter

7). Full descriptions of the samples collected and types of analyses performed can be found in Appendix D.

5.1 Structural Geology of the Akatore Section

The Akatore coastline is composed of TZIIa sub-greenschist (down to pumpellyite-actinolite facies) rocks of the Otago Schist (Adams and Robinson, 1993; Mortimer, 1993; Robinson, 1958). The lithology is primarily comprised of alternating layers of weakly metamorphosed sandstone and mudstone. Small-scale (multiple sandstone-mudstone sequences within a metre) variations in lithology are common and were therefore not differentiated during mapping.

A 150 m long segment of the coastal platform was mapped in detail using both hand and digital methods (Fig. 5.2). This offers an overview of the spatial and cross-cutting relationships between the primary foliation surfaces, joints, and small-displacement faults (with veins and breccias) that are described sequentially below.

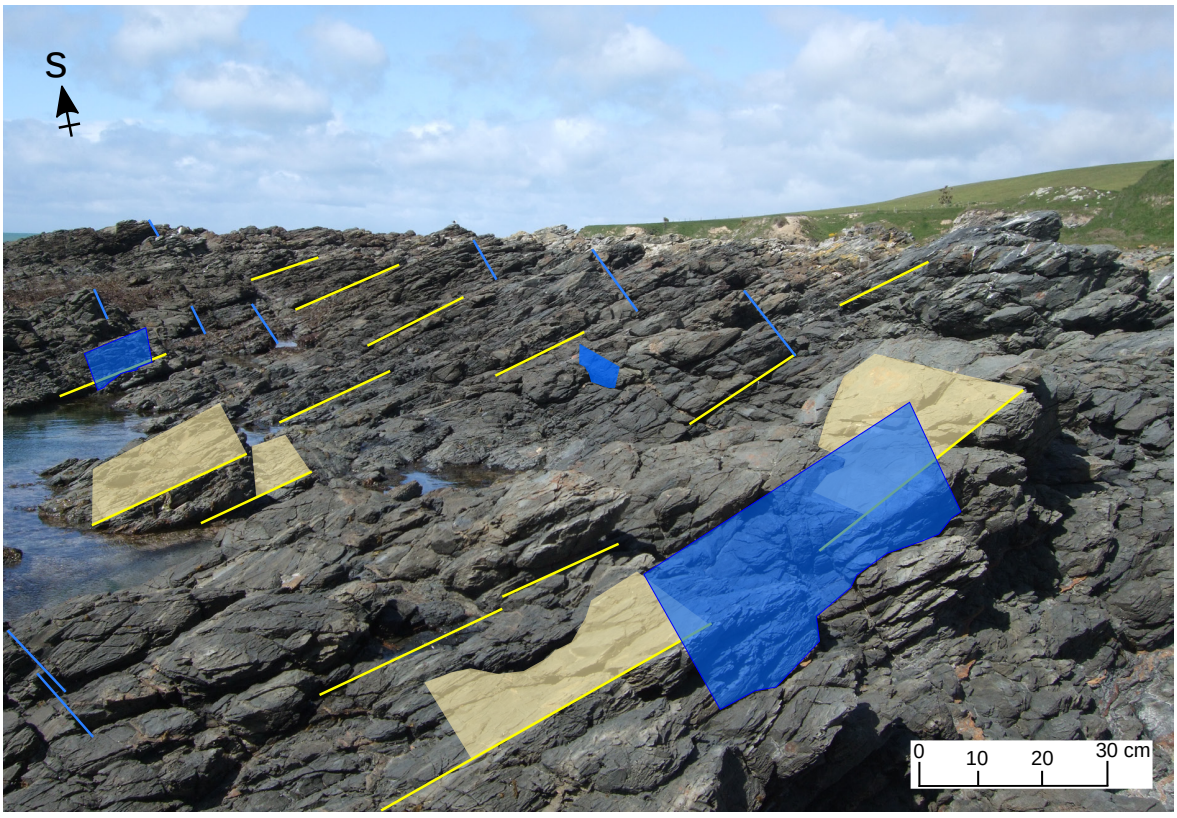

Figure 5.1: Foliation (yellow) and joint (blue) surfaces demonstrating the stacked block morphology of schist.

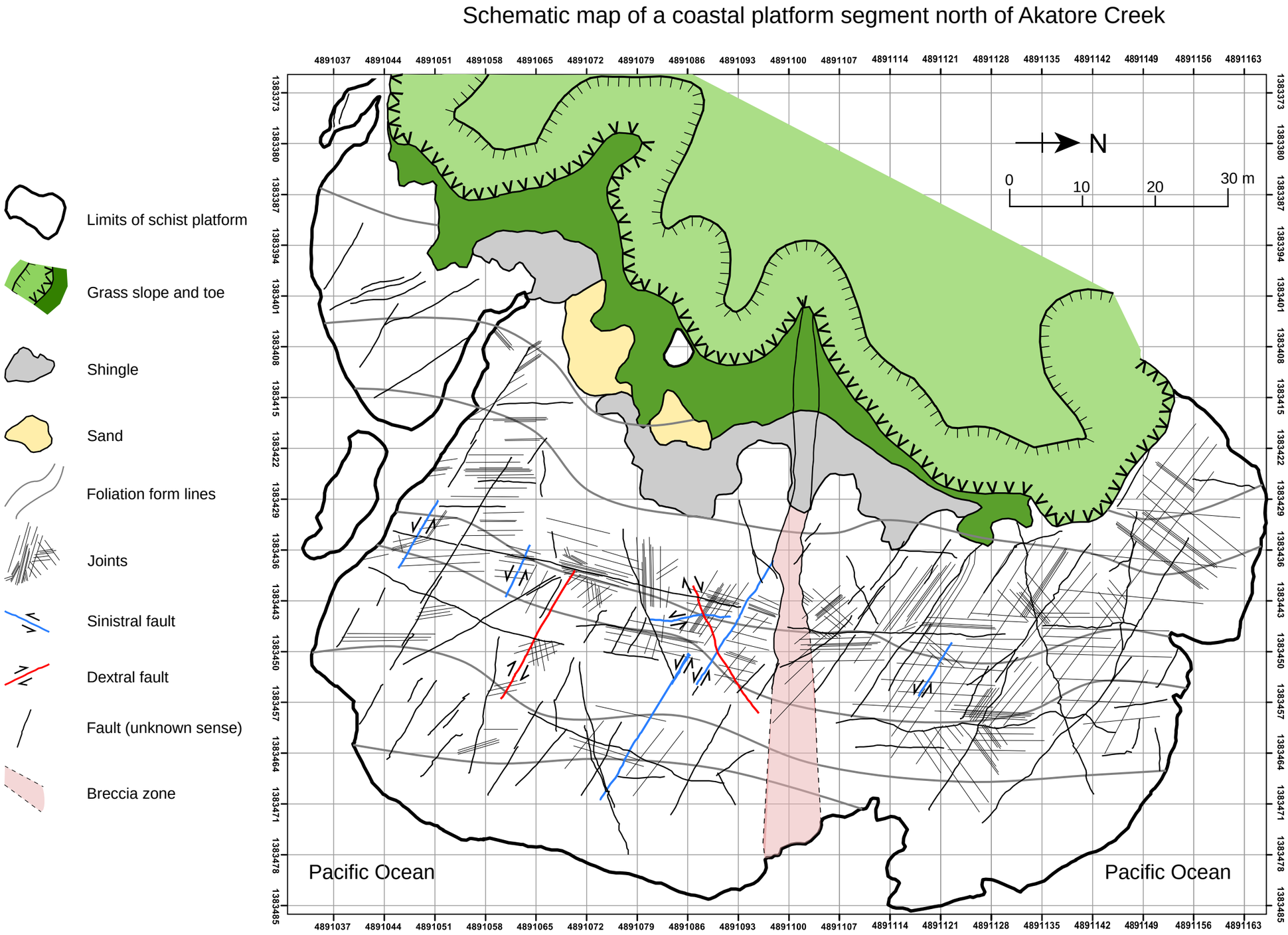

Figure 5.2: Detailed surface map of a 150 m long represntative coastal platform segment.showing the patterns and distribution of structural features mapped along Akatore coast.

5.1.1 Foliation in host rock schist

Foliation surfaces throughout the field area are defined by a shallowly east to south-east dipping dipping slaty cleavage (Figs. 5.2, 5.1, and 5.3). Although locally undulatory in nature, foliation measurements (n=122) across the entire field region show a tight cluster with mean strike and dip of 017/21E as seen in Fig. 5.3.

5.1.2 Joints

The schist is cut by a pervasive network of systematically oriented joints (Figs. 5.2, 5.1, and 5.4). The joints are widespread, relatively planar fractures between abutting rock masses that display no observable displacement and are not filled by vein or fault rock materials. Joints are frequently observed to occur with stepped geometries, where one joints tips out immediately adjacent to another. In the area of the detailed map, left-stepping geometries were most commonly observed, with distances between overlapping joints on the order of a few centimetres to a few tens of centimetres. Measurements (n=209) of joint orientations show at least 3 well-defined sets: 1) a dominant set striking SE-NW and dipping $\sim$ 70°SW; 2) a secondary set striking E-W and dipping 85-90°N and; 3) a subsidiary set striking N-S with variable dip $\geq$ 50°W (Fig. 5.4).

5.1.3 Faults

"First-order" faults - those that are continuous for at least 30 m - may be up to a few metres wide. These faults have characteristic geomorphological signatures; they occupy channels or gullies that are typically filled by relatively thick breccias and extend back to a notch in the grass slope behind the coastal platform (Fig. 5.5). "Second-order" faults may be up to tens of centimetres wide. These are generally small-displacement faults ($<$ tens of centimetres displacement) that are commonly filled by quartz and/or calcite veins (Section 5.1.4) and associated with breccias (Section 5.1.5). Observations from the area mapped in detail (Fig. 5.2) indicate that many of the secondary faults represent reactivated joints, as discussed further below.

Measurements of secondary faults (n=80) have been broken down into three categories based on observed fault separation; sinistral, dextral, or unknown separation (Fig. 5.7). All three categories show a spread of orientations but in general can be confined to the joint or foliation orientations with sinistral faults (n=25) striking SE-NW and dipping steeply SW while subvertical dextral faults (n=11) strike E-W. Faults with unknown sense show well-defined clusters 1) striking SE-NW and dipping steeply

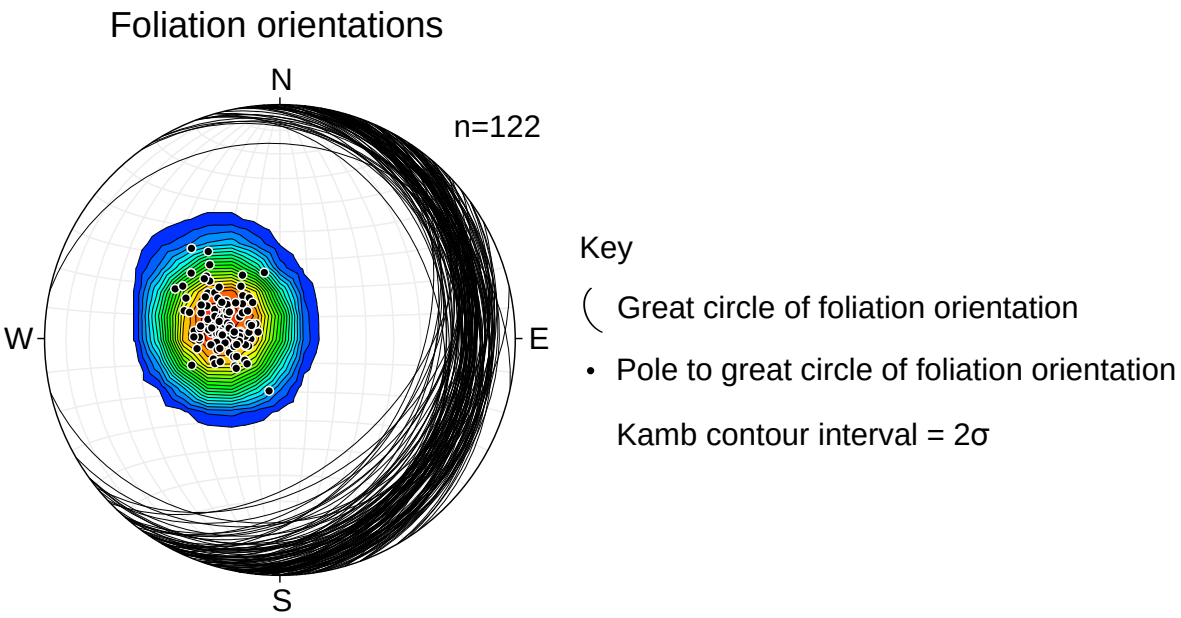

Figure 5.3: Stereonet showing contoured orientation measurements of foliation. Poles have been countered using the Kamb method (Kamb, 1959) with a contour interval of 2σ and a counting area of 4.1%.

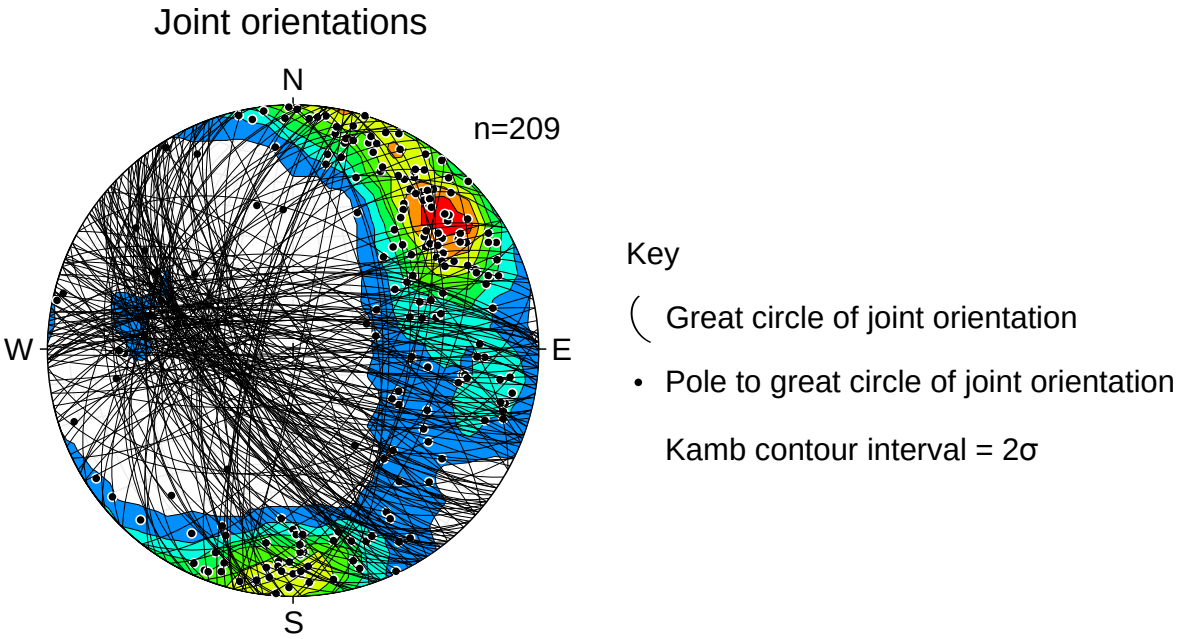

Figure 5.4: Stereonet showing the orientation of joint measurements. Poles have been countered using the Kamb method (Kamb, 1959) with a contour interval of 2σ and a counting area of 4.1%.

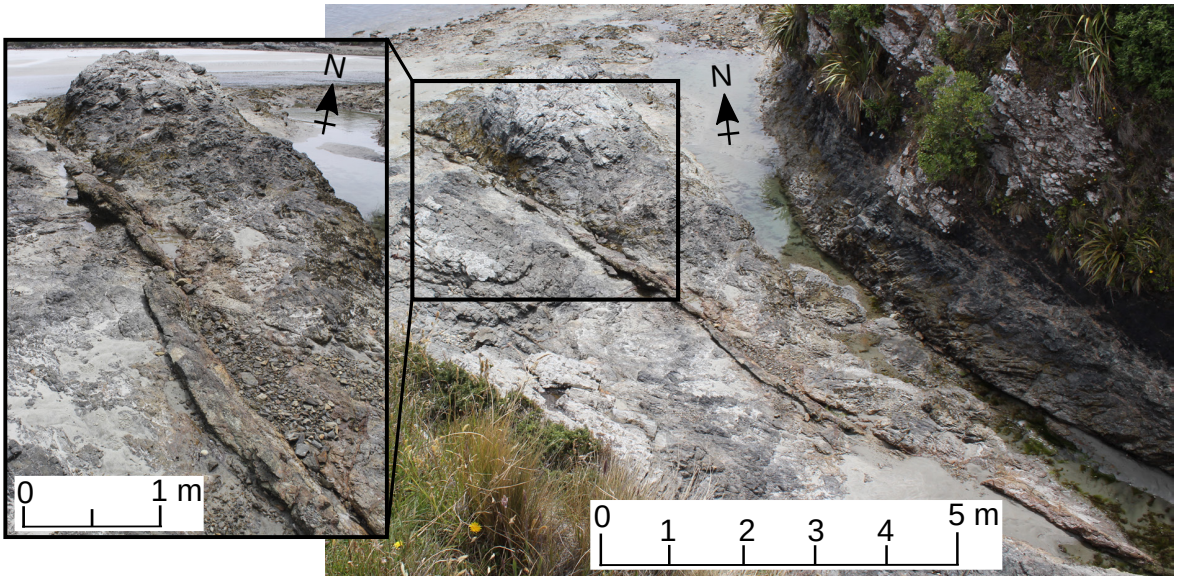

Figure 5.5: Large SE-NW striking fault characterised by a thick (≈ 25 cm) upstanding red breccia cutting through the ridge as a gully.

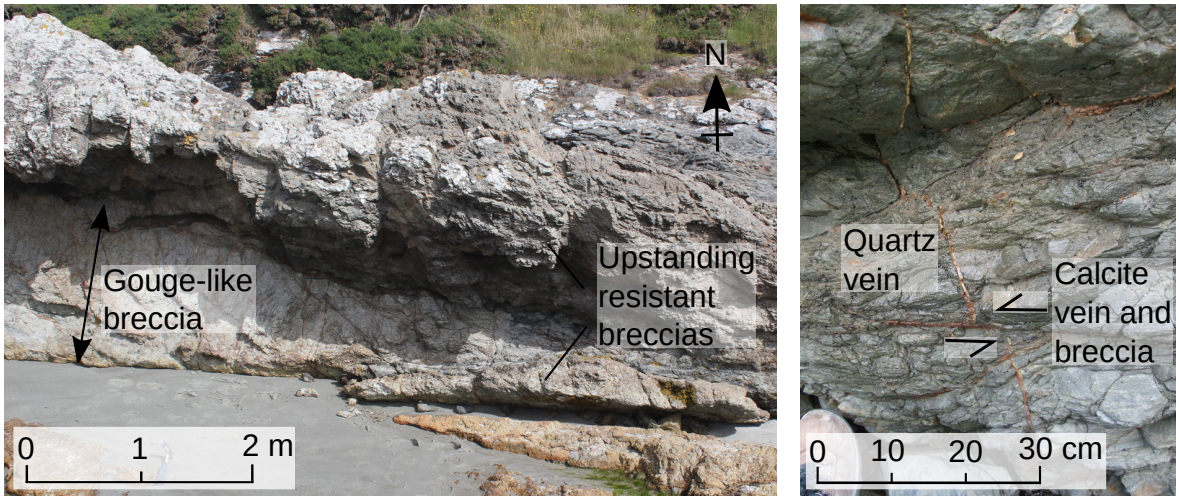

(a) (b)

Figure 5.6: Faults occur across varying scales along Akatore coast. (a) A large upstanding fault striking SE-NW with an approx. 1 m thick interior of gouge-like breccia and more resistant red breccias at the margin. (b) A thin quartz vein is offset 2 cm by a foliation parallel fault containing strands of calcite veins and calcite-rich breccia.

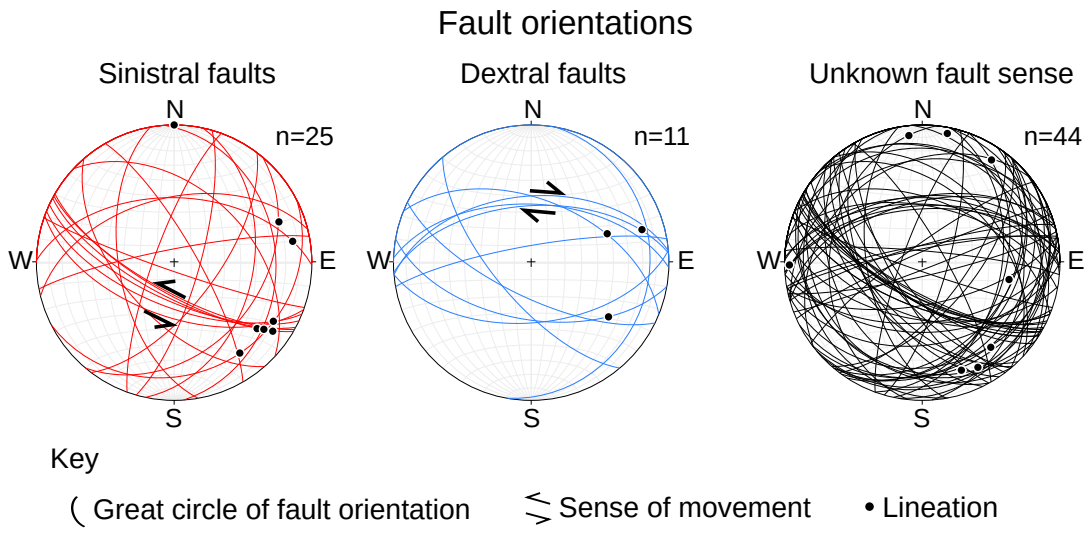

Figure 5.7: Stereonet showing the orientation of sinistral, dextral, and faults with unknown motion sense as well as associated lineations.

SW, 2) striking E-W and dipping steeply N and 3) striking NNE-SSW and dipping up to $\sim 30°$.

A variety of kinematic indicators were identified along faults. Most common are offset markers, usually a joint or breccia displacing a near vertical vein, and dilational jogs between vein and/or joint sets. Sparse lineations have been preserved in some vein material, almost purely as slickenfibres in near vertical quartz or quartz-calcite bearing faults with rare slickenlines (circles in Fig. 5.7). Lineations in shallowly dipping calcite bearing faults are extremely rare. Lineations on conjugate faults indicate mostly strike-slip motion with the central section between SE-NW and E-W faults moving towards the intersection of the planes (Fig. 5.13). Lineations on foliation parallel faults show dip-slip motion.

5.1.4 Fault-related veins

Secondary faults frequently host thin quartz, calcite and paired quartz-calcite veins. Quartz veins are generally resistant, variable size (from ≤ 5 cm to rare ≤ 25 cm) white veins with weathered brown surfaces (Fig. 5.8a, b). Some larger quartz veins are surrounded by pale green alteration zones - thick (≥ 5 cm) bands of schist dominated by quartz. These zones are commonly cut by an anastamosing network of individual quartz veins (Fig. 5.8c). Calcite veins vary in thickness but on average are ≤ 2 cm. Thicker, shallowly dipping examples may show fibres approximately perpendicular to the vein margins as well as a dark medial suture line, or rarely multiple dark lines

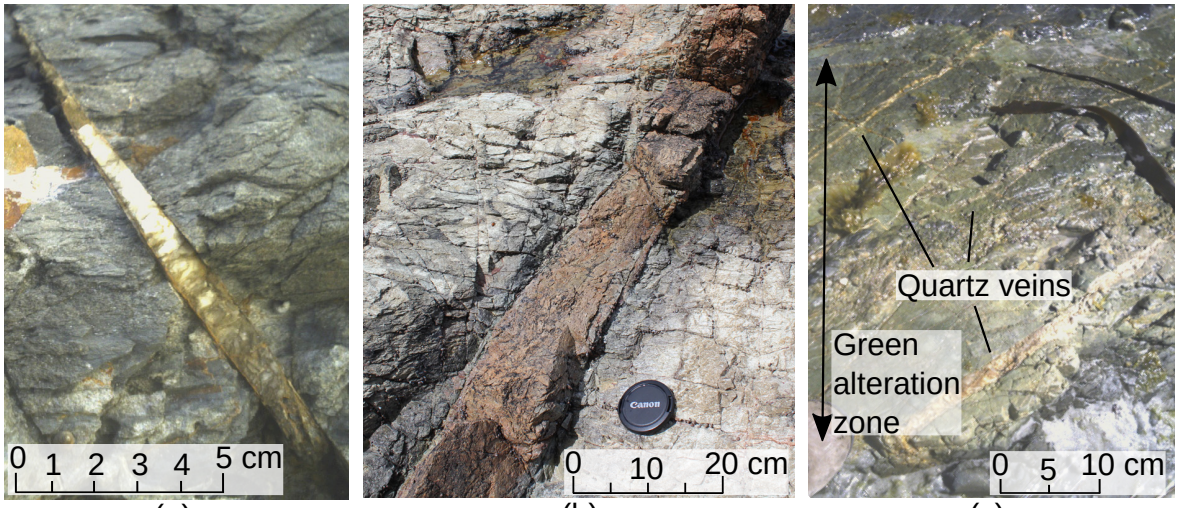

Figure 5.8: Types of quartz veins seen along Akatore coastal platform. (a) Thin resistant quartz-calcite vein filling a joint. (b) Rare thick (∼12cm) quartz vein. (c) Zone of quartose schist with green alteration and multiple distinct quartz veins.

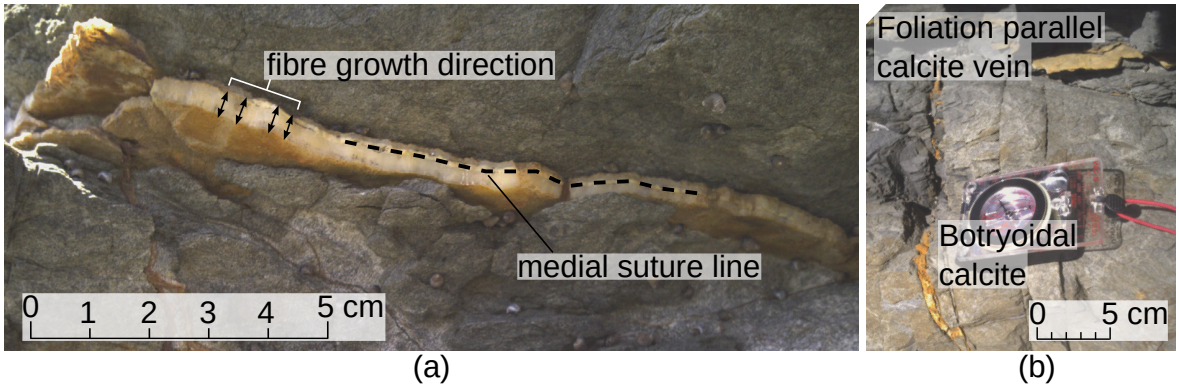

Figure 5.9: Types of calcite veins seen along Akatore coastal platform. (a) Shallowly dipping calcite vein with fibres perpendicular to the vein wall and a medial suture line. (b) Lenses of botryoidal calcite filling an open joint with a shallowly dipping calcite vein parallel to foliation in background.

parallel to vein margins (Fig. 5.9a). The shallowly dipping calcite veins may also be paired with thin, calcite-rich breccias. Calcite that fills steeply-dipping faults tends to occur as thick zones of milky white, botryoidal or vuggy calcite (Fig. 5.9b). A distinctive characteristic of paired quartz-calcite veins are a softer calcite interior with thin, more resistant quartz margins.

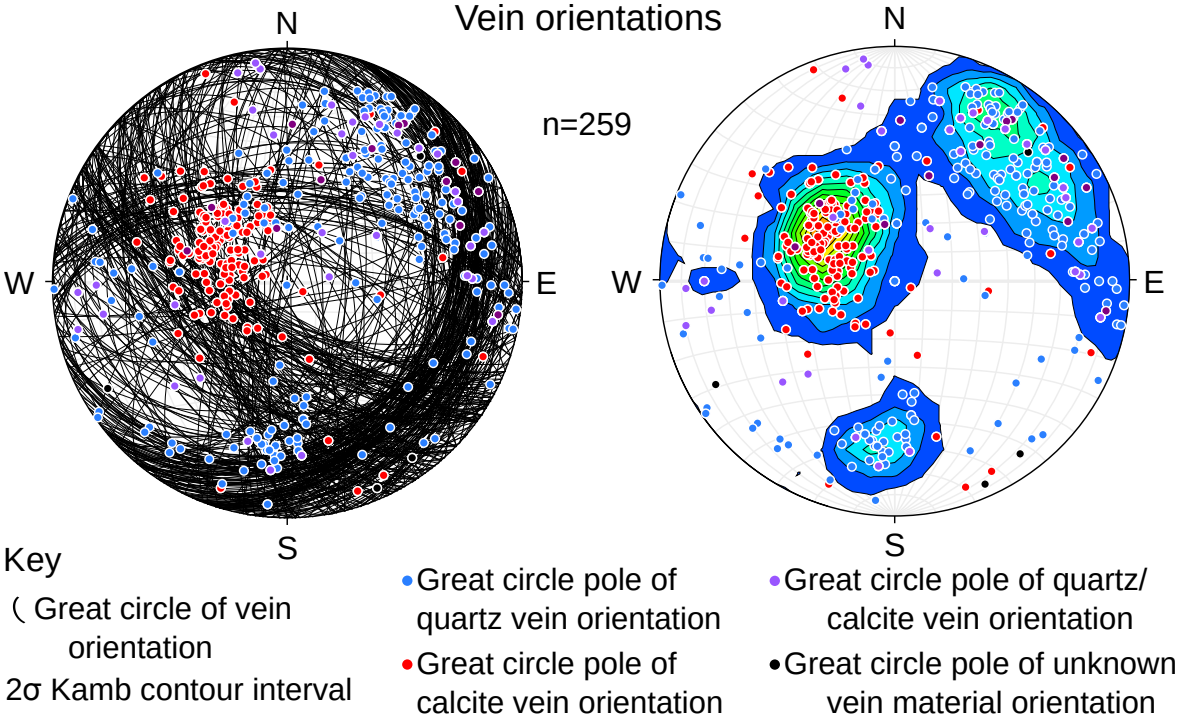

Figure 5.10: Stereonet showing the orientation of vein measurements. Poles have been countered using the Kamb method (Kamb, 1959) with a contour interval of 2σ and a counting area of 4.1%.

Orientation measurements (n=259) of fault-related quartz, calcite, and paired quartz-calcite veins show three broad trends (Fig. 5.10) that closely mirror the orientation of foliation, joints and faults as shown in Figures 5.3, 5.4, and 5.7 respectively. Most prominent are the veins striking NNE-SSW and dipping shallowly east. These veins are roughly parallel to foliation and comprised of pure calcite. Quartz and quartz-calcite veins show a wide range of orientations that equates to dominant joint and fault orientations including: 1) a stretched cluster associated with steeply dipping, SE-NW to N-S striking veins, and 2) a weaker cluster associated with near vertical E-W striking veins.

5.1.5 Fault-related breccias

Fault-related breccias are one of the most characteristic structures visible along the coastal platform. Breccias vary in thickness from a few centimetres to up to a metre and are generally clast dominated. They can be described as crackle breccias (as defined by Woodcock and Mort, 2008) with angular clasts of > 2 mm and minimal rotation relative to neighbouring clasts. Most breccias have a distinctive rusty red colour that comes from the weathered carbonate matrix. Large clast (> 1 cm) dominated breccias appear grey while breccias with small clasts and very high matrix percentage are pale pink.

Measurements of fault-related breccia orientations (n=148) show a more random background spread of orientations than other features. However, like foliation and joints, three trends can be identified. Most dominant is a broad cluster of steeply dipping breccias that strikes SE-NW. These breccias typically occur as rhomboidal regions of breccia in dilational jogs formed in the step-over region between overlapping fault segments (Fig. 5.11). A second, more minor cluster of steeply north dipping breccias strike roughly E-W. These breccias are continuous but have formed in intact schist meandering between E-W striking joints rather than being locally confined to the joints. Finally there is a loose cluster of shallowly east to south-east dipping breccias with calcite veins that strikes NNE-SSW.

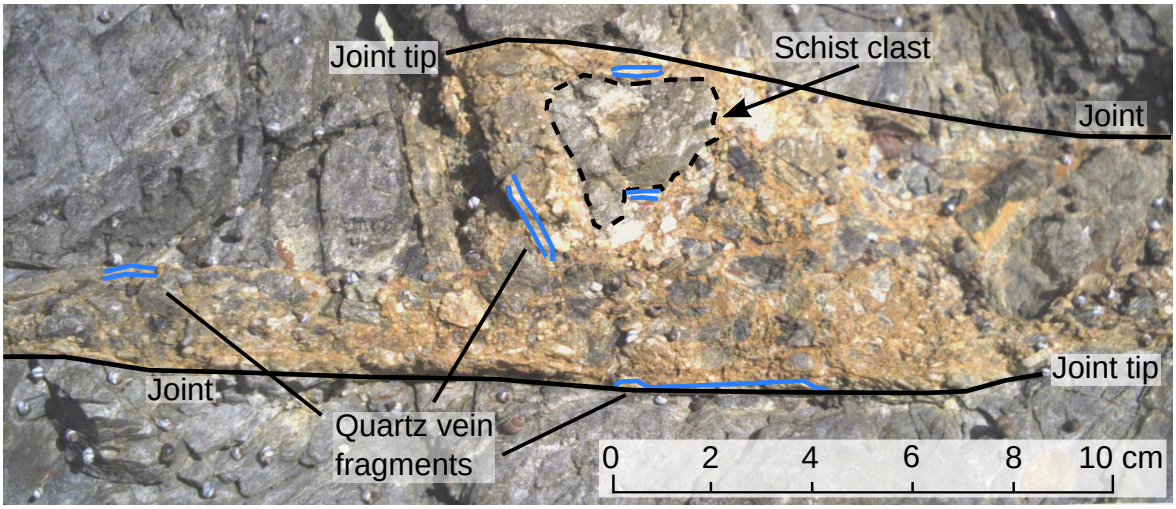

Figure 5.11: Dilational jog formed in the step over region between two adjacent joint tips filled by a breccia with grey schist clasts and fragments of quartz veins (blue) in orange calcite-rich matrix.

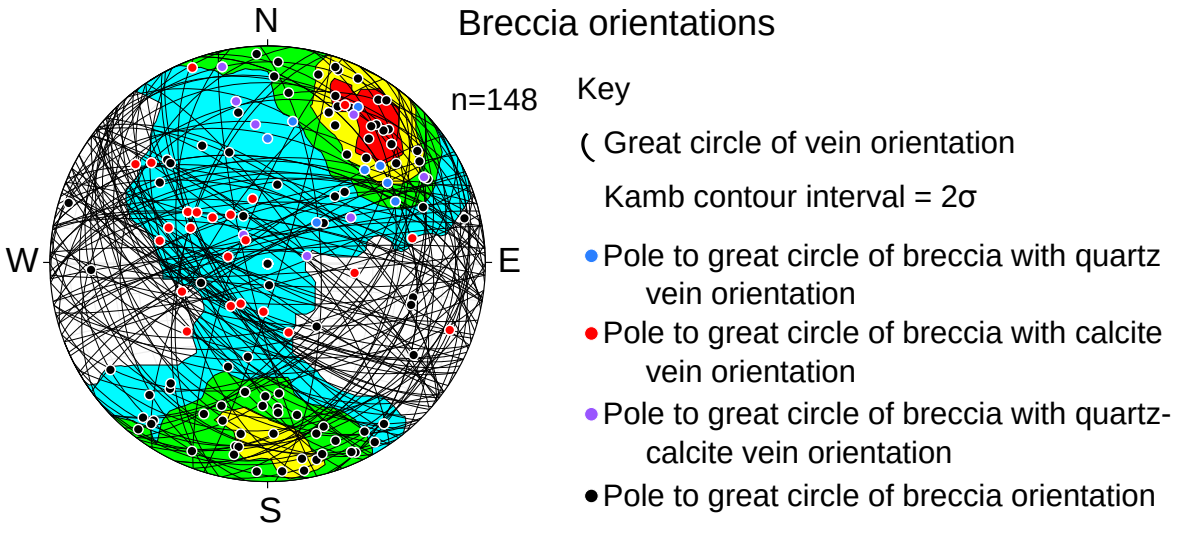

Figure 5.12: Stereonet showing the orientation of breccia measurements. Poles have been countered using the Kamb method (Kamb, 1959) with a contour interval of 2σ and a counting area of 4.1%.

5.2 Stress Inversion

A stress inversion can be performed on a dataset of faults with associated kinematic indicators in order to resolve the regional stress tensor under which the faults broke. There are several assumptions inherent to a stress inversion; namely that a) the population of faults ruptured under the same stress tensor i.e. corresponds to a single tectonic event (Angelier, 1979), b) fault displacement is small relative to fault length, c) the stress tensor is homogeneous and the rock is isotropic, and d) that slip on each fault plane occurred in the direction of maximum shear stress (Wallace-Bott assumption; Pollard *et al.*, 1993). In general a stress inversion is more reliable if assumptions a and b are met while assumptions c and d are inherent in any stress inversion and cannot be avoided.

Stress inversions work because the rake of a slickenline on a given fault is dependent on the three angles which define the orientation of the fault plane relative to the orientation of the principal stresses and the aspect ratio of the stress tensor i.e. the magnitude of the principal stresses (Bott, 1959). A computer can be used to back-calculate the necessary paleostress field (principal stresses and stress ratio) needed to produce a slickenline of the orientation measured on the given fault. By comparing multiple faults with striations which have slipped under the same stress regime it is possible to find the optimal paleostress field which contains the least angular separation between the modelled shear stress and true slip vectors with principal stress magnitudes

sufficient to induce slip. [Angelier, 1990]

5.2.1 Win_TENSOR stress inversion program

Win_TENSOR by D. Delvaux is an open source program for inverting kinematic and EQ focal mechanisms to analyse tectonic stress. It utilizes an improved Right Dihedron method to estimate the relative (not absolute) stress ratio from the inferred orientations of the principal stresses and also filters out incompatible fault slip data. The data then undergoes iterative inversions called Rotational Optimization. The Rotational Optimization method uses the initial stress tensor found with the improved Right Dihedron method to restrict the search area then tests various stress tensor configurations against the dataset in an attempt to progressively find an optimal tensor that meets the Mohr criteria for failure on a pre-existing surface. Full details on procedures used by TENSOR can be found in Delvaux and Sperner (2003).

5.2.2 Data

Twenty-nine slickenlines were identified on small displacement secondary faults across the coastal platform (see Section 5.1.3 for a description); 12 are striations on slickensides, and the remaining 17 are slickenfibres in quartz or paired quartz-calcite veins where fibres are assumed to have grown incrementally parallel to the direction of maximum shear stress. Shear sense of the host faults has only been identified in 11 cases; 8 of the faults are sinistral while the remaining 3 are dextral. Sense of movement was not directly observed on the remaining faults.

Data was input into Win_TENSOR in the format of dip/dip direction for faults and rake/azimuth for slickenlines. Win_TENSOR omits data that gave unknown shear sense from the calculation so, given the paucity of the dataset, fault motion was inferred from orientation using the fault orientation patterns identified in Fig. 5.7. The data was then weighted corresponding to confidence in slickenline measurement and inferred vs. measured shear sense.

5.2.3 Results

Figure 5.13 shows the stress tensor calculated by Win_TENSOR. The principal stresses (plunge/trend) with 1σ errors are $\sigma_1 = 23/114 \pm 48.7°$, $\sigma_2 = 65/268 \pm 34.6°$, and $\sigma_3 = 10/020 \pm 49.9°$. Angular deviation was $37.8 \pm 19.9°$. Only 28 of the 29 data points were used to build the stress tensor as the fault and lineation orientations of

one data point were incompatible with strike slip motion so the fault motion was left as unknown.

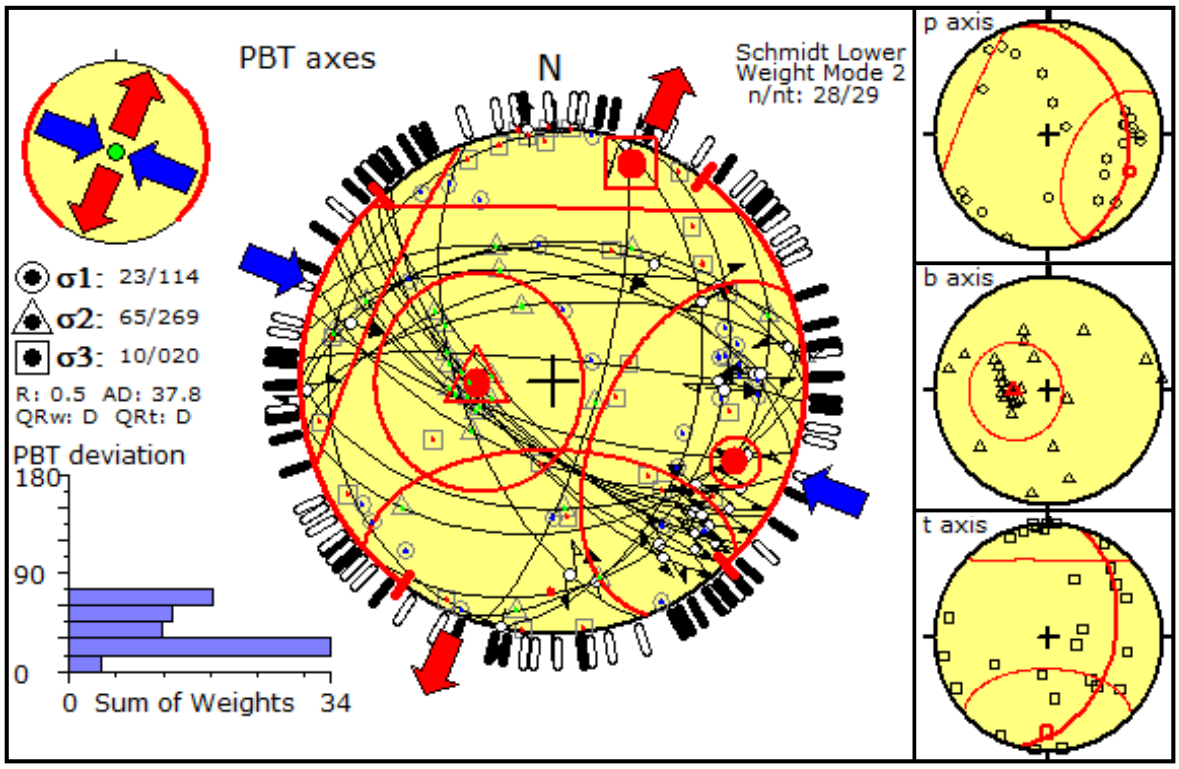

Figure 5.13: PBT diagram calculated from the orientation of faults and associated slickenlines (black lines and flags respectively). The orientation of the principal stresses are shown as a red circle (σ_1), triangle (σ_2), and square (σ_3) with associated uncertainty as the surrounding red circle. Compression (blue arrow) and extension (red arrow) axes indicate the stress tensor orientation, angular deviation of the p axes is shown in red on the stereonet perimeter and as a histogram in the bottom left corner.

5.3 Discussion

Careful examination of the morphology, characteristics and orientation patterns of the features described above, in combination with the results from regional lineament analysis (Chapter 4), allows several conclusions regarding the relative timing and mechanisms of formation to be drawn.

5.3.1 A chronology of brittle faulting

Cross-cutting age relationships

Based on cross-cutting relationships, a brittle fault fabric chronology along Akatore coast has been established in the following sequence (Fig. 5.14). 1) Packages of mudstone and sandstone are lightly metamorphosed creating a through-going foliation of slaty cleavage (light grey foliation form lines in Fig. 5.2, Fig. 5.14A). 2) Long, planar SE-NW striking joints, with subsidiary E-W and N-S joints, form during exhumation of the Otago Schist during the Late Cretaceous (Fig. 5.14B). 3) Exhumation joints are reactivated as small displacement faults and are filled by fault related veins and breccias (Fig. 5.14C). In SE-NW striking sinistral faults quartz was precipitated followed by calcite along with lozenges of breccia in dilational jogs (blue and black faults in Fig. 5.2) between adjacent joint tips. Dextral E-W striking faults form continuous calcite-rich breccias with rare quartz and quartz-calcite veins mostly in intact schist as a conjugate set to SE-NW striking faults (black and red faults in Fig. 5.2). 4) High fluid pressure drives open extensional fractures parallel to foliation allowing calcite veins and breccias to form (Fig. 5.14D). The relative timing of steeply dipping faults with paired quartz-calcite veins vs. foliation parallel calcite veins is undetermined, they may have formed contemporaneously or at different times as a series of calcite-rich fluid events. 5) Unconfined botryoidal calcite forms in open voids, mostly in the intersections of steeply dipping joints and on top of pre-existing breccias (Fig. 5.14E).

Joints

The long, planar, and systematic nature of joints in the Akatore platform matches joints in the Otago Schist described by Weinberger *et al.* (2010). As explained by Weinberger *et al.* (2010) formation of these joints can be attributed to exhumation during the Cretaceous releasing residual elastic strain through tensile fracturing. Steeply dip-

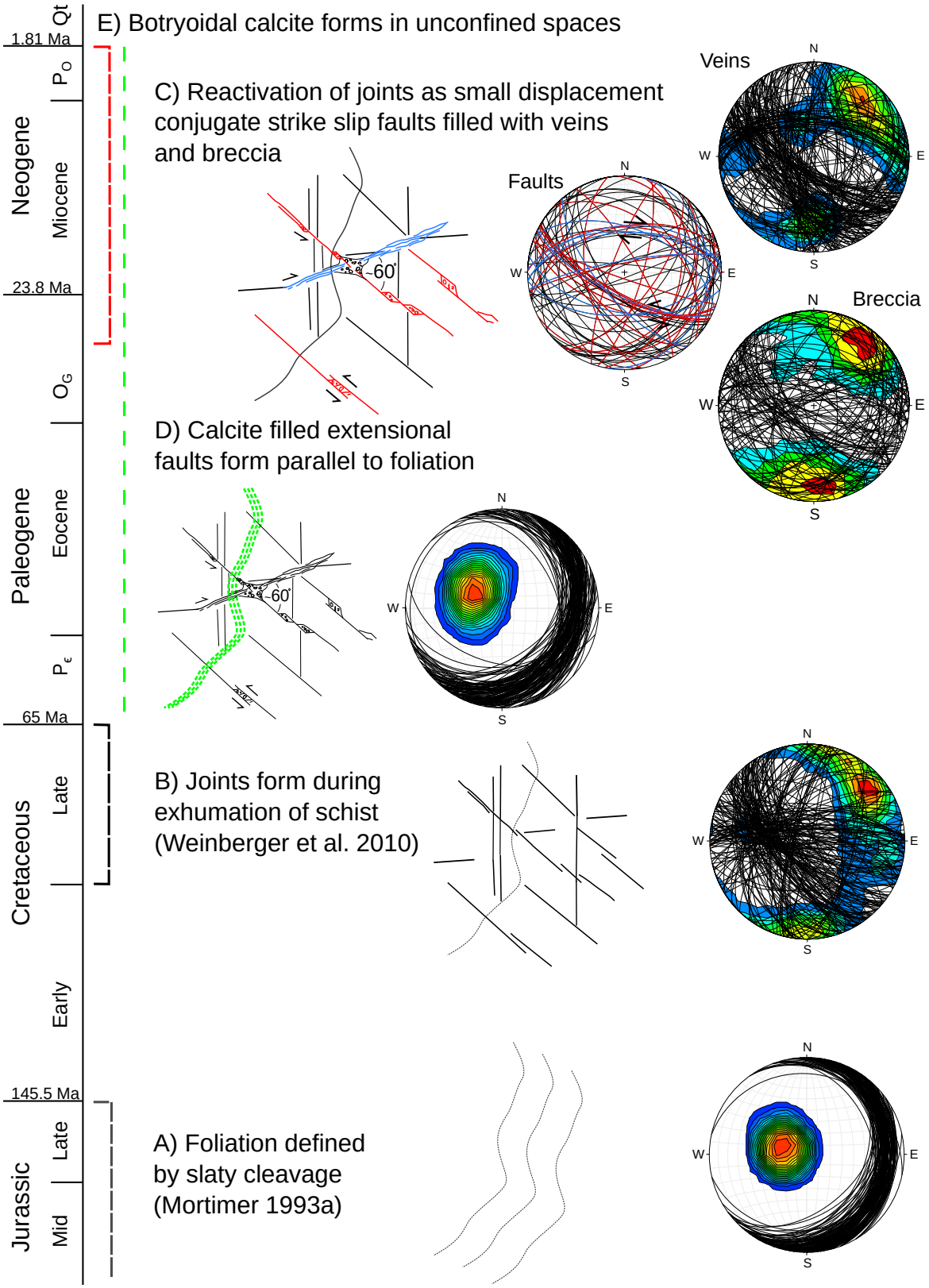

Figure 5.14: Schematic showing the occurrence of different brittle deformation features at Akatore coast with stereonets of feature orientation.

ping SE-NW and E-W striking joints clearly overlap with steeply dipping fault-related quartz vein, quartz-calcite vein, and breccia orientations. Rare, steeply dipping calcite veins can also be found in these orientations. These calcite veins are usually thick discontinuous zones where botryoidal calcite has freely formed in voids and thin lenses injected along open fractures at the intersection of joints. The localization of these veins, breccias, and faults in exhumation joints indicates that brittle deformation in the post-Cretaceous preferentially utilized pre-existing weaknesses in the rock.

Faults, veins, breccias, and reactivated joints

The most striking pattern in the data is the trend of foliation and calcite vein orientations. Both are tightly constrained as shallowly dipping, NE-SW striking features. The broad trend of this pattern is also repeated, to a lesser extent, within the breccia dataset as well as rarely to faults of unknown fault sense. As described in vein descriptions (Section 5.1) these foliation parallel calcite veins are often characterised by fibres perpendicular to the vein margin. The fibrous texture indicates that these veins likely formed through fluid overpressure driving open fractures roughly parallel to foliation. Fibres show median surfaces indicating antitaxial growth but are rarely curved so offer no insight into lateral motion during formation. The dark medial suture line which can sometimes be seen, and is occasionally accompanied by further dark lines, may represent crack-seal events where incremental strain was accommodated on a weak plane (the calcite vein) through repeated fracturing and resealing by precipitated calcite. This idea is further explored using cathodoluminescence in Chapter 6.

Fluid flow

The abundance of veins throughout the Akatore coast indicates significant fluid migration has occurred since the Cretaceous. Relative timing of fluid events can be loosely established using different vein types. Almost all steeply dipping SE-NW and N-S veins are of quartz or paired quartz-calcite, steeply dipping pure calcite veins are much more rare. Paired veins show quartz margins and calcite interiors indicating that the quartz was initially precipitated into joints followed by calcite precipitation contemporaneous with reactivation as small displacement sinistral faults allowing emplacement of breccia lenses in dilational jogs. The inclusion of quartz fragments in these breccia pods also indicates that quartz was precipitated before reactivation of SE-NW striking joints and associated calcite precipitation. In contrast shallowly dipping veins are, with rare exceptions, purely calcite and are assumed to have precipitated due to fluid

overpressure opening extensional fractures along foliation surfaces. As these features are very shallowly dipping, little to no offset of foliation parallel calcite faults relative to steeply dipping faults or vice versa is observed and the timing of foliation parallel faults are therefore poorly constrained relative to the reactivation of steep joints and later botryoidal calcite precipitation.

Steeply dipping features broadly striking E-W are not as tightly restricted as other dominant orientation trends, varying between E-W and NEbE-SWbW. These faults mutually cross-cut SE-NW striking features to form a conjugate set at $\sim 60°$. Although fill material is the same as SE-NW striking features the morphology is markedly different. Fault-related veins are not as dominant in this orientation, rather continuous breccias (as opposed to breccia lozenges restricted to dilational jogs) are common and meander between intact schist and E-W joints as dextral faults.

5.3.2 Paleostress field at Akatore

The stress tensor resolved by Win_TENSOR is characterised by subhorizontal σ_1 azimuth trending 114°and subvertical σ_2, a classic Andersonian strike-slip regime. The modern day stress tensor in the Canterbury region is given by Sibson *et al.* (2011, 2012) with a subhorizontal σ_1 azimuth trending $115° \pm 5°$. The modern stress tensor in the Otago region is inferred from the Galleon-1 well breakout (Sibson *et al.*, 2011) and microseismicity data Reyners *et al.* (1983) to match the Canterbury tensor. Earthquake focal mechanisms and borehole blowout data from the 2010-2011 Christchurch earthquake sequence was used to generate the Sibson *et al.* (2012) stress inversion. The modern-day stress field documented by these techniques in Canterbury and Otago is strikingly similar to the paleostress field derived from conjugate strike-slip faults along Akatore coast (Fig. 5.15). This suggests that strike-slip faults along the Akatore coast will have ruptured within the past $\sim$ 25 Ma (Beanland and Berryman, 1989; Sibson *et al.*, 2012) under the modern stress configuration. Angular deviation and errors associated with the stress inversion of Akatore data are significant but are likely due to the relatively small dataset used to generate the stress field and the difficulty in finding reliable kinematic indicators which can be weighted to full confidence.

The 2010-2011 Christchurch earthquake sequence (Fig. 5.15) was a composite rupture that occurred in basement metamorphosed Torlesse metasediments and the overlying sedimentary cover sequence. The first motion focal mechanisms of the M7.1 Darfield mainshock showed reverse motion on a steeply E dipping SE-NW striking fault (Gledhill *et al.*, 2011) followed by dextral strike-slip motion on the E-W striking

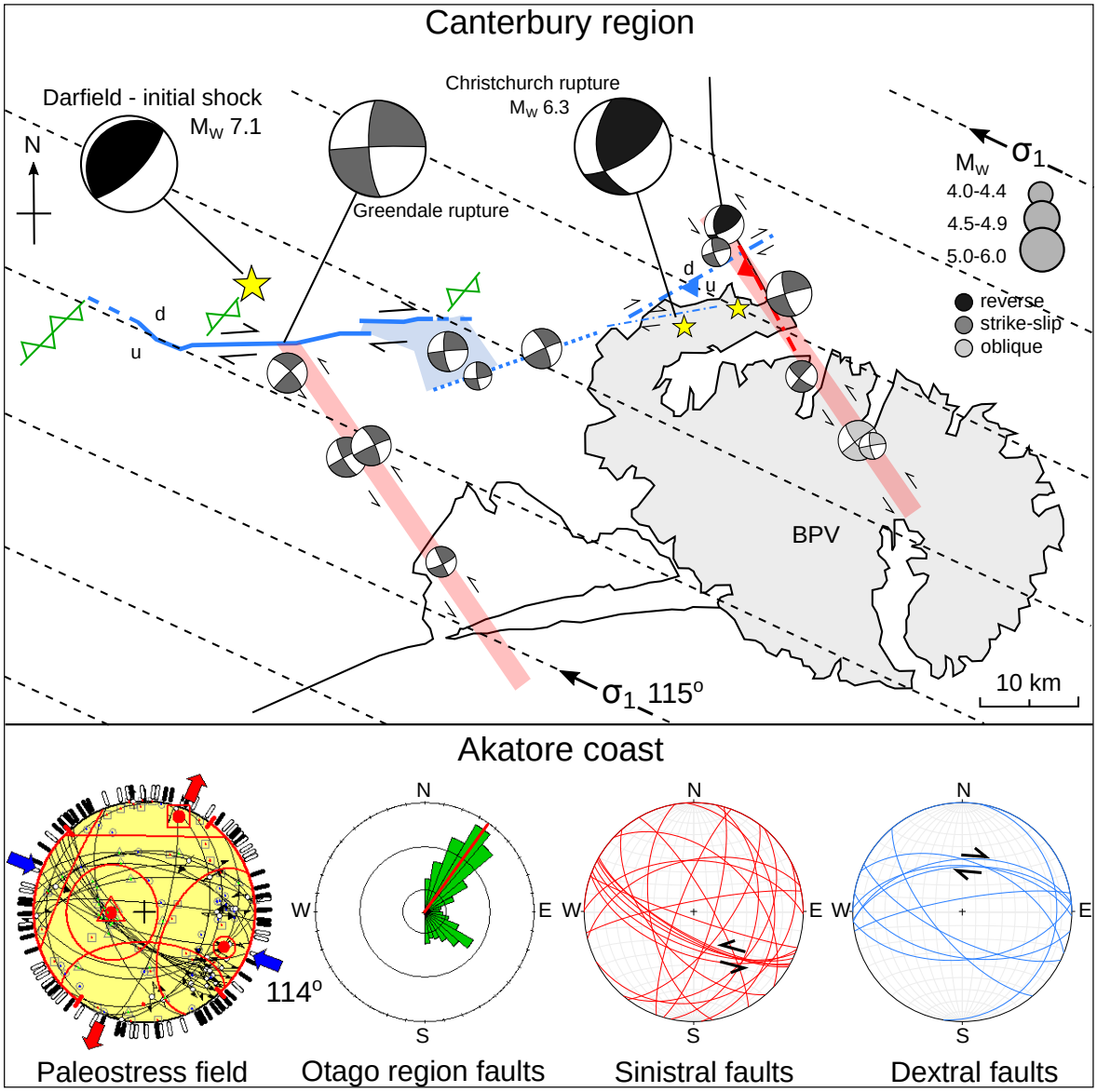

Figure 5.15: Schematic of the Canterbury region showing the 2010-2011 Christchurch earthquake sequence (adapted from Sibson *et al.* (2011, 2012)). Canterbury and Otago structures are coloured by E-W (blue) or SE-NW (red) orientation. Included are surface outcrop of Banks Peninsula volcanics (BPV); regional stress field (black dashed lines); major shock epicentres (yellow stars); the Greendale fault surface rupture (thick blue line); modelled subsurface ruptures of the Christchurch Mw 6.2 and Mw 6.0 aftershocks (dash-dot lines, teeth indicate dip direction), microearthquake lineament (blue dotted line); dilational stepover region of intense aftershock activity (blue-shaded area); aftershock lineaments (red-shaded bands); inferred reverse-slip trace (green lines with hollow teeth, dip unknown); and representative focal mechanisms of aftershocks and major shocks. Inset is the paleostress field at Akatore coast, dominant orientations of regional faults in Otago (Akatore Fault in red), and orientation of the conjugate basement fabric.

Greendale Fault from teleseismic focal mechanisms (Gledhill *et al.*, 2011; Sibson *et al.*, 2011). The Canterbury aftershock sequence included a number of strike-slip events on E-W striking structures (blue faults in Fig. 5.15) known to be part of the Late Cretaceous basement fabric (Ghisetti and Sibson, 2012; Sibson *et al.*, 2011) as well as a SE-NW alignment of strike-slip events (red-shaded bands in Fig. 5.15) inferred to be conjugate sinistral faults (Ghisetti and Sibson, 2012; Sibson *et al.*, 2011, 2012). The pattern of earthquake rupture observed during the Christchurch earthquake sequence closely matches the pattern of faulting observed at Akatore coast. Specifically;

1. The Otago region hosts many large NE-SW striking reverse faults, including the Akatore Fault, as seen in Chapter 4 with similar orientation to the first motion observed during the Canterbury sequence.

2. The basement fault fabric at Akatore is dominated by conjugate sinistral SE-NW and dextral E-W striking faults that partly reactivated the Late Cretaceous joint network, closely matching the known basement dextral E-W striking Late Cretaceous faults (including the Greendale Fault) and inferred SE-NW striking sinistral faults (from alignment of aftershocks) seen at Canterbury (Fig. 5.15). Furthermore the dip of some nodal planes of E-W striking and SE-NW striking focal mechanisms is very similar to the dip of conjugate E-W and SE-NW striking faults at Akatore coast (Fig. 5.15). It is therefore inferred that, in the current regional stress field, the basement fabric (such as that seen at Akatore) is widespread through both Otago and Canterbury regions and influences earthquake and aftershock distribution.

Chapter 6

Mineralogy and Microstructure of Brittle Deformation Features

Microstructural analyses are essential in investigating the deformation history of rocks. Microstructures offer insight into the relationships between mineralogy and structure which is critical to understanding the conditions of formation and subsequent alteration experienced. Comprehensive microstructural analysis is also necessary to provide adequate background before selecting samples for more detailed geochemical analyses.

Thin sections of 22 samples were prepared for optical analysis and cathodoluminescence (CL). 10 of these samples were further analysed using scanning electron microscopy (SEM). Description of sample preparation and methodology can be found in Chapter 3.4.

6.1 Host Rock

As described in Chapter 2.2 the Otago Schist protolith consisted of mostly turbiditic greywackes from the volcaniclastic Caples Terrane and the quartzofeldspathic Rakaia Terrane (Mortimer, 1993) which were subsequently metamorphosed during the Mid Jurassic (Adams and Robinson, 1993). The Chrystalls Beach Complex lithologies can be further separated (described below) into volcanogenic associated and sandstone-shale associated strata (Nelson, 1982) of pumpellyite-actinolite to biotite-zone greenschist facies (Adams and Robinson, 1993).

6.1.1 Volcanogenic associated rocks

Volcanogenic associated rocks make up approximately 10% of the Chrystalls Beach Complex and include; metabasalts, black manganiferous radiolarian metacherts, interbedded red and green argillites and chert, and pale green argillites (Fagereng, 2009; Nelson, 1982). With the exception of single green argillite outcrop none of the volcanogenic associated units were seen in the 2 km of detailed mapping and are not discussed further.

6.1.2 Sandstone-shale associated rocks

The remaining 90% of the Chrystalls Beach Complex, including the region of detailed mapping in this study, is made up of interbedded sandstone-mudstone turbidite deposits (Nelson, 1982). Mineralogy, as shown in Table 6.1 and Fig. 6.1A and B, consists of quartz, feldspar (both plagioclase and K-feldspar), sericite, and brown oxidised stilpnomelane with accessory muscovite, perthite, epidote, pumpellyite or chlorite, and opaque oxides. Lithics, particularly very fine-grained ones, of quartz and sericitic feldspar are also extremely common.

Table 6.1: Composition of sandstone-shale associated host rocks; average modal percentages determined by point counting.

Mineral	Modal percentage	Avg. grainsize
Lithics (quartz + feldspar)	30%	<1 mm (clast) 0.05 mm (individual grains)
Quartz	25%	0.5 mm
Sericite	15%	0.1 mm
Stilpnomelane	10%	0.5 mm
K-Feldspar	10%	0.5 mm
Plagioclase	5%	0.3 mm
Oxides	2%	1 mm
Muscovite	<1%	0.2 mm
Epidote	<1%	0.05 mm
Perthite	<1%	0.1 mm
Pumpellyite/chlorite	<1%	0.3 mm

In general, minerals except sericite and stilpnomelane are poorly sorted and rel-

atively angular. Quartz grains show patchy or sweeping undulous extinction, often contain small inclusions, and have irregular sutured boundaries with very small ($\ll 0.1$ mm) euhedral quartz grains. Plagioclase grains display albite twinning while K-feldspar rarely has any twins and is only distinguishable from quartz by it's flat extinction. Sericite forms a scruffy pale brown network in plain polarized light (ppl) and is generally concentrated along cracks and grain boundaries in the groundmass or as a psuedomorph. A weak foliation, corresponding to slaty cleavage in the field, can be seen in the groundmass where the long axis of sericite laths has aligned. Stilpnomelane is yellow to deep brown in both ppl and cross-polarized light (xpl) with varying pleochroism. It forms semi-circular patches of very fine, randomly oriented, bladed crystals. It also appears as large, fractured, euhedral psuedomorphs.

In addition varying amounts of calcite can be seen dependent on the samples proximity to the brittle faults described in Chapter 5.1.3. Calcite is assumed to have forming during late-stage brittle faulting and has therefore not been included in the primary host mineralogy.

Green quartz alteration zones

Hard green zones hosting quartz vein networks can often be seen in the schist (see Chapter 5.1.4). In thin section these zones are extremely silicic, made up of poorly sorted quartz grains with undulous extinction in an amorphous groundmass (brown in ppl). These zones closely match descriptions of green sandstones and mudstones by Fagereng (2009) who interprets them to be extensively chloritised rocks where chlorite has been altered to kaolinite on a microscopic scale as described by Craw *et al.* (1982). Minor opaque oxides, brown stilpnomelane, and muscovite can also be identified.

Two different quartz morphologies can be identified in these green zones; 1) very large (≤ 5 mm) grains with highly irregular boundaries, dusty inclusion rich surfaces, and regions of small subgrains defined by changes in extinction angles (Fig. 6.1C). And 2) regions of small (~ 0.1 mm), relatively inclusions free, polygonal grains surrounding larger (generally ~ 0.5 mm) grains with highly irregular boundaries and subgrain rich margins (Fig. 6.1D).

6.2 Fault-related Breccias

Mesoscopically breccia samples are clast supported with reddish calcite matrix and thin anastamosing veins surrounding angular schist clasts (Fig. 6.2A). Most samples can

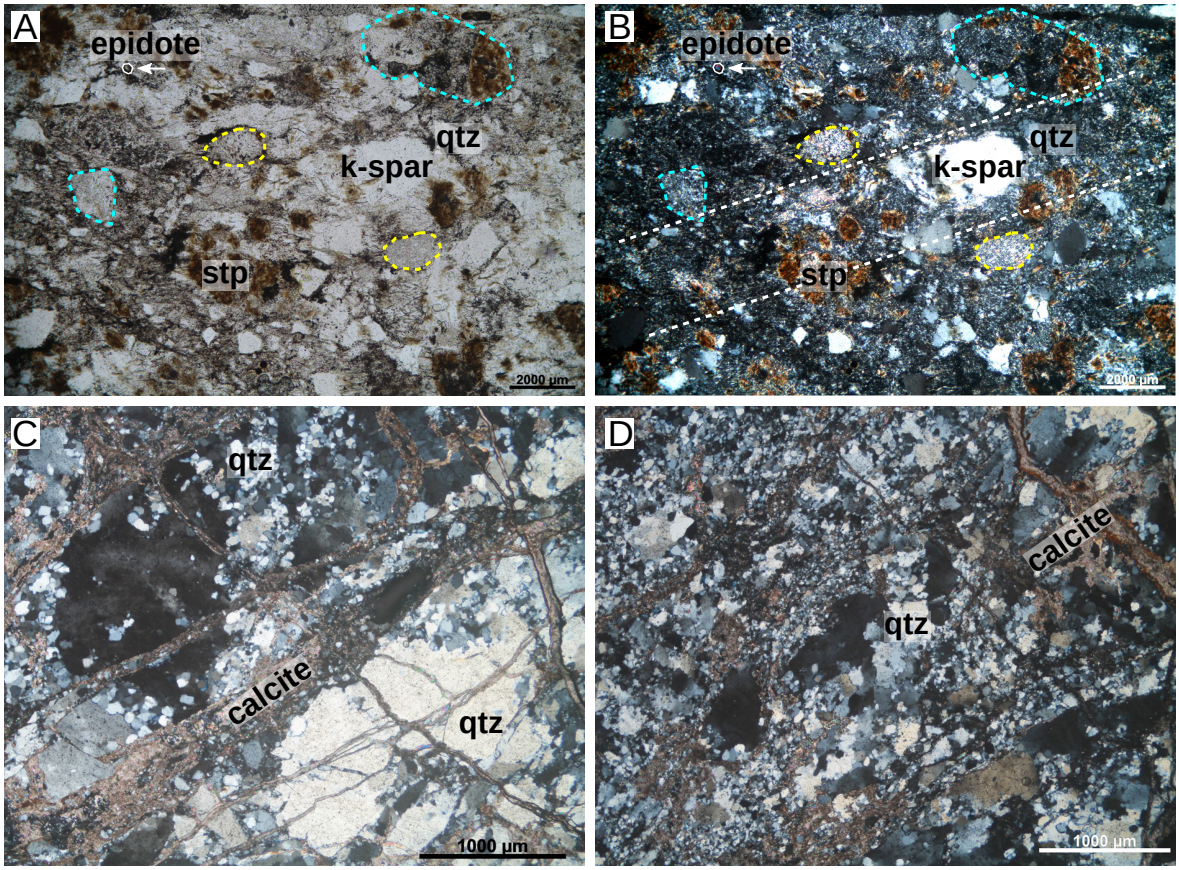

Figure 6.1: Mineralogy of host schist in ppl (A) and xpl (B) showing quartz (qtz), K-feldspar, brown stilpnomelane psuedomorph (stp), epidote, sericitized feldspars (yellow dotted lines), and relict quartzofeldspathic lithics (blue dotted lines) in a groundmass of quartz, feldspar, and brown sericite. Note the very faint foliation (white dotted lines) in the xpl image. C) Xpl image of quartz rich green alteration zone with massive grains and small subgrain rich margins and (D) a zone dominated by small polygonal grains and subgrains surrounding larger grains with highly irregular boundaries.

be defined as crackle breccias where clasts show minimal rotation relative to adjacent clasts and can clearly be geometrically realigned to original intact schist (Woodcock and Mort, 2008). Breccias have a clast:matrix ratio of $\geq$ 60% clasts to $\leq$ 40% red matrix or veins.

As expected breccia clasts show similar mineralogy to the host rock; quartz, K-feldspar, plagioclase, and sericite (Table 6.2 and Fig. 6.2B) are dominate. Angular quartz and feldspar grains are generally small ($\leq$ 0.4 mm) with phenocrysts $\leq$ 1 mm. Quartz grains still show undulous extinction and have irregular sutured boundaries. Groundmass is made up of fine grained quartz and feldspar in a pale brown sericite and phengite matrix. In larger clasts very weak foliation can still be picked out by tiny mica laths. EDS mapping of the groundmass indicates plagioclase is marginally more prevalent than K-feldspar and that both types of feldspars, although more commonly plagioclase, may be embayed in quartz (Fig. 6.2E). Embayment of quartz by feldspar is unrecognisable in thin section. Several samples show pleochroic brown (under both ppl and xpl) circular patches up to 0.1 mm diameter of randomly oriented, prismatic grains similar to the stilpnomelane seen in the host rock. Trace amounts of other minerals can be identified by EDS mapping including muscovite, zircon, and various iron oxides.

Red breccia matrix is controlled by the presence of patchy calcite which appears mottled brown in ppl. Calcite groundmass has filled in between schist clasts and often hosts quartz and feldspar phenocryst inclusions as well as lithic clasts of fine grained quartz and feldspar grains. Distinct (non-patchy) veins of calcite grains can be recognized within the calcite matrix. The margins of patchy calcite with other minerals, as well as calcite veins within calcite matrix, is delineated by brown colour in both ppl and xpl (Fig. 6.2C, D). EDS mapping indicates these brown margin zones are extremely iron-oxide rich (Fig. 6.2E).

Figure 6.2 *(following page)*: Mineralogy of fault-related breccias. A) Thin section scan showing relict schist clasts in red carbonate-rich matrix. B) Close up of relict schist clasts under cross-polarized light (xpl) showing quartzofeldspathic minerals. C) Close up of red carbonate-rich matrix in plain polarized light (ppl) showing brown staining on calcite margins. D) Xpl image showing large patchy calcite grains with brown margins. E) EDS image of the groundmass (plagioclase, alkali-feldspar, and calcite with iron oxide (red) margins) surrounding a quartz phenocryst.

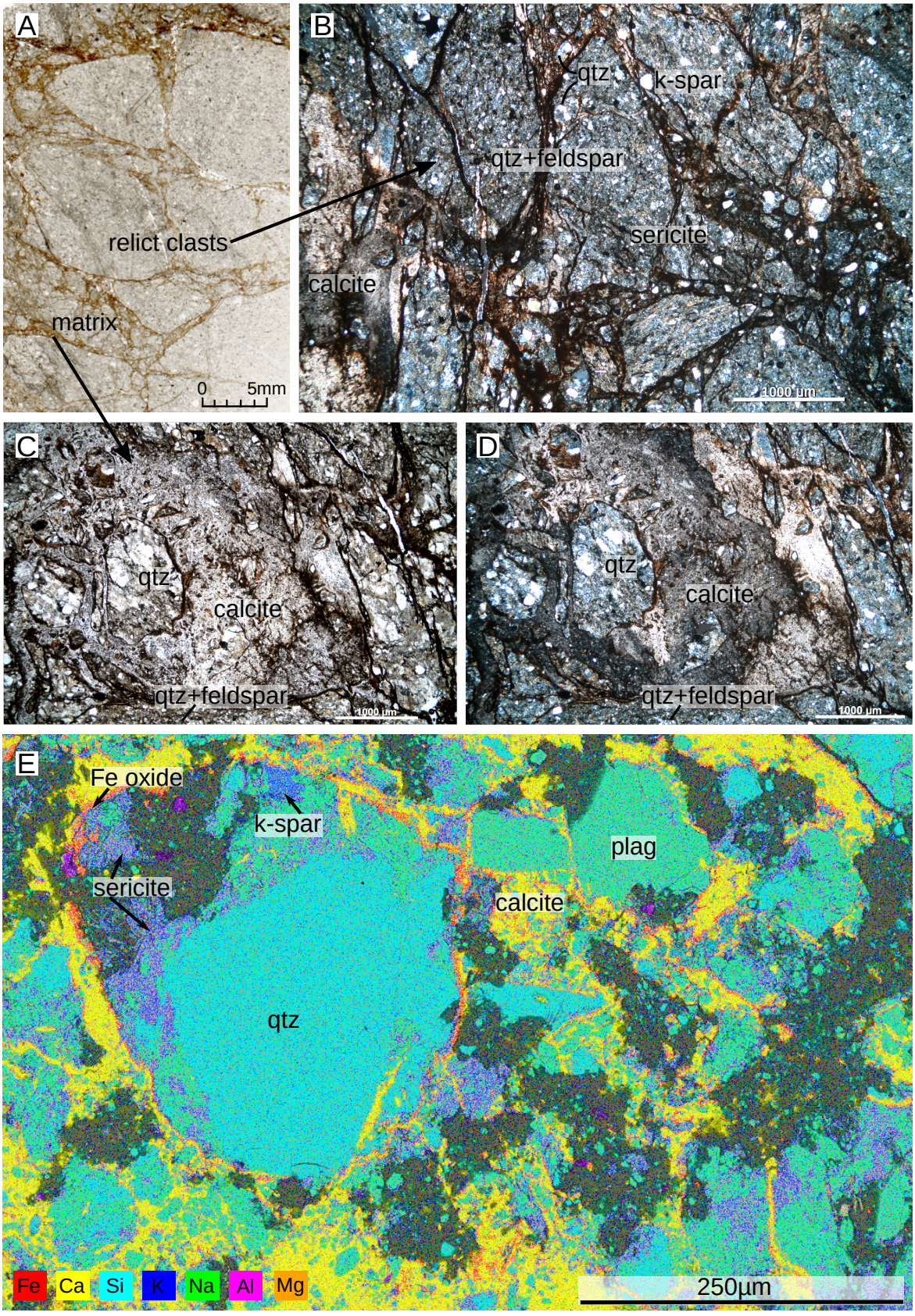
A
relict clasts
matrix
0
5mm
B
qtz
k-spar
qtz+feldspar
sericite
calcite
1000 µm
C
qtz
calcite
qtz+feldspar
1000 µm
D
qtz
calcite
qtz+feldspar
1000 µm
E
Fe oxide
k-spar
plag
sericite
calcite
qtz
Fe
Ca
Si
K
Na
Al
Mg
250µm

Table 6.2: Composition of breccia samples; average modal percentages determined by point counting.

Mineral	Modal percentage	Avg. grainsize
Calcite	40%	$\leq$ 2.5 mm
Quartz	25%	0.4 mm
Sericite	15%	0.1 mm
K-Feldspar	10%	0.4 mm
Plagioclase	5%	0.2 mm
Stilpnomelane	5%	0.1 mm

6.3 Fault-related Veins

Fault-related veins (see Chapter 5.1.4) can be identified at a variety of scales and are defined here as monomineralic (quartz or calcite) features which cross-cut multiple grains. Rare samples display extremely fine grained black anastamosing strands interpreted as phyllite (Fig. 6.3B). Quartz and calcite veins are mutually cross-cutting however visible displacement (sinistral or dextral) has only been identified in calcite veins which offset quartz veins or other calcite veins.

6.3.1 Quartz veins

Quartz veins are less common than calcite veins and tend to be large ($\geq$ 1 mm wide) structures that are continuous across the entire sample. The microstructure morphology of quartz veins falls into two categories depending on vein width. 1) In thin veins quartz grains tend to be tabular and equigranular with inclusion trails parallel to the vein direction (Fig. 6.3A). 2) In thick veins quartz grains are poorly sorted with large tabular grains adjacent to seams of very small polygonal grains. The contact between large grains with small polygonal quartz tends to be irregular while large grains surrounded by small grains are generally subgrain-rich (Fig. 6.3C).

6.3.2 Calcite veins

Three main types of calcite veins can be identified; 1) thin ($\leq$ 0.1mm wide) calcite veins in an anastamosing network around relict clasts and zones of patchy calcite groundmass (Fig. 6.4), 2) large fibrous calcite veins (Fig. 6.6), and 3) unconfined botryoidal veins (Fig. 6.7). These are described in detail below.

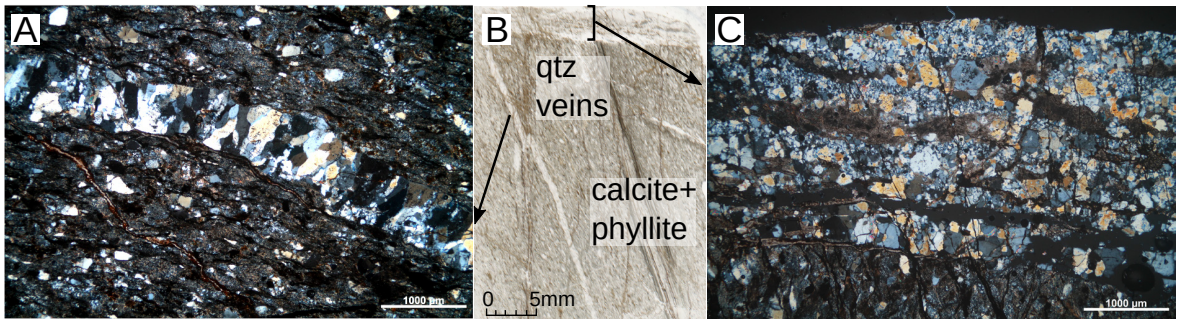

Figure 6.3: Microstructures seen in quartz veins. A) Xpl image of a thin quartz vein with tabular grains. B) Thin section scan showing a thin quartz vein (left) and a thick vein (top) along with an anastamosing calcite and phyllite vein network (right). C) Xpl image of a thick quartz vein showing tabular grains along the bottom margin and small polygonal grains surrounding phenocrysts with highly irregular margins in the centre of the vein.

Anastamosing veins

As noted in Section 6.2, thin calcite veins have dark brown margins in ppl and xpl (Fig. 6.4A, B) which EDS maps show are iron-oxide rich (Fig. 6.4C, E). Very thin calcite veins sometimes appear wholly brown and are completely oxidised in EDS images (Fig. 6.4E). At high resolution these Fe rich zones have a distinctive texture with irregular fibres (Fig. 6.5A) or cavities (Fig. 6.5B). Individual calcite grains cannot be easily identified, in some cases very fine fibrous textures occur on the margins of slightly larger veins (Fig. 6.4A). Sweeping extinction is used to delineate grain boundaries, in rare cases a medial surface, and thin differently oriented calcite margins in veins without dark brown staining. Very thin calcite veins may have an interwoven texture (Fig. 6.4D) and often fractures feldspar phenocrysts (Fig. 6.4D, E).

Fibrous vein network

Fibrous calcite veins are confined to extensional foliation parallel faults. These veins are typically about 5 mm wide and are laterally continuous (see Chapter 5.1.4). Individual fibres are generally very thin (Fig. 6.6A-D) however there are rare cases with more blocky fibres of $\leq$ 0.5 mm wide (Fig. 6.6E, F). Fibrous veins are antitaxial with a dark medial surface present. Some display further surfaces delineated by dark lines or colour changes. Fibrous veins rarely display the brown margins seen in thin calcite veins but interior sections are often stained red brown in ppl and xpl (Fig. 6.6A). EDS maps do not show significant chemical changes across fibrous veins correlating to

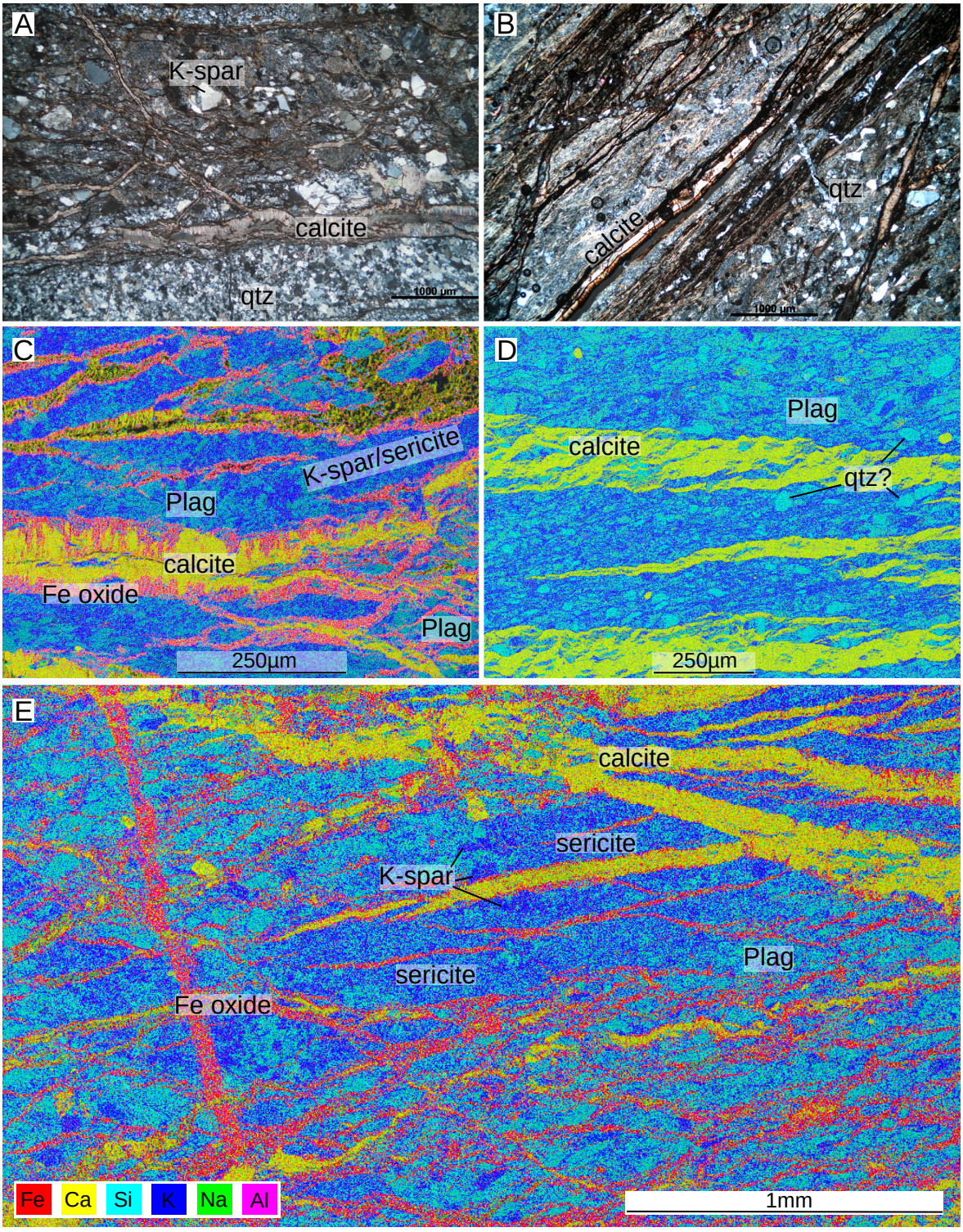

Figure 6.4: Xpl (A-B) and EDS (C-E) images of microstructures seen in anastamosing calcite veins.

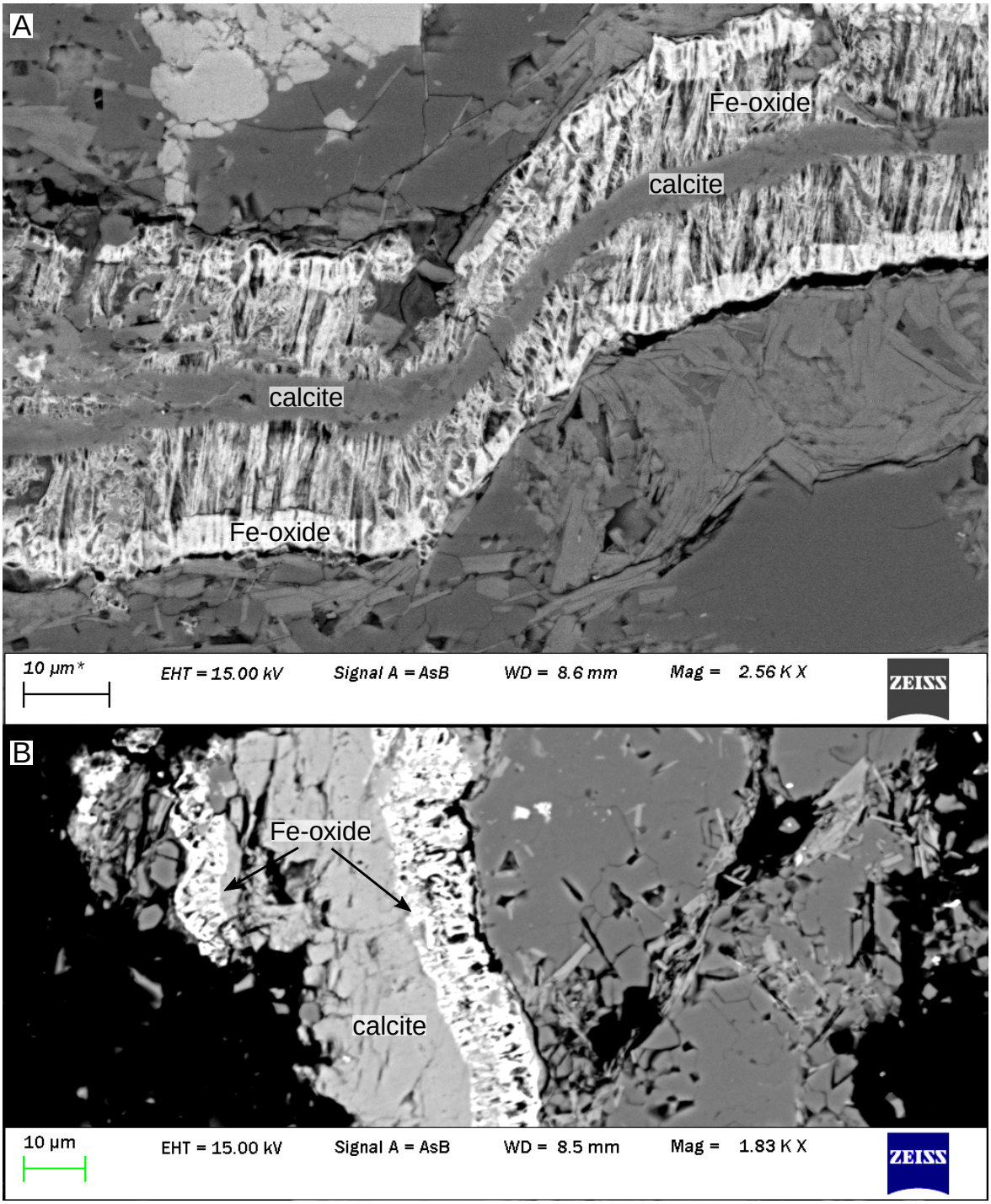

Figure 6.5: SEM images of the textures seen in oxidised Fe-rich along the margins of anastamosing calcite veins.

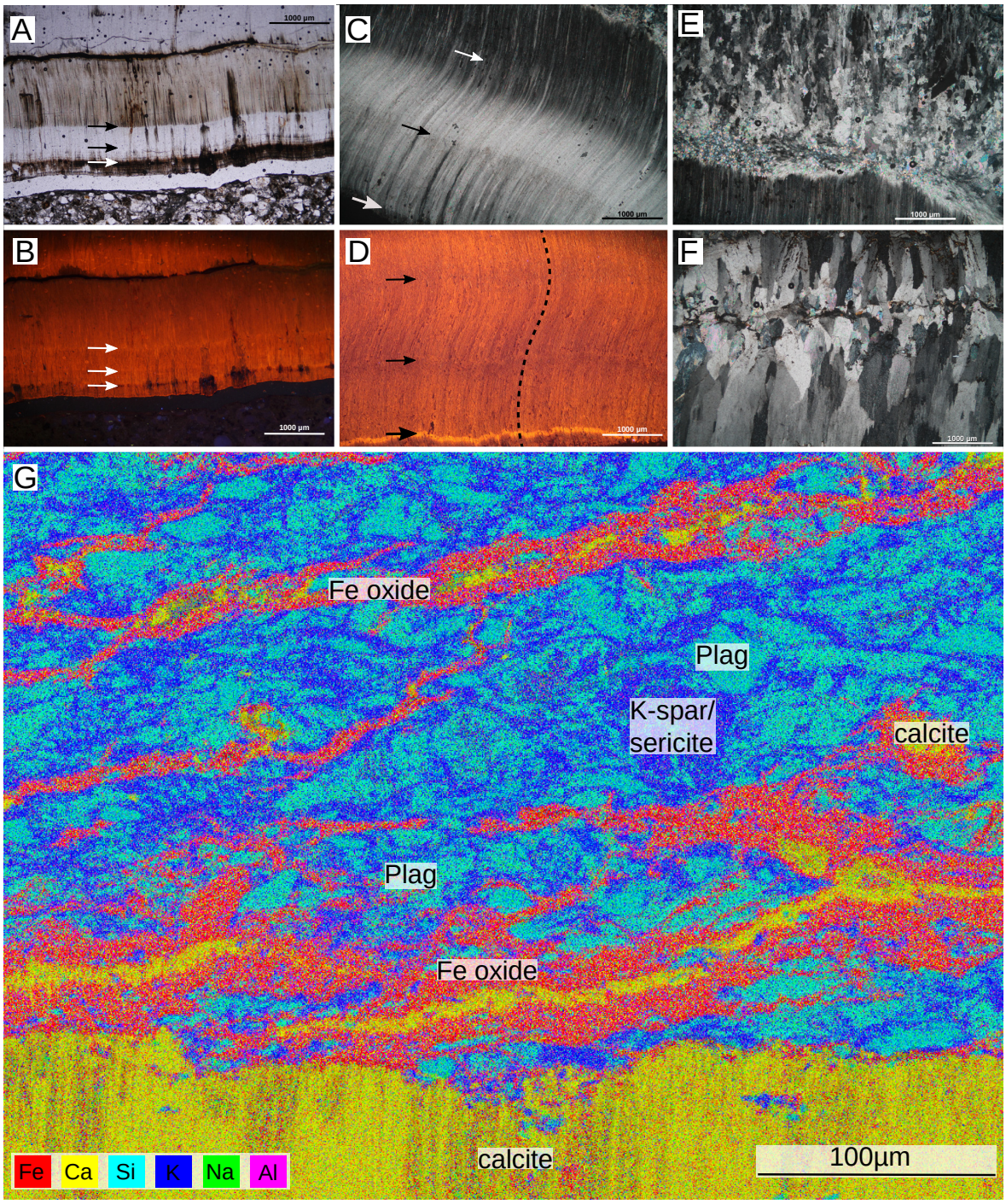

Figure 6.6: Optical and CL images of microstructures seen in straight (A-B), curved (C-D), and blocky (E-F) fibrous calcite veins. Minor zoning in CL correlating to colour changes in thin section are noted with black or white arrows. (G) EDS map showing the interaction between a fibrous vein (along the bottom) and anastamosing veins with oxidised iron-rich margins in a seriticised feldspar groundmass.

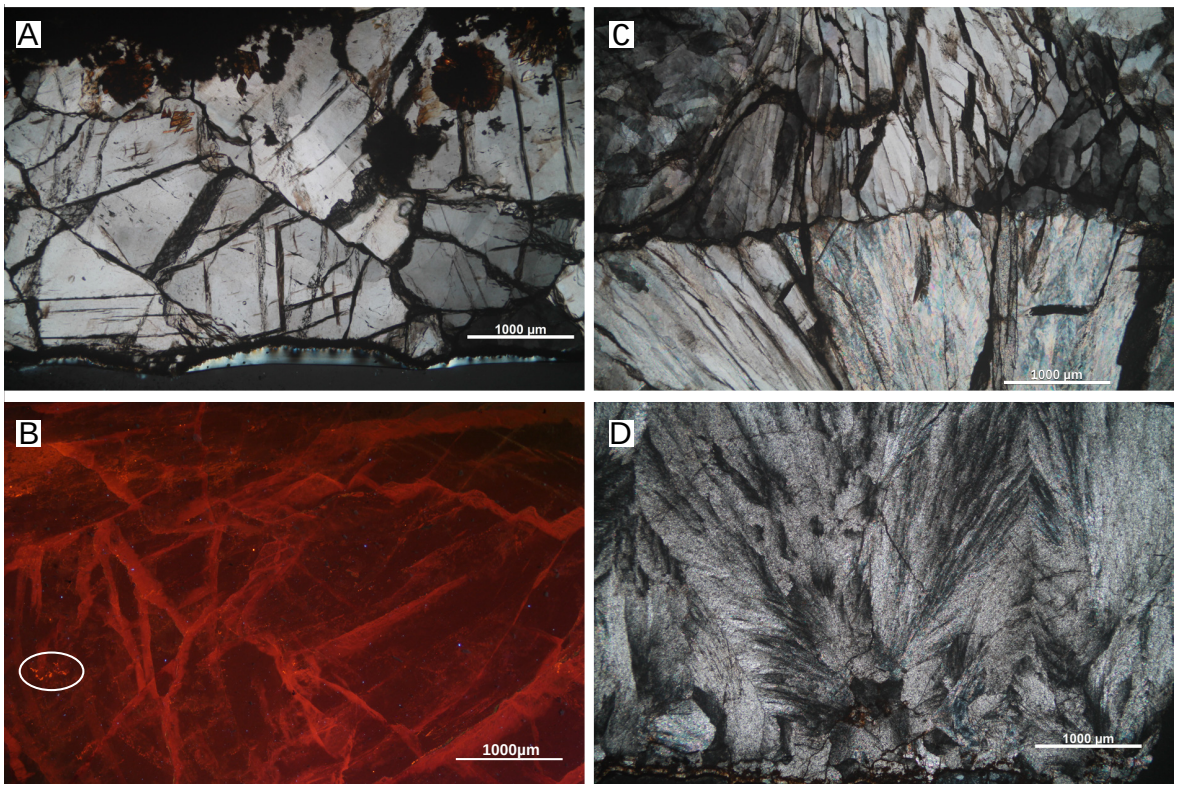

Figure 6.7: Xpl (A, D-E) and CL (B) images of botryoidal calcite veins. Spots of fluorescence have been circled in white (B) and scattered orange and blue flecks can be seen throughout the image.

colour changes. In rare cases where fibre growth is curved across the vein faint CL bands do not appear to correlate with changes in fibre orientation (Fig. 6.6C, D). No fluid inclusions could be seen. Most fibrous veins are not strongly fluorescent, likely due to increased Fe proportions, and do not show significant zoning under CL. Zoning correlated with colour changes and medial surfaces can be identified in some fibrous veins (see arrows in Fig. 6.6A-D) as well as gradual changes in luminescence parallel to the vein wall (Fig. 6.6B). Fibrous veins often contain clasts of schist along vein margins.

Botryoidal calcite

Botryoidal calcite veins, inferred to have mineralised in cavities where joints intersect and on top of breccias, are comprised of large ($\geq$ 1 mm) blocky grains with curved or slightly radiating faceted surfaces. An irregular medial surface can be seen between grains where growth has been inhibited (Fig. 6.7C). Perfect rhombohedral cleavage can be seen in polygonal grains along with rare simple twins (Fig. 6.7A). Radiating grains

(Fig. 6.7D) often contain curved fractures parallel to the fanning medial surface. Very small primary fluid inclusions with vapour bubbles can be identified but are rare and of poor quality. More common are trails of tiny secondary fluid inclusions on planes dipping into grains. Like the fibrous veins, botryoidal veins do not strongly fluoresce or demonstrate significant zoning under CL (Fig. 6.7B) and may reflect a more Fe-rich composition.

6.4 Discussion

Mineralogy and the development of microstructures offer insight into the deformation and fluid history of rocks at Akatore coast. The microstructures at Akatore coast can broadly be broken down into three categories; 1) host rock microstructures associated with regional metamorphism during the Jurassic, 2) microstructures associated with post-Cretaceous brittle deformation, and 3) microstructures associated with very late stage, unconfined mineralization.

6.4.1 Regional metamorphism microstructures

Excluding brittle deformation features (described above in Section 6.3), samples collected along Akatore coast are all compositionally similar; quartzofeldspathic and lithic-rich. Detrital clasts are poorly sorted and angular implying relatively little reworking. Quartz grains have clearly undergone deformation; patchy and sweeping undulous extinction is pervasive, large grains commonly display irregular boundaries with small polygonal grains, and subgrains are widespread. These are classic indicators of bulging recrystallization (BLG), transitioning into subgrain-rotation recrystallisation (SGR), where dislocations have migrated to form subgrain boundaries (Hirth and Tullis, 1992; Stipp *et al.*, 2002). There is no evidence for quartz recovery by grain boundary migration or extensive SGR limiting the maximum temperature experienced to $< 500°C$, most likely to $\sim 400°C$ in the BLG-SGR transition range (Stipp *et al.*, 2002). This fits well with Fagereng and Cooper (2010a) who define the maximum temperature of metamorphism at Chrystalls Beach Complex as $< 350°C$.

The majority of minerals seen in host rock samples are detrital with the exception of sericite and stilpnomelane. Sericite, an alteration product related to the breakdown of feldspars to white mica, is widespread throughout all samples in both the groundmass and as feldspar psuedomorphs. At high resolutions the margins of quartz grains may be embayed by sericitized plagioclase and phengite indicating authigenic growth after

the emplacement of quartz. Stilpnomelane also occurs as psuedomorphs although the original mineral is unknown. Stilpnomelane in the Otago Schist is attributed to the alteration of chlorite in the presence of iron oxides (Fagereng and Cooper, 2010a; Li *et al.*, 2000). Certainly the presence of multiple authigenic minerals implies a history of metasomatism and significant fluid flux throughout the region.

6.4.2 Fault-related microstructures

Microstructures associated with brittle deformation include; fault-related breccias, and fault-related quartz and calcite veins. Syntectonic mineralisation along Akatore coast is dominated by carbonates. Mutually cross-cutting quartz and calcite veins indicate that mineralisation of these veins occurred during the same fluid event or from later remobilisation. Widespread undulous extinction and lenses of subgrains in large quartz veins indicate that the grains have experienced mild deformation.

There is no strong microstructural evidence for multiple episodes of faulting. Breccia clasts show only minor rotation relative to adjacent clasts and are inferred to have experienced relatively little reworking. Optically, syntectonic fibrous veins (large fibre length:width ratio) show multiple surfaces defined by colour changes which look like crack-seal lines and rare curved fibres indicating multiple phases of calcite precipitation or precipitation during incremental faulting. However calcite veins, including fibrous ones, show almost no zoning under CL. If the veins were formed from multiple precipitation events the different calcite phases should appear under CL. Thin quartz veins of tabular grains forming blocky fibres host inclusions bands parallel to vein direction which again appear to indicate crack-seal growth but are not sufficient evidence on their own (Hilgers and Urai, 2002). Given the lack of strong CL banding and faceted fibres it may be inferred that the initial opening increment of the vein was small, suppressing crystal growth and allowing variations in orientation without mechanical coupling across the vein (Hilgers and Urai, 2002).

Part of the difficulty in determining different mineralisation stages is the absence of a clear selvage zone between the vein and country rock. Most veins are antitaxial, containing an irregular medial surface formed due to competition for space when crystals have grown inwards from the vein margins. Extensive alteration has occurred along the margins of anastamosing calcite veins and matrix. These oxidised zones have distinctive weathering textures and are likely the remnants of an iron carbonate (e.g. ankerite). This widespread oxidisation is interpreted as late-stage weathering which occurred when the rocks were exposed at, or near, surface. Preferential weathering

along veins margins may account for absence of any recognizable selvage zone.

It should be noted that there have been no occurrences of fibrous veins being cross-cut by other features and that there are rare examples of fibrous veins incorporating pods of schist. From this it is interpreted that foliation-parallel veins formed after the formation of steeply dipping veins and breccias.

6.4.3 Late stage mineralization

The final type of microstructures seen at Akatore coast are those associated with late stage mineralisation into relatively unconfined spaces. This is seen in the botryoidal calcite where very large blocky grains have been able to form due to lack of competition for space. Radiating grains with undulous extinction and irregular surfaces between crystal clusters indicates that there was some slight competition for space and minor deformation still occurring.

Chapter 7

Geochemistry

The Akatore coast hosts an extensive network of mineralised veins (described in Chapters 5.1.4 and 6.3) which will have required significant fluid flux to form. Carbonate mineralisation is particularly prolific which is interesting as the composition of the host rock and nearby units are not particularly Ca-rich. Geochemical analyses of carbonate features (breccia matrix, paired quartz-calcite veins from steeply dipping joints, fibrous foliation parallel calcite veins, and botryoidal calcite) were undertaken to determine the fluid history preserved at Akatore coast as well as potential fluid sources. Methodology for individual analyses can be found in Chapter 3.5.

7.1 Stable Carbon/Oxygen Isotopes

Carbonate stable isotope geochemistry uses the ratio of $^{13}C/^{12}C$ (reported as $\delta^{13}C$) and $^{18}O/^{16}O$ (reported as $\delta^{18}O$) to investigate fluid-rock interactions by assuming that the isotopic values measured fall somewhere on a spectrum between original fluid or rock isotopic values and isotopic equilibrium between the two. Isotope values are reported relative to international standards; VPDB for $\delta^{13}C$, e.g.

$$\delta^{13}C = [\frac{(^{13}C/^{12}C)_{sample}}{(^{13}C/^{12}C)_{VBPDB}} - 1] * 1000 \tag{7.1}$$

and using the formula of Equation 7.1 relative to SMOW for $\delta^{18}O$. Negative values with respect to the standards equates to an increase in lighter isotopes while positive values equate to an increase in heavier isotopes. In general oxygen isotopic values are dependent on the isotopic composition and temperature of the source fluid while carbon isotope values reflect the carbon source (Nelson and Smith, 1996).

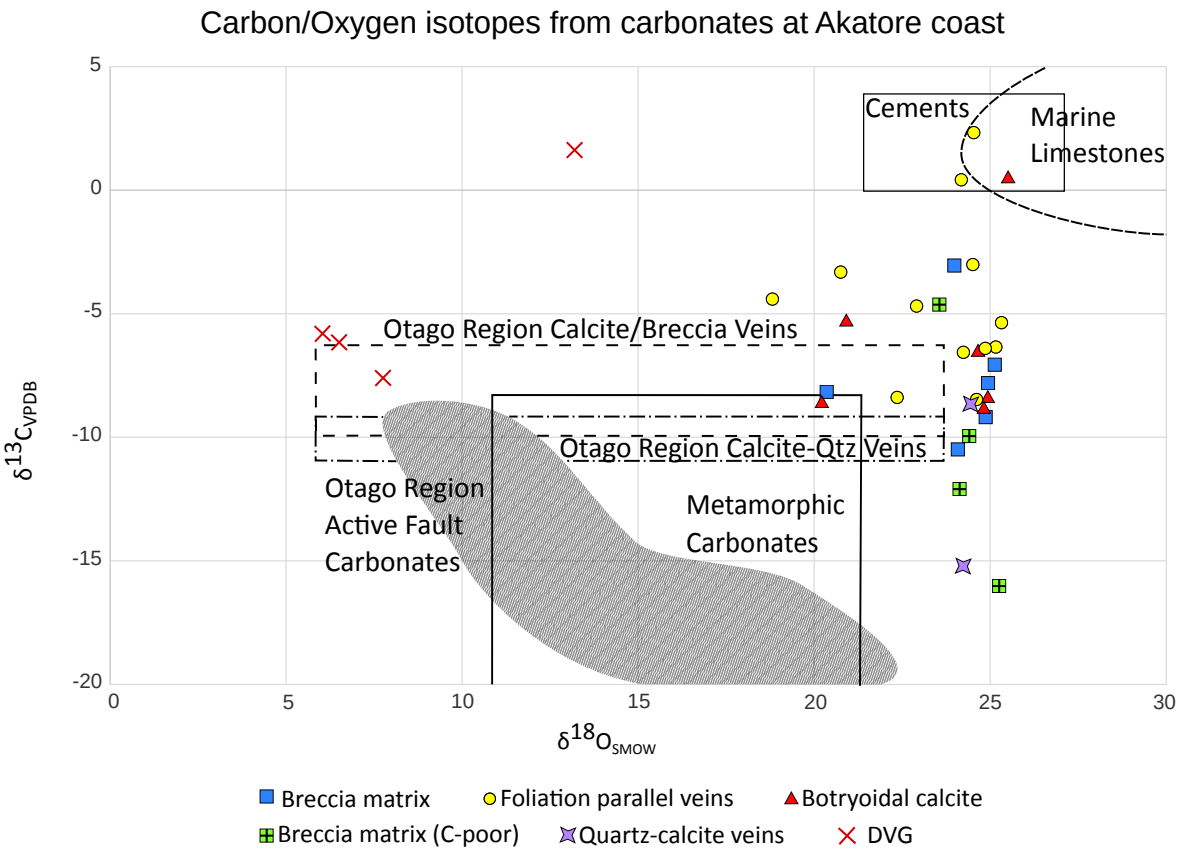

Figure 7.1: Average δ^{13}C and δ^{18}O values of carbonate features found at Akatore coast. References fields from; marine limestones (Nelson and Smith, 1996), cements (Nelson *et al.*, 1988), metamorphic carbonates (Templeton *et al.*, 1998; Upton *et al.*, 2000), active fault, calcite/breccia, and calcite-quartz carbonates (Templeton *et al.*, 1998), Dunedin Volcanic Group (DVG) (Price *et al.*, 2003).

As described in Chapter 3.5 all samples were duplicated to evaluate carbonate homogeneity within samples. Three sample vials experienced "suspected air leaks" during sample preparation, data from these were excluded and homogeneity of the sample could therefore not be evaluated. Isotopic values shown in Figure 7.1 have been averaged between the duplicated measurements. Samples were relatively homogeneous with an average standard deviation between duplicated samples of ± 0.09 δ^{18}O and ± 0.13 δ^{13}C across the entire dataset. The δ^{13}C values of some duplicated samples were much less homogeneous, with up to ± 0.55 in sample AK-14, compared to a maximum deviation of ± 0.27 δ^{18}O in sample AK-15.

In addition to homogeneity, the signal strength from each sample was evaluated. Four breccia samples had low peak CO_2 voltage ($\leq$ 2) compared to the rest of the dataset (CO_2 voltage $\simeq$ 6), these samples were included within the final dataset as a separate carbon-poor category. Low signal strength in this case is believed to have occurred due to a low carbonate:total sample ratio and likely represents the incorporation of schist fragments during the crushing stage.

As shown in Figure 7.1, carbonates at Akatore coast have a wide range of δ^{18}O and δ^{13}C values. However, although δ^{18}O values range from 18.8 to 25.5, the majority of samples fall between 23.5 to 25.5. In comparison, δ^{13}C values vary between -16.0 (soil weathering to reduction of organic material values; Nelson and Smith, 1996) to 2.3 (marine limestone type values; Nelson and Smith, 1996) with the bulk of samples falling between -10.5 to -0.8. There is no obvious correlation between isotopic composition with either feature type or spatial distribution along the coast.

7.2 Radiogenic Strontium Isotopes

^{87}Sr/^{86}Sr values within samples, with the exception of AK-23, are relatively uniform and there is relatively little difference across the entire sample suite (Table 7.1; Fig. 7.2). Overall ^{87}Sr/^{86}Sr values range between 0.705739 (AK-42) – 0.706818 (AK-23). Estimated ^{87}Rb/^{86}Sr is generally low ($<$ 0.0006) except in breccia samples AK-17 and AK-23 ($\leq$ 0.04538), likely due to ablation of micas during analysis. Low Rb concentrations mean that there has been little to no change in ^{87}Sr/^{86}Sr values when age correcting for 25 Ma.

Table 7.1: Age corrected (25 Ma) average $^{87}Sr/^{86}Sr$ values for each sample and amount of deviation from the average within sample runs.

Sample	Avg $^{87}Sr/^{86}Sr$*	$^{87}Sr/^{86}Sr$ range	Feature type	Sample tracks	MWSD
AK-33	0.70601	±0.00006	Breccia	5	3.4
AK-17	0.70634	±0.00011	Breccia	5	7.9
AK-23	0.70623	±0.00032	Breccia	4	55.0
AK-42	0.70583	±0.00008	Quartz-calcite vein	5	4.7
AK-34	0.70615	±0.00012	Foliation-parallel vein	6	14.0
AK-40	0.70589	±0.00008	Foliation-parallel vein	5	3.2
AK-24	0.70633	±0.00005	Botryoidal calcite	5	2.0

* $^{87}Sr/^{86}Sr$ and estimated $^{87}Rb/^{86}Sr$ values for each run can be found in Appendix E.

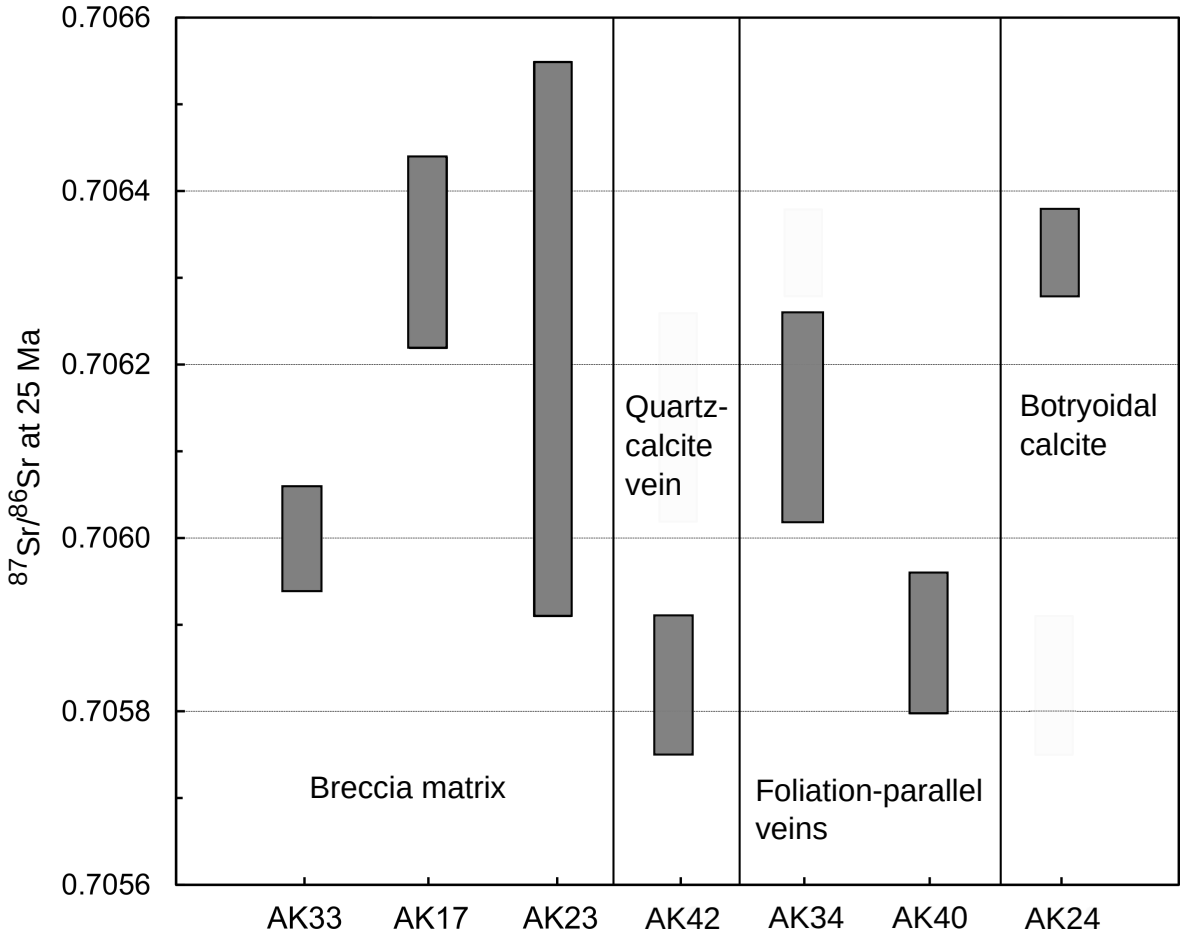

Figure 7.2: Weighted average $^{87}Sr/^{86}Sr$ composition of samples from Akatore coast, age corrected to 25 Ma for $^{87}Rb/^{86}Sr$ decay. Box heights are 2 s.d.

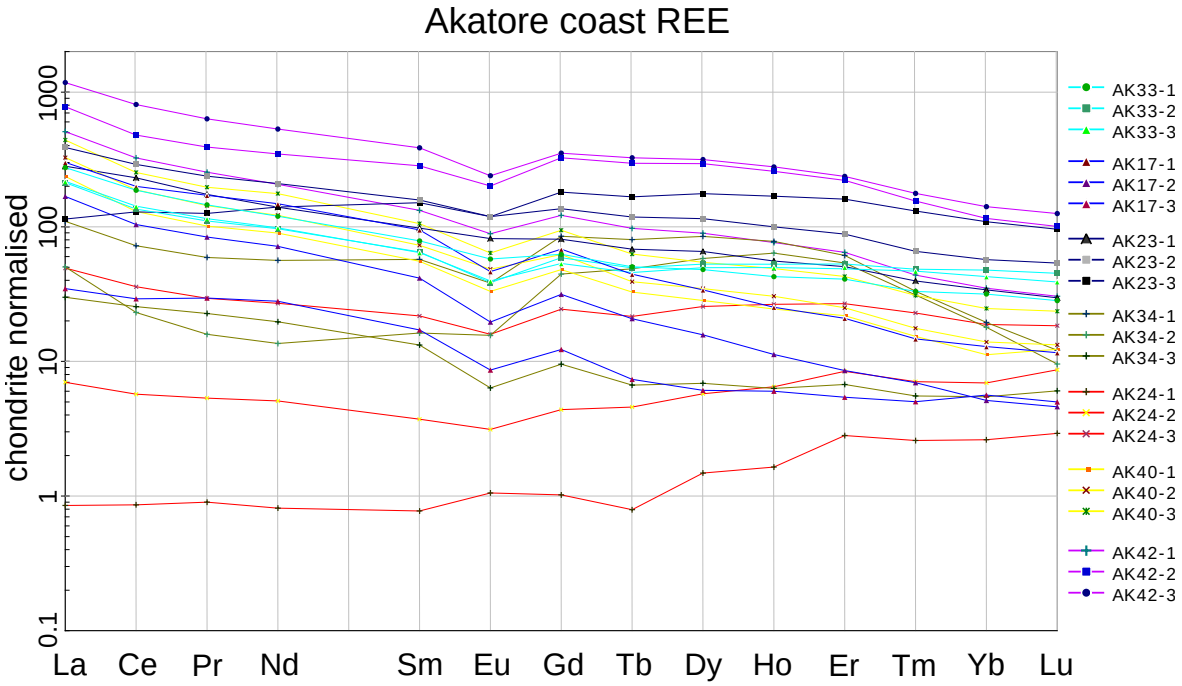

Figure 7.3: REE plots for all 3 runs of individual samples normalised to chondrite values from Sun and McDonough (1989).

7.3 Trace Elements

As shown in Figure 7.3 rare earth element (REE) patterns are fairly parallel across all samples. Total REE concentration ranges across 3 orders of magnitude and loosely follows the pattern for quartz-calcite vein and breccia matrix, foliation parallel veins, and botryoidal calcite with highest to lowest REE concentrations respectively. Light REE are slightly enriched relative to heavy REE and have a negative trend. Heavy REE trends have a slight negative slope, mostly in Er and heavier REE. There is a persistent negative Eu anomaly in almost all samples. Botryoidal calcite (sample AK-24) and breccia matrix sample AK-23 (run 3) have flat REE patterns to slight enrichment of heavy REE.

7.4 Discussion

7.4.1 Cenozoic geology near Akatore coast

As concluded in Chapter 5, fault-related carbonates are locally confined to reactivated Late Cretaceous exhumation joints. The faults are inferred to have ruptured under the current stress configuration from paleostress inversion of kinematic data (Chapter

5.3.2). Formation of fault-related carbonate veins and breccias is therefore restricted to the past $\sim$ 25 Ma (i.e. Miocene or younger mineralisation). Rock deposited after exhumation of the schist in the Late Cretaceous must therefore be considered for when modelling the fluid:rock interactions during the Miocene.

Sedimentary sequences

Sedimentation in the Southland and Canterbury basins and Otago region includes a marine transgressive sequence from the Late Cretaceous up to the Late Eocene-Oligocene (marked by a regional paraconformity) followed by a regressive sequence (Norris *et al.*, 1978). This sediment sequence is made up of conglomerates, quartzose sandstone, greensand, mudstone, and bioclastic limestone with minor coal (GNS, 2012; Norris *et al.*, 1978; NZPAM, 2013). The Takapu-1A well, which was drilled offshore of Taieri Mouth in 1978, shows a sedimentary sequence of alternating sandstone and mudstones with a thin marl unit (NZPAM, 1978). Inland of Akatore coast are outcrops of fluvial quartz gravels and sands with local coal deposits belonging to the Taratu Formation overlain by marine sands of the Wangaloa Formation and the Abbotsford Formation mudstones (Bishop, 1994; McMillan and Wilson, 1997; Norris and Turnbull, 1996). Finally, the sequence is capped by a number of Tertiary sandstones and greensands (Green Island, Burnside, Concord, and Caversham units; Bishop, 1994; McMillan and Wilson, 1997). It is believed these sediments formed a relatively thin overburden on top of the, now exposed, modern coastal platform along Akatore coast with a maximum thickness of 1.5 – 2 km (Norris *et al.*, 1978, J. Lindqvist pers. comm.). As described above, faults hosting carbonate features at Akatore coast are of Miocene or younger age so have formed after deposition of the Cenozoic sediments. These faults are interpreted have formed at shallow depths as they are located just below the basal unconformity between the schist and the sedimentary sequence. Assuming a 25°C/km geothermal gradient during exhumation (Fagereng and Cooper, 2010a; Mortimer, 2000) fault-related veins will have formed under low temperatures of $\leq$ 50°C. Ideally the temperature conditions at vein formation would also be confirmed by fluid inclusion analysis but the size, poor quality of primary inclusions, and anticipated low temperatures meant that this technique was not pursued.

Dunedin Volcanic Group

The Dunedin Volcanic Group (DVG) includes the Dunedin shield volcano and monogenetic Waipiata Volcanic Field (Coombs *et al.*, 1986). It is located in Eastern and

Central Otago and extends as far south as Kaitangata, inland of Chrystalls Beach (Bishop, 1994; Coombs *et al.*, 2008; GNS, 2012). The DVG was active from 25 – 9 Ma (Dunedin volcano erupted between ∼16 – 10.1 Ma; Coombs *et al.*, 2008; Timm *et al.*, 2010), i.e. at the same time that carbonate features are inferred to have formed. Deposits are made up of basanite through phonolite which have been erupted through the schist basement from a shallow mantle source with further pressure-driven differentiation at various depths in the crust (Coombs *et al.*, 2008; Hoernle *et al.*, 2006; Timm *et al.*, 2010).

7.4.2 Fluid flow models

Given the disparity between variation in $\delta^{18}O$ and variation in $\delta^{13}C$ two models of fluid flux can be proposed; 1) carbonates have precipitated from fluids derived through mixing of multiple reservoirs with different carbon and oxygen isotope signatures and 2) carbonates have precipitated from a fluid which is isotopically homogeneous except for carbon which is decoupled within the system. Model 2 is not necessarily exclusive of a mixed fluid model but requires that mixing does not significantly change the O and Sr isotopic composition.

Together C, O, and Sr isotopic compositions offer insights into determining which of these models is more credible. $\delta^{18}O$ acts as a tracer of the source and pathway of water molecules, the $\delta^{18}O$ ratio in authigenic minerals is therefore largely controlled by the fluid composition and temperature (Banner, 2004; Hoefs, 2009; Hudson, 1977). In contrast $^{87}Sr/^{86}Sr$ records the source and pathway of dissolved ions so is strongly controlled by the mineralogy and age of the source rocks and acts as a tracer for Ca mobilization (Banner, 2004). $\delta^{13}C$ is strongly dependent on the original sources of carbon (Hudson, 1977).

One of the disadvantages faced in this study is that $\delta^{18}O$ fractionation is strongly temperature dependent at low temperatures, meaning the $\delta^{18}O$ variations seen in Figure 7.1 could be accommodated by relatively small changes in temperature rather than mixing. $\delta^{18}O$ values of 23 – 26, matching the range seen in Akatore samples, are predicted for temperatures between 35 – 50°C using the Golyshev *et al.* (1981) equation for fractionation in low temperature carbonate systems. Therefore, temperature dependent oxygen isotopic fractionation is assumed to account for $\delta^{18}O$ variation hereafter.

One advantage in studying $^{87}Sr/^{86}Sr$ values is that Sr, but not Rb, will preferentially substitute for Ca in the crystal lattice of carbonate minerals (Banner, 2004). This accounts for the very small estimated $^{87}Rb/^{86}Sr$ ratios in the Akatore samples and

means that age corrections to the $^{87}Sr/^{86}Sr$ values should be very small. $\delta^{13}C$ is slightly more complex. $\delta^{13}C$ ratios exhibit only minor temperature dependent fractionation, but may vary widely depending on the proportion of organic-derived to oxidised carbon (Hudson, 1977) and, to a much lesser extent, fluid pH (Rye and Ohmoto, 1974).

Mixed fluid source model

In a classic fluid mixing model, two or more fluid reservoirs with different isotopic signatures physically mix to produce a range of intermediate isotopic compositions which are passed on to carbonates precipitated from these mixtures. As seen in Figure 7.1 three Akatore samples have positive $\delta^{13}C$ values and $\delta^{18}O$ values > 23 – an isotopic composition typically seen in marine limestones. The majority of samples have $\delta^{13}C$ values in the range of -15 to -5 which are generally associated with soil weathering processes and oxidation of organic matter (Nelson and Smith, 1996).

As discussed above the sedimentary overburden will have included lenses of Kaitangata coal and marine sediments belonging to the Taratu and Wangaloa Formations. Fluids circulating in these sediments could have acquired isotopic signatures representative of both limestone and coal prior to mixing during migration down to the basement schist. However the $\delta^{18}O$ composition does not fully support this model. If mixing of multiple fluids with no previous history of interaction had occurred then some variation in $\delta^{18}O$ would be expected along a subvertical trend line (e.g. the active fault carbonates field from Templeton *et al.*, 1998) instead of the vertical distribution seen in Figure 7.1. There is also poor agreement in $^{87}Sr/^{86}Sr$ values for this model. Like $\delta^{18}O$, if isotopic composition was purely representative of the different sources being captured then the Sr isotopes should reflect different source rocks instead of the homogeneous $^{87}Sr/^{86}Sr$ signal seen in Akatore samples.

Decoupled carbon model

The alternative model is a decoupled system where a fluid source with constant oxygen and Sr isotopic ratios has acquired $\delta^{13}C$ signatures *without* the associated $\delta^{18}O$ and $^{87}Sr/^{86}Sr$ signatures from various carbon sources. This model allows for a relatively constant $\delta^{18}O$ and $^{87}Sr/^{86}Sr$ ratio paired with wide ranging $\delta^{13}C$ values present in the data. As noted earlier, a decoupled model is not exclusive of the mixing model but does require a mechanism for keeping relatively constant $\delta^{18}O$ and $^{87}Sr/^{86}Sr$ compositions if mixing does occur. Some possible ways to meet this requirement would be to have sufficient residence time within the fluid pathway for isotopic equilibrium to occur or for

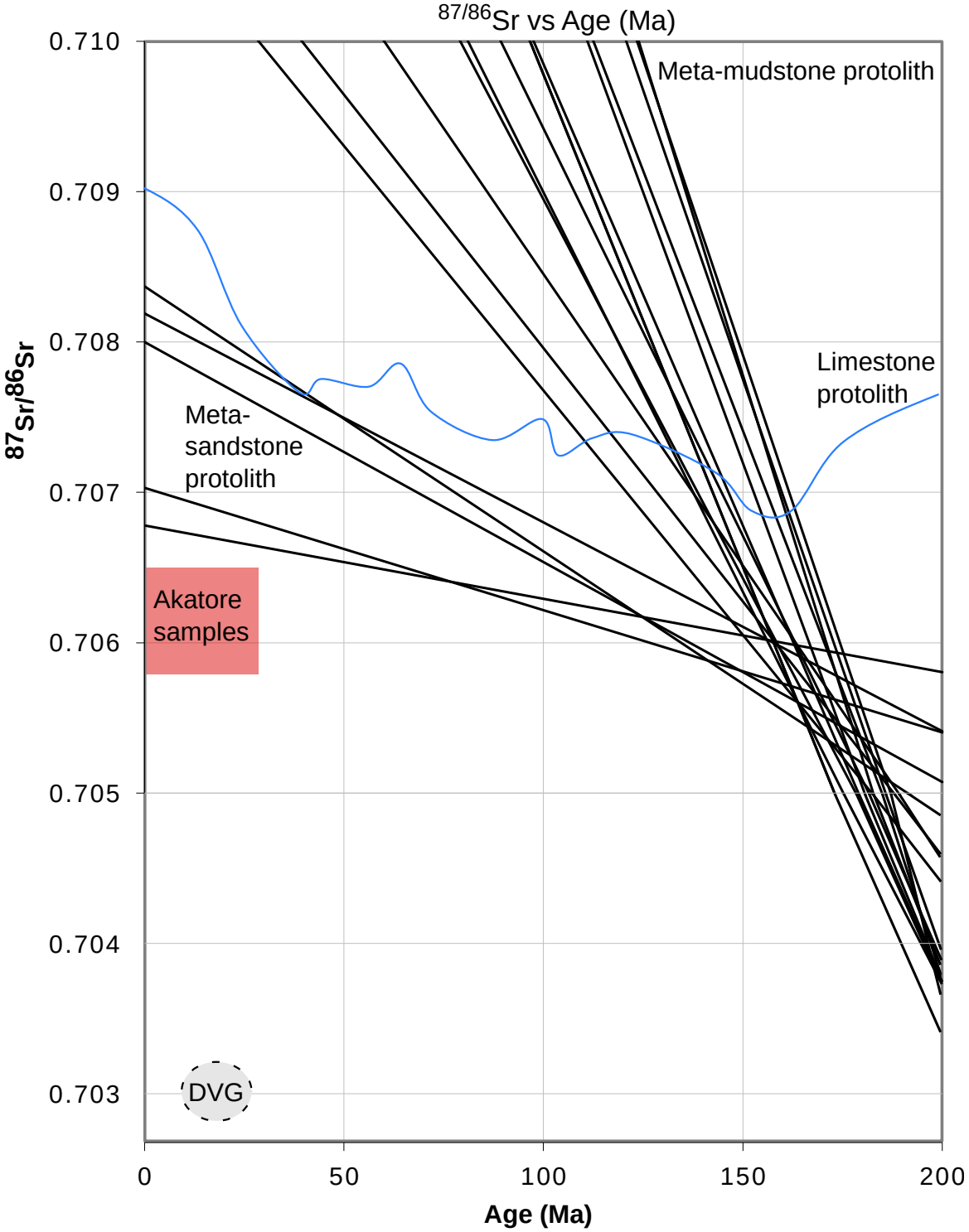

Figure 7.4: Predicted $^{87}Sr/^{86}Sr$ ratio over the past 200 Ma for whole rock Caples Terrane meta-mudstone and meta-sandstone protoliths (Adams and Graham, 1997), marine limestone protolith (McArthur *et al.*, 2001), and Dunedin Volcanic Group (DVG) (Timm *et al.*, 2010) compared to $^{87}Sr/^{86}Sr$ values for Akatore coast (red box).

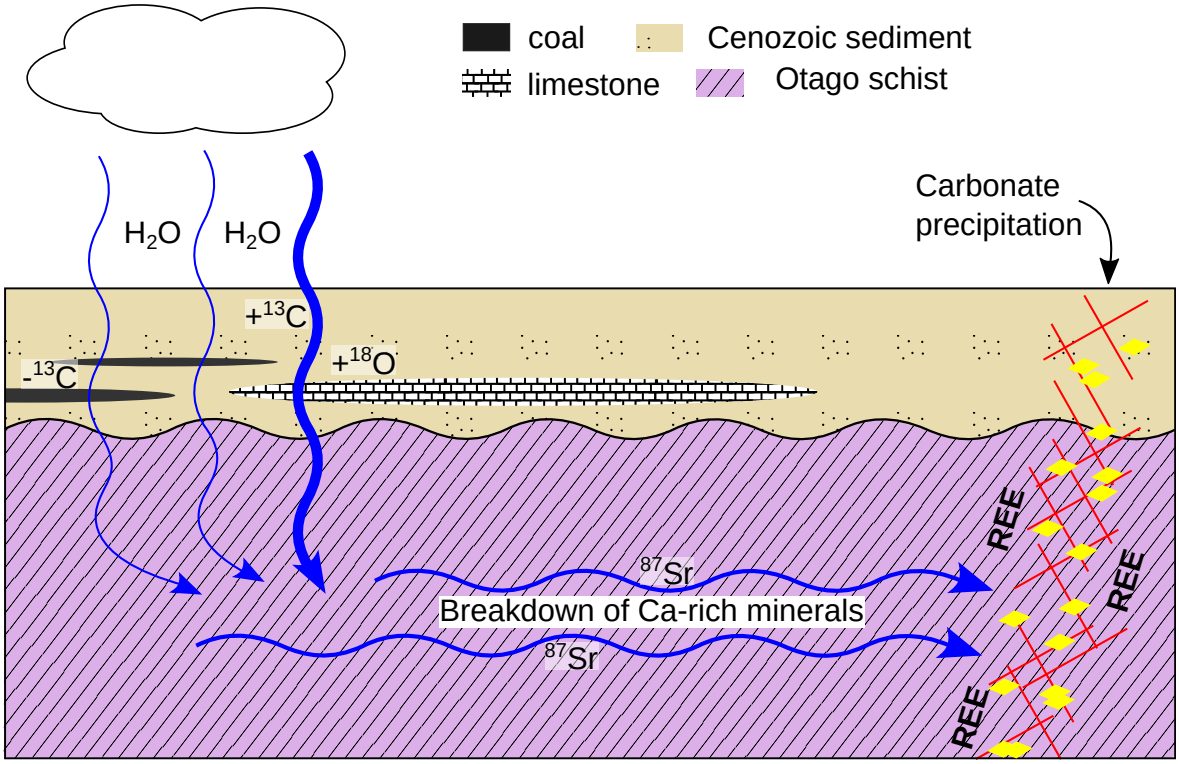

Figure 7.5: Schematic of potential fluid flow path at Akatore coast. Different δ^{13}C compositions are associated with fluids interacting with either limestone or coal horizons. δ^{18}O composition is determined by the volumetrically significant fluid which passes through limestone. ^{87}Sr/^{86}Sr composition relates to the breakdown of Ca-rich minerals in the host schist and REE are scavenged from immediately adjacent to the precipitation zone.

one source to have effectively insignificant proportions of δ^{18}O and ^{87}Sr/^{86}Sr relative to the other source (i.e. the addition of δ^{18}O and ^{87}Sr/^{86}Sr from fluid A does not measurably change the δ^{18}O and ^{87}Sr/^{86}Sr values of fluid B when mixed together).

7.4.3 Potential fluid history at Akatore coast

The Cenozoic sedimentary sequence, with both marine sediments and coal, is still the obvious choice for variable δ^{13}C sources. Downward circulating basinal fluids could pick up a range of δ^{13}C values depending on the extent which they interacted with different sedimentary units (Fig. 7.5). In order to maintain a homogeneous δ^{18}O composition after mixing of these fluids the oxygen proportion would need to be significantly different volumetrically. Given that δ^{18}O values are in a limestone range one option would be for the majority of fluid to sample oxygen from a limestone unit while a small volume

of fluid samples a coal unit. On recombination of these fluids the oxygen component of the coal-sourced fluid is proportionally insignificant compared to the oxygen component of the limestone-sourced fluid so the resultant $\delta^{18}O$ composition remains closer to a pure limestone-sourced $\delta^{18}O$ value. As long as the volume of carbon in each fluid is roughly equivalent the $\delta^{13}C$ composition of the combined fluid will show a 'mixing' signal.

Average $^{87}Sr/^{86}Sr$ values at Akatore coast are $\simeq 0.7062$ (Fig. 7.2). This has been compared to $^{87}Sr/^{86}Sr$ values of regional geologic units (Fig. 7.4) in hopes of identifying a potential fluid source. Present day $^{87}Sr/^{86}Sr$ values for seawater and, by proxy, limestone, is 0.7092 and has not dropped below 0.7070 in the past 150 Ma (Fig. 7.4; McArthur *et al.*, 2001). Age corrected $^{87}Sr/^{86}Sr$ values of whole rock Otago Schist from a meta-sandstone protolith (i.e. the host rock of carbonate features at Akatore coast) have been calculated by Adams and Graham (1997) using Rb-Sr whole rock isochrons but are still greater than $^{87}Sr/^{86}Sr$ values at Akatore coast. By contrast $^{87}Sr/^{86}Sr$ values for the Dunedin Volcanic Group (DVG) are much lower than Akatore samples at $^{87}Sr/^{86}Sr \simeq 0.7030$.

The $^{87}Sr/^{86}Sr$ composition of regional rocks clearly do not correlate well with the carbonates at Akatore coast. Two potential explanations for this are; mixing of $^{87}Sr/^{86}Sr$ values from the DVG and meta-sandstone derived Caples Terrane or that $^{87}Sr/^{86}Sr$ values are derived from the breakdown of specific minerals in the schist. The second option is preferred given the large discrepancy between Akatore and DVG $^{87}Sr/^{86}Sr$ values and presence of Ca-rich, low ^{87}Rb bearing minerals (e.g. carbonate, pumpellyite, and/or epidote) in the host schist but the possibility of a DVG influence cannot be excluded at this time. In this scenario the $^{87}Sr/^{86}Sr$ value is postulated to come from the breakdown of Ca-rich minerals (Fig. 7.5) to calcite (or siderite) and kaolinite in a CO_2-rich fluid (Craw *et al.*, 2009). Crystal lattices which can host Ca are generally incompatible with Rb, which has a much larger ionic radius (White, 2013), and a fluid which breaks down Ca-rich minerals will therefore have a lower $^{87}Sr/^{86}Sr$ ratio than associated whole rock $^{87}Sr/^{86}Sr$ values which will include ^{87}Sr from the radiogenic decay of ^{87}Rb bearing minerals like muscovite (Frei *et al.*, 2004).

REE mobility

Within the current dataset, REE patterns do not offer much without further information. REE patterns of carbonates from Akatore coast generally match REE patterns from Chrystalls Beach Complex lithologies with strong light-REE enrichment, a small

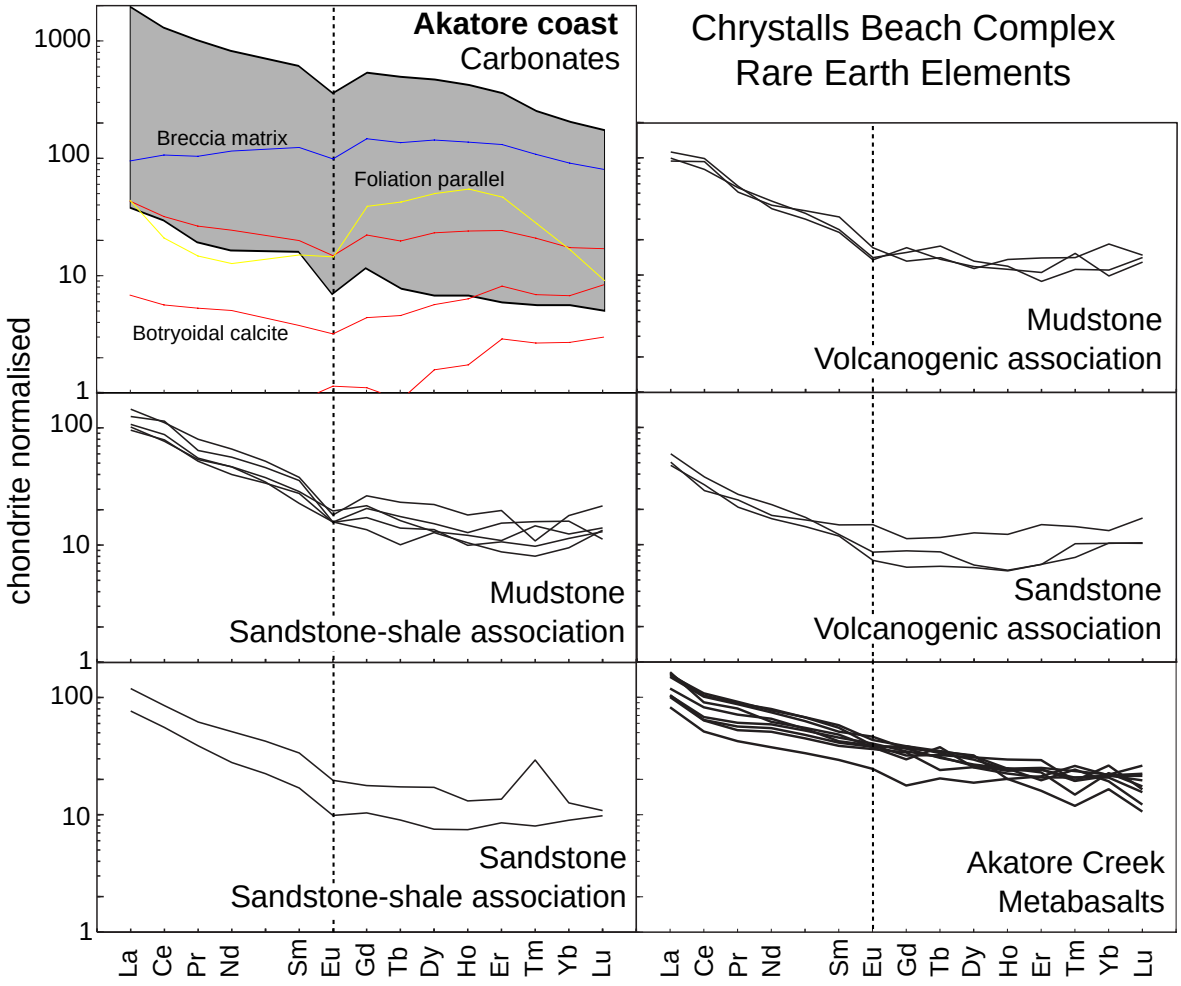

Figure 7.6: Average REE pattern of carbonate features at Akatore coast compared to REE plots for different lithologies present in the Chrystalls Beach Complex from (Fagereng, 2009). Samples AK-24 (red), AK-34-2 (yellow) and AK-23-3 (blue) do not match the average pattern and are shown separately. All plots have been normalised to chondrite values from Sun and McDonough (1989).

negative Eu anomaly, and relatively flat heavy-REE patterns (Fig. 7.6). Carbonates of Akatore coast are concentrated in all REE, up to an order of magnitude, relative to host rocks but REE enrichment is common in Ca-bearing mineral phases (Ingrid, 1998) so this is not notable. Given the similarities in REE patterns from Akatore coast and whole rocks from Chrystalls Beach Complex, local host schist is interpreted to be the source of Akatore coast carbonate REE (Fig. 7.5). That being said, there is very little that can be interpreted in terms of the overall fluid flux responsible for deposition of these carbonates. Given the low mobility of REE a source immediately adjacent to the carbonates is likely in low temperature fluid scenarios. Furthermore the individual solubility of REE in specific fluid phases is controlled by the temperature and pH of the fluid so small variations in REE patterns may be accounted for by variations in carbonate complexation and pH (Byrne and Kim, 1990) rather than reflecting different sources. There is a general pattern of decreasing REE concentrations from quartz-calcite veins to breccia matrix to foliation parallel veins and finally botryoidal calcite. This sequence follows the age of formation (from cross-cutting relationships) from oldest to youngest features and may indicate that REE in host rocks are being progressively leached by each pulse of mineralisation resulting in lower total concentrations of REE in younger features. A larger dataset would be necessary to test this conclusion.

Chapter 8

Summary and Conclusions

The following section summarizes the essential elements and conclusions of each of the chapters included in this thesis, and follows with a short discussion of some wider implications of this work.

8.1 Findings from this study

The aim of this study was to investigate the nature of brittle deformation and fluid flow in clean outcrops of basement schist exposed along the outboard portion of the Otago reverse-fault province (Akatore coast). The main questions addressed throughout the project were:

- What are the sources of fluids in basement rocks of coastal Otago?
- Does fault structure and mineralization depend on fault orientation?
- Do brittle faults in exhumed mid-crustal basement rocks represent ancient seismic slip events?
- How does pre-existing anisotropy (e.g. foliation) influence brittle faulting?
- Could basement fault fabric have any influence on seismicity in Otago?

Lineaments

Analysis of n=6625 lineaments along Akatore coast showed three well-defined preferred orientations; SEbE-NWbW, ENE-WSW, and locally confined N-S trends. Regional

faults, including the nearby active Akatore Fault, are strongly confined to NEbN-SWbS and SEbE-NWbW orientations. Almost no lineaments trending NEbN-SWbS, parallel to the majority of regional faults, were identified.

Fieldwork

Extensive structural fieldwork indicates the SEbE-NWbW lineaments correspond to first-order faults $\leq$ 2 m wide hosting breccias, as well as smaller (generally sinistral) faults that nucleated on continuous, planar, steeply-dipping joints. The latter are associated with paired quartz-calcite veins and small breccia pods developed in dilational jogs between overlapping joints. ENE-WSW lineaments correspond to a second (often dextral) fault set hosting thin, continuous breccia layers formed within intact schist. Both fault sets host shallowly plunging lineations and form a conjugate set.

From cross-cutting relationships relative fault fabric chronology has been established; 1) foliation forms (Mid-Late Jurassic), 2) formation of exhumation joint network (Late Cretaceous), 3) small-displacement conjugate (SE-NW striking sinistral and E-W striking dextral) faults reactivate exhumation joints and are filled by fault related veins and breccias, 4) unconfined botryoidal calcite forms in open voids. The relative age of extensional fractures parallel to foliation cannot be determined by cross-cutting relationships in the field. Stress inversion of lineations from the conjugate fault set indicates the paleostress field during faulting was similar to the modern-day stress field in Canterbury and Otago, characterized by subhorizontal σ_1 trending c. 114°and subvertical σ_2, i.e. a strike-slip regime. Faulting is therefore interpreted to have occurred in the modern-day stress field at $\leq$ 25 Ma.

Microstructures

Mineralogy of Akatore coast host rocks matches descriptions of Chrystalls Beach Complex rocks in the literature. Microstructures are consistent with regional low grade metamorphism and deformation. Microstructures in syntectonic calcite veins and breccia matrix indicates competition for crystal growth but does not show strong evidence for multiple phases of faulting. Extensive weathering can be seen along vein margins where iron carbonates are inferred to have been. Cross-cutting relationships implies that foliation parallel veins were formed after steeply dipping conjugate faults.

Geochemistry

Geochemical analyses of carbonate features show distinctive isotopic trends where $\delta^{13}C$ varies between -16.0 to 2.3 compared to relatively constant $\delta^{18}O$ (18.8 to 25.5) and $\delta^{87}Sr$ (0.705739 to 0.706818) values. This is interpreted as representative of a decoupled carbon system where shallow downward circulating basinal fluids interact with limestone units in the Cenozoic sedimentary overburden and a small proportion interact with coal beds before continuing through the schist and facilitating the breakdown of ^{86}Sr rich, Ca-bearing minerals. REE are assumed to be sourced from immediately adjacent host rock and decreasing REE concentrations with subsequent carbonate precipitation may reflect progressive leaching of adjacent rocks. Fluids are not believed to have interacted with the Dunedin Volcanic Group (emplaced within the same time frame as mineralisation) although this cannot be confidently excluded without further analysis.

8.2 Wider Implications

A number of wider implications can be drawn from the outcomes of this study to answer our original questions.

The fluid recorded by extensive carbonate mineralisation at Akatore coast reflects a complex history which cannot be explained by a single fluid source or mixing model. Instead the isotopic composition has become decoupled allowing overprinting of oxygen and Sr isotopes compared to mixing carbon isotopes by fluids of different volumes interacting with multiple isotope sources at different points through the fluid pathway.

At Akatore coast we see that fault structure and mineralization is strongly dependent on fault orientation with distinctive fault-related veins and breccia characteristics for SEbE-NWbW and ENE-WSW striking features as well as foliation parallel faults. Furthermore similarities in the orientation of fault-related features to foliation and joint orientations demonstrates that pre-existing anisotropy has controlled brittle faulting. Fault-related veins, particularly SEbE-NWbW striking ones, are contained within the exhumation joint network that has been reactivated, breccia lozenges are locally confined to the stepover region between joint tips where dilational jogs have formed, and ENE-WSW joints appear to have facilitated continuous ENE-WSW brecciation during activation of conjugate faults. In addition the slaty cleavage which defines foliation appears to have preferentially failed, opening extensional fracture filled by fibrous calcite veins and calcite-rich breccias.

These brittle faults in exhumed mid-crustal basement rocks at Akatore coast are

interpreted as relatively recent seismic slip events given that they are locally confined to exhumation joints and paleostress analysis ($\sigma_1 = 114°$) indicates formation under the modern day stress configuration ($\sigma_1 = 115°$). Our study has shown that the orientations and kinematics of these widespread basement faults in Otago mimics aspects of the faulting pattern from the 2010-2011 Canterbury Earthquake sequence. A conjugate basement fault fabric, similar to the one documented at Akatore coast, is inferred in Canterbury from observed dextral E-W striking faults (e.g. the Greendale Fault) and the alignment of SE-NW striking aftershocks with sinistral focal planes. Furthermore the first motion observed from the Canterbury mainshock depicted rupture on a NE-SW striking reverse fault such as is observed in Otago regional faults. Thus, there may be a common basement fault fabric developed throughout Otago and Canterbury that plays an important role in controlling earthquake sequences developed within the contemporary stress field.

References

Adams, C. J., Campbell, H. J., and Griffin, W. L. (2007). Provenance comparisons of Permian to Jurassic tectonostratigraphic terranes in New Zealand: perspectives from detrital zircon age patterns. *Geological Magazine*, *144*, 701–729.

Adams, C. J. and Graham, I. J. (1997). Age of metamorphism of Otago Schist in eastern Otago and determination of protoliths from initial strontium isotope characteristics. *New Zealand Journal of Geology and Geophysics*, *40*(3), 275–286.

Adams, C. J. and Robinson, P. (1993). Potassium-argon age studies of metamorphism/uplift/cooling in Haast Schist coastal sections south of Dunedin, Otago, New Zealand. *New Zealand Journal of Geology and Geophysics*, *36*(3), 317–325.

Angelier, J. (1979). Determination of the mean principal directions of stresses for a given fault population. *Tectonophysics*, *56*(34), T17 – T26.

Angelier, J. (1990). Inversion of field data in fault tectonics to obtain the regional stressIII. A new rapid direct inversion method by analytical means. *Geophysical Journal International*, *103*(2), 363–376.

Banner, J. L. (2004). Radiogenic isotopes: systematics and applications to earth surface processes and chemical stratigraphy. *Earth-Science Reviews*, *65*(3-4), 141 – 194.

Beanland, S. and Berryman, K. R. (1989). Style and episodicity of late Quaternary activity on the Pisa-Grandview Fault Zone, Central Otago, New Zealand. *New Zealand Journal of Geology and Geophysics*, *32*(4), 451–461.

Berryman, K. and Beanland, S. (1991). Variation in fault behaviour in different tectonic provinces of New Zealand. *Journal of Structural Geology*, *13*(2), 177 – 189.

Bishop, D. (1974). The Dunedin Earthquake, 9 April, 1974; Part 2: Local effects. Technical report, New Zealand Society for Earthquake Engineering Inc.

Bishop, D. G. (1972). Progressive Metamorphism from Prehnite-Pumpellyite to Greenschist Facies in the Dansey Pass Area, Otago, New Zealand. *Geological Society of America Bulletin*, *83*(11), 3177–3198.

Bishop, D. G. (1994). *Institute of Geological & Nuclear Sciences Geological Map 9*, Chapter Geology of the Milton area. Lower Hutt, New Zealand. Institute of Geological & Nuclear Sciences Ltd.

Bott, M. H. P. (1959). The Mechanics of Oblique Slip Faulting. *Geological Magazine*, *96*, 109–117.

Butler, R., Bond, C., Shipton, Z., Jones, R., and Casey, M. (2008). Fabric anisotropy controls faulting in the continental crust. *Journal of the Geological Society*, *165*(2), 449–452.

Byrne, R. H. and Kim, K. (1990). Rare earth element scavenging in seawater. *Geochimica et Cosmochimica Acta*, *54*(10), 2645 – 2656.

Coombs, D. S., Adams, C. J., Roser, B. P., and Reay, A. (2008). Geochronology and geochemistry of the Dunedin Volcanic Group, eastern Otago, New Zealand. *New Zealand Journal of Geology and Geophysics*, *51*(3), 195–218.

Coombs, D. S., Cas, R., Kawachi, Y., Landis, C., McDonough, W., and Reay, A. (1986). Cenozoic volcanism in north, east and central Otago. *Royal Society of New Zealand Bulletin*, *23*, 278–312.

Cortes, A. L., Soriano, M. A., Maestro, A., and Casas, A. M. (2003). The role of tectonic inheritance in the development of recent fracture systems, Duero Basin, Spain. *International Journal of Remote Sensing*, *24*(22), 4325–4345.

Craw, D., Coombs, D. S., and Kawachi (1982). Interlayered biotite-kaolin and other altered biotites, and their relevance to the biotite isograd in Eastern Otago, New Zealand. *Mineralogical Magazine*, *45*(337), 79–85.

Craw, D. and Norris, R. (1991). Metamorphogenic Au-W veins and regional tectonics: Mineralisation throughout the uplift history of the Haast Schist, New Zealand. *New Zealand Journal of Geology and Geophysics*, *34*(3), 373–383.

Craw, D., Upton, P., and Mackenzie, D. J. (2009). Hydrothermal alteration styles in ancient and modern orogenic gold deposits, New Zealand. *New Zealand Journal of Geology and Geophysics*, *52*(1), 11–26.

Davis, J. C. and Sampson, R. J. (2002). *Statistics and data analysis in geology*, Volume 3. Wiley New York.

Delvaux, D. and Sperner, B. (2003). New aspects of tectonic stress inversion with reference to the TENSOR program. *Geological Society, London, Special Publications*, *212*(1), 75–100.

Dorn, C., Green, A. G., Jongens, R., Carpentier, S., Kaiser, A. E., Campbell, F., Horstmeyer, H., Campbell, J., Finnemore, M., and Pettinga, J. (2010). High-resolution seismic images of potentially seismogenic structures beneath the northwest Canterbury Plains, New Zealand. *Journal of Geophysical Research: Solid Earth*, *115*(B11).

Fagereng, A. (2009). *Subduction-related Fault Processes: Ancient and Active*. Ph. D. thesis, University of Otago, Dunedin, New Zealand.

Fagereng, A. (2011a). Fractal vein distributions within a fault-fracture mesh in an exhumed accretionary mlange, Chrystalls Beach Complex, New Zealand. *Journal of Structural Geology*, *33*(5), 918 – 927.

Fagereng, A. (2011b). Frequency-size distribution of competent lenses in a block-in-matrix mlange: Imposed length scales of brittle deformation? *Journal of Geophysical Research: Solid Earth*, *116*(B5).

Fagereng, A. and Cooper, A. (2010a). The metamorphic history of rocks buried, accreted and exhumed in an accretionary prism: an example from the Otago Schist, New Zealand. *Journal of Metamorphic Geology*, *28*(9), 935–954.

Fagereng, A. and Cooper, A. (2010b). Petrology of metabasalts from the Chrystalls Beach accretionary mlange - implications for tectonic setting and terrane origin. *New Zealand Journal of Geology and Geophysics*, *53*(1), 57–70.

Faulkner, D. and Armitage, P. (2013). The effect of tectonic environment on permeability development around faults and in the brittle crust. *Earth and Planetary Science Letters*, *375*(0), 71 – 77.

Frei, D., Liebscher, A., Franz, G., and Dulski, P. (2004). Trace Element Geochemistry of Epidote Minerals. *Reviews in Mineralogy and Geochemistry*, *56*(1), 553–605.

Gabrielsen, R. H., Braathen, A., Dehls, J., and Roberts, D. (2002). Tectonic lineaments of Norway. *Norsk Geologisk Tidsskrift*, *82*(3), 153–174.

Ghisetti, F. C. and Sibson, R. H. (2012). Compressional reactivation of E-W inherited normal faults in the area of the 2010 – 2011 Canterbury earthquake sequence. *New Zealand Journal of Geology and Geophysics*, *55*(3), 177–184.

Ghisetti, F. C. and Vezzani, L. (2002). Normal faulting, transcrustal permeability and seismogenesis in the Apennines (Italy). *Tectonophysics*, *348*(1-3), 155 – 168. Tectonic Processes and the Flow of Mineralising Fluids.

Glassey, P., Barrell, D., Forsyth, J., and Macleod, R. (2003). The geology of Dunedin, New Zealand, and the management of geological hazards. *Quaternary International*, *103*(1), 23 – 40. Urban and Quaternary Geology, New Zealand and Eastern Australia.

Gledhill, K., Ristau, J., Reyners, M., Fry, B., and Holden, C. (2011). The Darfield (Canterbury, New Zealand) Mw 7.1 Earthquake of September 2010: A Preliminary Seismological Report. *Seismological Research Letters*, *82*(3), 378–386.

GNS (2012). QMAP.

Golyshev, S., Padalko, N., and Pechenkin, S. (1981). Fractionation of stable isotopes of carbon and oxygen in carbonate systems. *Geokhimiya*, (10), 1427–1441.

Gracia, E., Danobeitia, J., Verges, J., Bartolome, R., and Cordoba, D. (2003). Crustal architecture and tectonic evolution of the Gulf of Cadiz (SW Iberian margin) at the convergence of the Eurasian and African plates. *Tectonics*, *22*(4).

Gray, D. and Foster, D. (2004). 40Ar/39Ar thermochronologic constraints on deformation, metamorphism and cooling/exhumation of a Mesozoic accretionary wedge, Otago Schist, New Zealand. *Tectonophysics*, *385*(1-4), 181 – 210.

Hada, S., Yoshikura, S., Landis, C. A., and Coombs, D. S. (2006). Melange fabric of the Chrystalls Beach Complex, southeast Otago, New Zealand. *The Journal of the Geological Society of Japan*, *112*(6), XI–XII.

Hale, R. V. (2014). Method note for $\delta^{13}C$ and $\delta^{18}O$ measurements of carbonates.

Higgins, R. and Harris, L. (1997). The effect of cover composition on extensional faulting above re-activated basement faults: results from analogue modelling. *Journal of Structural Geology*, *19*(1), 89 – 98.

Hilgers, C. and Urai, J. L. (2002). Microstructural observations on natural syntectonic fibrous veins: implications for the growth process. *Tectonophysics*, *352*(34), 257 – 274.

Hirth, G. and Tullis, J. (1992). Dislocation creep regimes in quartz aggregates. *Journal of Structural Geology*, *14*(2), 145 – 159.

Hobbs, W. H. (1904). Lineaments of the Atlantic border region. *Geological Society of America Bulletin*, *15*, 483–506.

Hoefs, J. (2009). *Stable Isotope Geochemistry*. Springer.

Hoernle, K., White, J., van den Bogaard, P., Hauff, F., Coombs, D., Werner, R., Timm, C., Garbe-Schonberg, D., Reay, A., and Cooper, A. (2006). Cenozoic intraplate volcanism on New Zealand: Upwelling induced by lithospheric removal. *Earth and Planetary Science Letters*, *248*(12), 350 – 367.

Hudson, J. D. (1977). Stable isotopes and limestone lithification. *Journal of the Geological Society*, *133*(6), 637–660.

Hung, L. Q., Batelaan, O., and De Smedt, F. (2005). Lineament extraction and analysis, comparison of LANDSAT ETM and ASTER imagery. Case study: Suoimuoi tropical karst catchment, Vietnam. *Proc. SPIE*, *5983*, 59830T–59830T–12.

Ingrid, H.-K. (1998). Rare Earth Elements in Svitic Carbonatites and their Mineral Phases. *Journal of Petrology*, *39*(11-12), 2105–2121.

JISCM@IL (2014). Geo-Tectonics Mailing List.

Kamb, W. B. (1959). Ice petrofabric observations from Blue Glacier, Washington, in relation to theory and experiment. *Journal of Geophysical Research*, *64*(11), 1891–1909.

Lacombe, O., Jolivet, L., Le Pourhiet, L., Lecomte, E., and Mehl, C. (2013). Initiation, geometry and mechanics of brittle faulting in exhuming metamorphic rocks: insights from the northern Cycladic islands (Aegean, Greece). *Bulletin de la Societe Geologique de France*, *184*(4-5), 383–403.

Li, G., Essene, E. J., Peacor, D. R., and Coombs, D. S. (2000). Reactions leading to the formation and breakdown of stilpnomelane in the Otago Schist, New Zealand. *Journal of Metamorphic Geology*, *18*(4), 393–407.

Litchfield, N. J. (2001). The Titri Fault System: Quaternary-active faults near the leading edge of the Otago reverse fault province. *New Zealand Journal of Geology and Geophysics*, *44*(4), 517–534.

Litchfield, N. J. and Norris, R. J. (2000). Holocene motion on the Akatore Fault, south Otago coast, New Zealand. *New Zealand Journal of Geology and Geophysics*, *43*(3), 405–418.

MacKinnon, T. C. (1983). Origin of the Torlesse terrane and coeval rocks, South Island, New Zealand. *Geological Society of America Bulletin*, *94*(8), 967–985.

McArthur, J. M., Howarth, R. J., and Bailey, T. R. (2001). Strontium Isotope Stratigraphy: LOWESS Version 3: Best Fit to the Marine Sr-Isotope Curve for 0509 Ma and Accompanying Look-up Table for Deriving Numerical Age. *The Journal of Geology*, *109*(2), pp. 155–170.

McMillan, S. G. and Wilson, G. J. (1997). Allostratigraphy of coastal south and east Otago: A stratigraphic framework for interpretation of the Great South Basin, New Zealand. *New Zealand Journal of Geology and Geophysics*, *40*(1), 91–107.

Mortimer, N. (1993). Jurassic tectonic history of the Otago Schist, New Zealand. *Tectonics*, *12*(1), 237–244.

Mortimer, N. (2000). Metamorphic discontinuities in orogenic belts: example of the garnet-biotite-albite zone in the Otago Schist, New Zealand. *International Journal of Earth Sciences*, *89*(2), 295–306.

Mortimer, N. (2003). A provisional structural thickness map of the Otago Schist, New Zealand. *American Journal of Science*, *303*(7), 603–621.

Mortimer, N. (2004). New Zealand's Geological Foundations. *Gondwana Research*, *7*(1), 261 – 272.

Mortimer, N., Davey, F. J., Melhuish, A., Yu, J., and Godfrey, N. J. (2002). Geological interpretation of a deep seismic reflection profile across the Eastern Province and Median Batholith, New Zealand: Crustal architecture of an extended Phanerozoic convergent orogen. *New Zealand Journal of Geology and Geophysics*, *45*(3), 349–363.

Nelson, C. S., Harris, G. J., and Young, H. R. (1988). Burial-dominated cementation in non-tropical carbonates of the Oligocene Te Kuiti Group, New Zealand. *Sedimentary Geology*, *60*(14), 233 – 250. Non-tropical shelf carbonates-modern and ancient.

Nelson, C. S. and Smith, A. M. (1996). Stable oxygen and carbon isotope compositional fields for skeletal and diagenetic components in New Zealand Cenozoic nontropical carbonate sediments and limestones: A synthesis and review. *New Zealand Journal of Geology and Geophysics*, *39*(1), 93–107.

Nelson, K. D. (1982). A suggestion for the origin of mesoscopic fabric in accretionary melange, based on features observed in the Chrystalls Beach Complex, South Island, New Zealand. *Geological Society of America Bulletin*, *93*(7), 625–634.

Nishimura, Y., Coombs, D. S., Landis, C. A., and Itaya, T. (2000). Continuous metamorphic gradient documented by graphitization and K-Ar age, southeast Otago, New Zealand. *American Mineralogist*, *85*(11-12), 1625–1636.

Norris, R., Carter, R. M., and Turnbull, I. M. (1978). Cainozoic sedimentation in basins adjacent to a major continental transform boundary in southern New Zealand. *Journal of the Geological Society*, *135*(2), 191–205.

Norris, R., Koons, P., and Cooper, A. (1990). The obliquely-convergent plate boundary in the South Island of New Zealand: implications for ancient collision zones. *Journal of Structural Geology*, *12*(5-6), 715 – 725. Australasian tectonics.

Norris, R. and Turnbull, I. (1993). Cenozoic basins adjacent to an evolving transform plate boundary, southwest New Zealand. *South Pacific Sedimentary Basins. Sedimentary Basins of the World. Amsterdam, Elsevier Science Publishers BV*, 251–270.

Norris, R. and Turnbull, M. (1996). The Akatore Fault and Haast Schists, Otago coast. In *Geological society of New Zealand 1996 annual conference field trip guides*. Geological society of New Zealand.

NZPAM (1978). Takapu-1A composite well log.

NZPAM (2013). Great South-Canterbury Province. Technical report, New Zealand Petroleum and Minerals.

O'Leary, D., Friedman, J., and Pohn, H. (1976). Lineament, linear, lineation; some proposed new standards for old terms. *Geological Society of America Bulletin*, *87*(10), 1463–1469.

Pewsey, A., Neuhauser, M., and Ruxton, G. (2013). *Circular Statistics in R*. EBL-Schweitzer. OUP Oxford.

Pitcairn, I. K., Teagle, D. A. H., Craw, D., Olivo, G. R., Kerrich, R., and Brewer, T. S. (2006). Sources of Metals and Fluids in Orogenic Gold Deposits: Insights from the Otago and Alpine Schists, New Zealand. *Economic Geology*, *101*(8), 1525–1546.

Pollard, D., Saltzer, S., and Rubin, A. M. (1993). Stress inversion methods: are they based on faulty assumptions? *Journal of Structural Geology*, *15*(8), 1045 – 1054.

Price, R. C., Cooper, A. F., Woodhead, J. D., and Cartwright, I. (2003). Phonolitic Diatremes within the Dunedin Volcano, South Island, New Zealand. *Journal of Petrology*, *44*(11), 2053–2080.

Reyners, M., Ingham, C. E., and Ferris, B. G. (1983). Microseismicity of the upper Clutha valley, South Island, New Zealand. *New Zealand Journal of Geology and Geophysics*, *26*(1), 1–6.

Robinson, P. (1958). The structural and metamorphic geology of the Brighton-Taieri Mouth area, east Otago, New Zealand. Master's thesis, University of Otago. Unpublished M.Sc. thesis, lodged in the Library.

Rye, R. O. and Ohmoto, H. (1974). Sulfur and Carbon Isotopes and Ore Genesis: A Review. *Economic Geology*, *69*(6), 826–842.

Saltzer, S. D. and Pollard, D. D. (1992). Distinct element modeling of structures formed in sedimentary overburden by extensional reactivation of basement normal faults. *Tectonics*, *11*(1), 165–174.

Shaner, J. (2013). Smartphones, Tablets and GPS Accuracy.

Sibson, R. H. (1987). Earthquake rupturing as a mineralizing agent in hydrothermal systems. *Geology*, *15*(8), 701–704.

Sibson, R. H. (1989). Earthquake faulting as a structural process. *Journal of Structural Geology*, *11*(1-2), 1 – 14.

Sibson, R. H. (1992). Implications of fault-valve behaviour for rupture nucleation and recurrence. *Tectonophysics*, *211*(1-4), 283 – 293.

Sibson, R. H. (1994). Crustal stress, faulting and fluid flow. *Geological Society, London, Special Publications*, *78*(1), 69–84.

Sibson, R. H. (1996). Structural permeability of fluid-driven fault-fracture meshes. *Journal of Structural Geology*, *18*(8), 1031 – 1042.

Sibson, R. H., Ghisetti, F. C., and Crookbain, R. A. (2012). Andersonian wrench faulting in a regional stress field during the 20102011 Canterbury, New Zealand, earthquake sequence. *Geological Society, London, Special Publications*, *367*(1), 7–18.

Sibson, R. H., Ghisetti, F. C., and Ristau, J. (2011). Stress Control of an Evolving Strike-Slip Fault System during the 2010-2011 Canterbury, New Zealand, Earthquake Sequence. *Seismological Research Letters*, *82*(6), 824–832.

Stipp, M., Stnitz, H., Heilbronner, R., and Schmid, S. M. (2002). The eastern Tonale fault zone: a 'natural laboratory' for crystal plastic deformation of quartz over a temperature range from 250 to 700°C. *Journal of Structural Geology*, *24*(12), 1861 – 1884.

Sun, S. and McDonough, W. F. (1989). Chemical and isotopic systematics of oceanic basalts: implications for mantle composition and processes. *Geological Society, London, Special Publications*, *42*(1), 313–345.

Suppe, J. (2007). Absolute fault and crustal strength from wedge tapers. *Geology*, *35*(12), 1127–1130.

Suzen, M. L. and Toprak, V. (1998). Filtering of satellite images in geological lineament analyses: An application to a fault zone in Central Turkey. *International Journal of Remote Sensing*, *19*(6), 1101–1114.

Templeton, A., Chamberlain, C., Koons, P., and Craw, D. (1998). Stable isotopic evidence for mixing between metamorphic fluids and surface-derived waters during recent uplift of the Southern Alps, New Zealand. *Earth and Planetary Science Letters*, *154*(14), 73 – 92.

Timm, C., Hoernle, K., Werner, R., Hauff, F., van den Bogaard, P., White, J., Mortimer, N., and Garbe-Schonberg, D. (2010). Temporal and geochemical evolution of the Cenozoic intraplate volcanism of Zealandia. *Earth-Science Reviews*, *98*(12), 38 – 64.

Townend, J. and Zoback, M. D. (2000). How faulting keeps the crust strong. *Geology*, *28*(5), 399–402.

Turnbull, I. M., Mortimer, N., and Craw, D. (2001). Textural zones in the Haast Schist - a reappraisal. *New Zealand Journal of Geology and Geophysics*, *44*(1), 171–183.

Upton, P., Caldwell, T. G., Chamberlain, C. P., Craw, D., James, Z., Jiracek, G., Koons, P., and Wannamaker, P. (2000). Fluids in a backthrust regime (Southern Alps, New Zealand). *Journal of Geochemical Exploration*, *69-70*, 517 – 521.

Valley, M. (2014). FieldMove.

Valoroso, L., Chiaraluce, L., and Collettini, C. (2014). Earthquakes and fault zone structure. *Geology*, *42*(4), 343–346.

Weinberger, R., Eyal, Y., and Mortimer, N. (2010). Formation of systematic joints in metamorphic rocks due to release of residual elastic strain energy, Otago Schist, New Zealand. *Journal of Structural Geology*, *32*(3), 288 – 305.

White, W. (2013). *Geochemistry*. Wiley.

Woodcock, N. H. and Mort, K. (2008). Classification of fault breccias and related fault rocks. *Geological Magazine*, *145*(3), 435–440.

Yin, Z. and Ranalli, G. (1992). Critical stress difference, fault orientation and slip direction in anisotropic rocks under non-Andersonian stress systems. *Journal of Structural Geology*, *14*(2), 237 – 244.

Appendix A

R Code

```
### Code for reading in linear directional mean calculated CSV files
    and plotting as a rose diagram using Circular package###

#########################################################################
### Setup

setwd("working directory folder path here")
library(circular)


#########################################################################
### Functions for creating rose diagrams

drawroselinear <- function(data, title, bins, ...){
   plot <- rose.diag(data, stack=TRUE, main = title, cex = 1, axes =
           FALSE, col=3, prop = 10, bins=bins, upper=TRUE, radii.scale
           = "linear", ...)
}

plotroselinear <- function(data, title, bins, akatore, ...){
    drawroselinear(data, title, bins, ...)
    axis.circular(at=circular(seq(0,2*pi,by=pi/4)), labels=c("E","NE",
           "N","NW","W","SW","S","SE","E"), units="degrees", template=
           "geographic", tcl.text = -0.1, tick=FALSE)
```

```
    ##add circles to plot
    symbols(0, 0, circle = 0.2, inches = FALSE, add = TRUE)
    symbols(0, 0, circle = 0.6, inches = FALSE, add = TRUE)
}


#########################################################################
### Reading data into R

LinTable <- read.csv("lineament_orientation.csv")
akatore_flt <- read.csv("Akatore_DirectionalMean.csv")
otago_flts <- read.csv("Otago_Faults_orientation.csv")


#########################################################################
### Assigning variables

### Creating dataframe of lineaments from original csv
sorted <- LinTable[order(LinTable$Group),]  ##Sort ascending by group

##Create a dataframe of circular type with only columns of interest
dfLin <- data.frame(circular(data.frame(sorted$Group, sorted$CompassA,
    sorted$AveLen, sorted$Dist_group, sorted$Nat_group), type="angles",
    units="degrees", template="geographic"))

##Rename columns
colnames(dfLin) <- c("group", "compassA", "aveLen", "distGroup",
    "natGroup")


###Average of regional fault angles

##compass angle measured clockwise from N as type circular
akatoreOrient <- circular(akatore_flt[,2], type="angles", units=
    "degrees", template="geographic")
```

```
##compass angle measured clockwise from N as type circular
otagoOrient <- data.frame(circular(otago_flts[,2], type="angles",
    units="degrees", template="geographic"))

##Mean NNE and SSW orientation
otagoMeanOrient <- c(mean(otagoOrient[otagoOrient <= 90]),
    mean(otagoOrient[otagoOrient >= 90]))



#########################################################################
### Plot parameters

par('usr') ##user coordinates and plot dimensions

### Saving orginal settings (1 plot displayed)
opar <- par()

### Create new plot
plot.new()

### Return to original dimensions
par(opar)

#########################################################################
### Creating rose diagram plots

### Choose bin size
bins = 36

###############################################
### Otago regional data
plotrose(otagoOrient, 'Nearby lineaments in Otago region', bins,
    akatoreOrient, otagoMeanOrient, shrink=1.2)
```

```
##############################################
### All data
plotrose(dfLin$compassA, 'Lineaments along Akatore coast', bins,
    akatoreOrient, otagoMeanOrient, shrink=1.2)

### All lineaments >30m
plotrose(dfLin$compassA[dfLin$aveLen>=30], 'Lineaments along Akatore
    coast >30m in length', bins, akatoreOrient, otagoMeanOrient,
    shrink=1.25)



##############################################
### Group or natural break to plot
group=21

##############################################
### Lineaments by distGroup (1-10)
plotrose(dfLin$compassA[dfLin$distGroup>=group], paste(c('Lineaments
    along Akatore coast in group', group), sep=""), bins,
    akatoreOrient, otagoMeanOrient, shrink=1.25)

### Lineaments >30m by distGroup (1-10)
plotrose(dfLin$compassA[dfLin$aveLen>=30 & dfLin$distGroup>=group],
    paste(c('Lineaments along Akatore coast >30m in length in group',
    group), sep=""), bins, akatoreOrient, otagoMeanOrient, shrink=1.25)



##############################################
### Lineaments by natGroup (1-21)
plotrose(dfLin$compassA[dfLin$natGroup>=group], paste(c('Lineaments
    along Akatore coast in natural break', group), sep=""), bins,
    akatoreOrient, otagoMeanOrient, shrink=1.25)

### Lineaments >30m by natGroup (1-21)
plotrose(dfLin$compassA[dfLin$aveLen>=30 & dfLin$natGroup>=group],
```

```
    paste(c('Lineaments along Akatore coast >30m in length in natural
    break', group), sep=""), bins, akatoreOrient, otagoMeanOrient,
    shrink=1.25)


#########################################################################
###Save last plot

png("filename.png")

png("images/otago.png")

png(paste(c('filename', group, '.png'), collapse=""))

#run plot
dev.off()
```

Appendix B

Dominant orientations of lineaments

B.1 Regional lineament orientations

Table B.1: Primary and secondary dominant orientations seen in Otago region faults and lineaments at Akatore coast.

Rose Diagrams	Primary Orientations	Secondary Orientations
Otago region	20-50	110-140
Akatore coast	120-140	0-10 60-70 90-120 140-150

B.2 Akatore coast lineament (length >30 m) orientations

Table B.2: Primary and secondary dominant orientations of lineaments (length >30 m) at Akatore coast.

Rose Diagrams	Primary Orientations	Secondary Orientations
Akatore coast 30+	60-80 120-140	0-10 90-100

B.3 Lineament orientations by assigned group

Table B.3: Primary, secondary, and tertiary orientations of lineaments at Akatore coast divided into groups (x 10) of equal length.

Rose Diagrams	Primary Orientations	Secondary Orientations	Tertiary Orientations
Dist_group 1	120-140	0-10 60-70 90-120 140-150	
Dist_group 2	120-140	0-10 60-70 90-120 140-150	
Dist_group 3	120-140	0-10 60-70 90-120 140-150	
Dist_group 4	120-140	60-70 90-100 110-120 140-150	0-10 100-110
Dist_group 5	120-140	60-70 90-100 110-120 140-150	0-10 100-110
Dist_group 6	120-140	60-70 90-100 110-120 140-150	0-10
Dist_group 7	120-140	0-10 60-70 140-150 170-180	110-120 150-160

Dist_group 8	130-140	0-10 110-130 140-160 170-180	60-70
Dist_group 9	130-160	60-70 110-130	0-10 160-180
Dist_group 10	140-150	0-10 50-70 90-100 150-160 170-180	130-140 160-170

B.4 Lineament orientations (length >30 m) by assigned group

Table B.4: Primary, secondary, and tertiary orientations of lineaments (length >30 m) at Akatore coast divided into groups (x 10) of equal length.

Rose Diagrams	Primary Orientations	Secondary Orientations	Tertiary Orientations
Group 1 30+	60-80 120-140	0-10 90-100	
Group 2 30+	60-80 120-140	0-10 90-100	
Group 3 30+	60-80 120-140	0-10 90-120	50-60
Group 4 30+	60-80 120-140	0-10 90-100 110-120	50-60 100-110
Group 5 30+	60-70 120-130	0-10 70-80 90-100 130-140	50-60

Group 6 30+	60-70 120-140	0-10 70-80 90-100	
Group 7 30+	60-70 130-140	120-130	0-10 90-100 170-180
Group 8 30+	130-140	60-70	90-100 120-130 150-160 170-180
Group 9 30+	60-70 130-140	150-160	110-130 170-180
Group 10 30+	50-70	0-10 90-100 130-160	170-180

B.5 Lineament orientations by natural breaks

Table B.5: Primary, secondary, and tertiary orientations of lineaments at Akatore coast divided by natural breaks (x 21) in the coastal platform.

Rose Diagrams	Primary Orientations	Secondary Orientations	Tertiary Orientations
Natural break 1	120-140	0-10 60-70 90-120 140-150	
Natural break 2	120-140	0-10 60-70 90-120 140-150	
Natural break 3	120-140	60-70 90-120 140-150	0-10

Natural break 4	120-140	60-70 90-120 140-150	0-10
Natural break 5	120-140	60-70 90-120 140-150	0-10
Natural break 6	120-140	60-70 90-120 140-150	0-10
Natural break 7	120-140	60-70 90-120 140-150	0-10
Natural break 8	120-140	60-70 90-120 140-150	0-10
Natural break 9	120-140	60-70 90-100 110-120 140-150	0-10 100-110
Natural break 10	120-140	60-70 90-100 110-120 140-150	0-10 100-110
Natural break 11	120-140	60-70 90-100 110-120 140-150	0-10 100-110
Natural break 12	120-140	0-10 60-70 90-100 110-120 140-150	170-180

Natural break 13	60-70 120-140	0-10 90-100 110-120 140-150	170-180
Natural break 14	60-70 120-140	0-10 110-120 140-150 170-180	150-160
Natural break 15	130-140	0-10 110-130 140-160 170-180	60-70
Natural break 16	130-140	0-10 60-70 110-130 140-160 170-180	
Natural break 17	140-150	0-10 60-70 110-120 130-140 150-160 170-180	160-170
Natural break 18	140-150	0-10 60-70	90-100 110-120 130-140 150-170
Natural break 19	140-150	0-10 50-70	90-100 130-140 150-180
Natural break 20	0-10	50-70	90-100 130-150 170-180

Natural break 21	0-10 50-60		90-100 110-120 130-140

B.6 Lineament orientations (length >30 m) by natural breaks

Table B.6: Primary, secondary, and tertiary orientations of lineaments (length >30 m) at Akatore coast divided by natural breaks (x 21) in the coastal platform.

Rose Diagrams	Primary Orientations	Secondary Orientations	Tertiary Orientations
Natural break 1 30+	60-80 120-130	0-10 90-100 130-140	
Natural break 2 30+	60-70 120-130	0-10 70-80 90-100 130-140	100-120
Natural break 3 30+	60-70 120-130	0-10 70-80 130-140	50-60 90-120
Natural break 4 30+	60-70 120-130	70-80 130-140	0-10 50-60 90-120
Natural break 5 30+	60-70 120-130	70-80 130-140	0-10 50-60 90-120
Natural break 6 30+	60-70 120-130	70-80 130-140	0-10 50-60 90-120
Natural break 7 30+	60-70 120-130	70-80 130-140	0-10 50-60 90-120

Natural break 8 30+	60-70 120-130	0-10 70-80 90-100 130-140	50-60 110-120
Natural break 9 30+	60-70 120-130	0-10 70-80 90-100 130-140	50-60
Natural break 10 30+	60-70 120-130	0-10 70-80 90-100 130-140	50-60
Natural break 11 30+	60-70 120-130	0-10 70-80 90-100 130-140	50-60
Natural break 12	60-70 120-140	0-10 90-100	70-80
Natural break 13 30+	60-70	0-10 90-100 120-140	70-80
Natural break 14 30+	60-70 130-140	0-10 90-100 120-130 170-180	110-120
Natural break 15 30+	130-140	60-70 90-100 120-130	0-10 110-120 170-180
Natural break 16 30+	130-140	60-70 90-100 120-130 150-160 170-180	110-120 140-150

Natural break 17 30+	60-70 130-140	0-10 50-60 110-120 140-160	90-100 170-180
Natural break 18 30+	60-70	130-140	0-10 50-60 90-100 110-120 140-160
Natural break 19 30+	60-70	50-60 140-150	0-10 90-100 130-140 150-160
Natural break 20 30+	50-70	0-10 90-100 130-140 170-180	160-170
Natural break 21 30+	0-10 50-60	60-70 90-100 130-140 170-180	

Appendix C

Digital Pilot Study

There are a variety of different devices and software available for digital fieldwork, ranging from professional tools that have been developed for geoscientists, to open-source apps for everyday devices such as smartphones and tablets. Each device and software combination offers individual benefits, disadvantages, and capabilities that need to be considered before commencing fieldwork.
Devices available for digital mapping at the University of Otago included; a Toshiba tablet, a Samsung tablet, a Nomad GPS unit, and a GeoExplorer (GeoXT) GPS unit. Available software included; ArcPad (a mobile version of ArcGIS) and FieldMove (made by Midland Valley) on the Toshiba tablet, Geopaparazzi and Collector (an online version of ArcGIS) on the Samsung tablet, ArcPad on the Nomad unit, and TerraSync on the GeoXT unit. Additionally, open source compass-clinometer apps including the popular FieldMove Clino are available for smartphones (assessed using an iPhone 4 in this study) and iPads.
The pilot study was primarily conducted on coastal platform segments near Akatore Creek where key fault rock assemblages were noted in earlier preliminary fieldwork.

C.1 Methodology for pilot study

Pre-fieldwork preparation of basemaps

Local aerial photograph basemaps were clipped from aerial photography of the entire field region in ArcGIS and exported as either TIFF or JPEG2000 files. A clipped shapefile of lineaments overlying local regions was also generated. Empty shapefiles for joints, foliation, lineations, faults, general points, and general line features were created and appropriate symbols assigned. All files were then exported into ArcPad accessible

files. A data dictionary for Terrasync was created with features matching the empty shapefiles for ArcPad. The clipped basemap and lineament shapefile were uploaded into Terrasync, FieldMove, as well as converted to *mbtiles* and *SQLite* databases respectively for Geopaparazzi. Significant time was spent trying to upload the aerial photography basemap and lineament files to ArcGIS online for use by Collector but ultimately only the lineament shapefile could be successfully uploaded.

Preliminary Fieldwork

The Nomad GPS unit running ArcPad was tested at the beginning of the year at Brighton. Structural point measurements of joints, foliation, lineations, and faults were made and a polyline trace was also taken. Measurements were located using both internal GPS readings and manually locating on aerial photographs.
The Toshiba tablet running ArcPad, the Samsung tablet running FieldMove and Geopaparazzi, and the GeoXT running Terrasync were all trialled on coastal platform segments immediately north of Akatore Creek. ArcPad, Geopaparazzi, and Terrasync were each run for ≈40 minutes on separate coastal platform segments where structural point measurements of joints, foliation, lineations, and faults were taken. Photographs were taken at some point measurements to test the camera quality and ease of linking photographs to field sites. Sites were located using internal GPS readings and accuracy assessed by comparison to recognizable features on the aerial photography. Due to the inability to recognize the internal GPS unit while using FieldMove only a few manually picked points were made to test feature generation in the program.

Post-field data processing

Data collected on ArcPad was exported directly back to ArcGIS. Images collected on Geopaparazzi could be directly viewed on a desktop or exported and viewed in GoogleEarth. Data could be converted to shapefiles for viewing in ArcGIS through uDig. Data collected on Terrasync was uploaded to GPS Pathfinder Office, a differential correction applied, then exported to a shapefile for viewing in ArcGIS.

C.2 Hardware performance for digital mapping

See Table C.1 for hardware specifications of each device.

Table C.1: Comparison of the key features of the hardware devices that have been tested in the pilot study.

Device	Size (cm)	Screen Size (cm diagonal)	Battery Life (hrs)	GPS Accuracy (± m)	Weight (kg)
Windows 8 tablet	21.3 X 13.6 x 1.1	20.3	14	3*	0.43
Samsung tablet	21.3 x 12.5 x 0.7	21.4	12	3*	0.29
Nomad GPS	17.6 x 10.0 x 5.0	8.9	15	1-3	0.56
GeoXT GPS	23.4 x 9.9 x 5.6	10.7	10	0.75	0.925
Device	Storage (GB)	External Storage Capacity (GB)	Ruggedized	Orientation Sensors	Camera (MP)
Windows 8 tablet	32	64	N	Y	5
Samsung tablet	16	128	N	Y	8
Nomad GPS	6	Y	Y	N	-
GeoXT GPS	2	32	Y	N	5

* Generic minimum locational accuracy of smartphones and tablets from Shaner (2013)

Table C.2: Ranking using a scale of 1 (bad) to 5 (good) of some aspects of the hardware devices (e.g. user-friendliness) based on the experiences of the author during the pilot study.

Device	Developer	Operating System	Screen Size	Robust-ness	Efficiency	GPS Accuracy	Total
Encore Tablet	Toshiba	Windows 8	5	1	3	2	11
Galaxy Tablet	Samsung	Android 4.4	5	3	5	3	17
Nomad	Trimble	Windows Mobile 6.1	3	5	4	4	15
GeoXT	Trimble	GeoXT	3	5	5	5	**18**

The Toshiba tablet runs Windows 8 compared to Android on the Samsung tablet. Both tablets are roughly 21.5 x 13.5 x 1.5 cm (including case) with almost all space given to the screen. Both tablets contain built in cameras and GPS units as well as the ability to connect to the internet, take notes, run windows or android apps, etc A generic stylus can be used but the accuracy and precision of point selection is still diminished compared to other stylus-supported tablets. Both tablets also have exterior cases for shock/scratch protection, the Toshiba tablet case is significantly less ruggedized making the device feel fragile while out in the field. The Samsung tablet case is waterproof while the Toshiba tablet has a separate waterproof case. The Samsung case has some issues, the plastic over the screen bows slightly increasing glare in sunlight and the case is not waterproof while using the camera. The Toshiba waterproof case has significant issues; it is extremely difficult to put on/take off, sun glare becomes a major problem, the camera is partially obscured, and the touch screen is extremely unwieldy through the plastic. Both devices handle opening software well and are relatively easy to navigate with little to no previous experience. One feature which particularly stood out on the Samsung tablet was the keyboard which automatically pops-up when a text field is selected, the Toshiba tablet requires the keyboard to be manually selected from the taskbar and manually closed making forms longer than the screen difficult to scroll through. The internal GPS of the Samsung tablet seemed significantly more accurate ($\pm$ 0.5 m) than the Toshiba GPS ($\pm$ 1.5 m) although it is uncertain how much individual software interact or interfere with that.

Table C.3: Ranking using a scale of 1 (bad) to 5 (good) of some aspects of the software devices (e.g. user-friendliness) based on the experiences of the author during the pilot study.

Developer	Software	Setup Time	User Interface	Efficiency	Versatility	Total
ESRI	ArcPad	1	1	2	5	9
Midland Valley	FieldMove	5	1	3	1	10
geopaparazzi	Geopaparazzi	3	5	5	3	**16**
ESRI	Collector	1	-	-	5	6
Trimble	TerraSync	2	4	5	5	**16**

The Nomad GPS unit designed by Trimble by comparison is 17.6 x 10.0 x 5.0 cm with an 8.9 cm display. The Nomad has a much more ruggedized design compared to the tablets; it is waterproof, relatively shock resistant, and designed with hand straps lending more confidence to its ability to handle an outdoor environment. There is a built in stylus and keypad making precise use relatively convenient. There are still small problems with glare in full sun but overall the Nomad screen is legible in all conditions. However the GPS capability does not appear as accurate as expected from a commercial grade GPS unit ($\pm$ 1 m).
The GeoXT unit, also designed by Trimble, is similar to the Nomad unit with a very ruggedized design including a waterproof, shock resistant case with built in hand straps, stylus, and keyboard. The GeoXT is marginally bigger than the Nomad (23.4 x 9.9 x 5.6 cm). The larger display (10.7 cm) is excellent but the screen can still struggle with glare in full sun. The biggest difference between the GeoXT and all other hardware tested with the GPS accuracy. The GeoXT has a reported accuracy of 0.75 m but in the field was accurate to 0.2-0.3m after differential GPS corrections.

C.3 Software for digital mapping

ArcPad

ArcPad is developed by ESRI specifically for mobile devices. Like ArcGIS desktop there is considerable flexibility in what the program can be used for and the level of complexity that it can handle. However, the cost of this is the lengthy time commitment necessary for setup before commencing fieldwork, particularly if the user is unfamiliar

with ArcGIS. In essence all data fields must be made from scratch in ArcGIS and read/write privileges specified before exporting to an ArcPad readable file type. There is built in capability for creating shapefiles within ArcPad which has not been tested but, given the small size and computing power of a mobile device, I believe it would be difficult to use in the field.

One of the major failings of ArcPad (when used in combination with the either device) is the size of the user interface. Although compromises have been made to enhance usability on small screens (such as drop down menus and removing text), individual icons and text fields are still small making them difficult to select and read. An additional concern with ArcPad is efficiency. The program uses significant computing power that can result in overall slow response of the system, particularly when attaching extra components such as images to feature entries. One notable positive feature about the program was that the GPS reading and calculated accuracy was displayed on the map when outside of feature creation. This allowed for very rapid assessment of potential changes in spatial accuracy in response to real time changes in satellite position and signal interference.

FieldMove

FieldMove, developed by Midland Valley, is a digital mapping environment specifically designed for structural geologists. As such, the setup time has been significantly reduced; all structural features needed for mapping have been built into the program as well as a digital field notebook. The only setup required is uploading a basemap of the area of interest. Unfortunately, uploading a basemap proved to be unexpectedly difficult. Initially a JPEG2000 basemap was uploaded which FieldMove accepted and automatically geolocated using an associated coordinate system conversion file (.prj). However, the program then froze and/or crashed after this step. Next, a TIFF basemap was uploaded but had to be manually georeferenced. FieldMove will accept a wide variety of file types but recommends using a geoTIFF which it should automatically georeference. It is uncertain whether the programs inability to georeference the TIFF provided was due to the way TIFFs are produced in ArcGIS or due to a mistake in file creation on my part. There was no issue uploading the lineament shapefile. An additional problem experienced was the inability of FieldMove to recognize the internal GPS unit, possibly due to internal settings of the tablet.

Aside from the difficulties above, which may stem from problems earlier in the setup process, the largest issue noted with FieldMove itself is the user interface. The program

looks like a desktop application (e.g. very small icons, many icons on the screen at once), which makes navigation extremely difficult on the relatively small tablet screen. A brief attempt at mapping by manually locating sites on the aerial photograph was made and the process was extremely simple, easy to use, and the feature fields very comprehensive. However, it was ultimately undermined by the small size of the icons making accurate selection, placement, and navigation through the program difficult, particularly on a non-stylus-supported device. Valley (2014) claim the software was optimized for tablet devices with stylus-support as well as laptops but do recommend using a device with as much screen space as possible.

Geopaparazzi

Geopaparazzi is an open source program designed by geopaparazzi for surveying. Setup was simple; Hamish Bowman created *mbtiles* and *SQLite* databases which then just needed to be placed in the correct directory for the program to access. This step may present more difficulties to a user who does not have experience creating these file types. The *mbtiles* can then be selected in Geopaparazzi allowing the user to easily switch between different basemaps (e.g. Aerial photography and geologic map).
Geopaparazzi is significantly less versatile compared to the other software being trialled. Users can create three basic types of notes; text, picture, or sketch, all three of which comprise a title and additional information in the form of the note type selected. There is also the option to create a form note that offers the ability to include information of multiple types. Forms are written using json language and must be saved in the master file containing code for all notes. The inherent danger of this system is that there is no easy way to edit or create forms while in the field. Geopaparazzi also offers additional features such as logging a GPS track and sending 'panic' or 'checking in' texts.
It is obvious when using Geopaparazzi that it has been designed specifically for use on a mobile device such as a tablet. All icons are large and the number of icons on the screen has been kept to a minimum making navigation through the program simple. Because of this, the program is significantly more efficient than ArcPad and FieldMove; within the 40 min of field mapping without a customized form for structural measurements I was able to log eleven sites (compared to ArcPad where I was only able to log seven sites). Quick notes about site hazards, contacts between lithologies, and interesting features for further analysis, etc... could also easily be taken while walking through the field area. Geopaparazzi does not offer a constant view of the GPS signal so changes in accuracy may not be immediately apparent. Also there is currently no way to take

polyline measurements but the program is being updated to include this feature in future iterations.

Collector

Collector has not been field tested due to difficulties during setup. Collector is another mobile GIS program developed by ESRI that syncs data via the cloud. All data of interest including custom basemaps and shapefiles must be uploaded to ArcOnline and synced with Collector using an internet connection. Data logging in the field can be done without an internet connection and then synced at a later time when internet is available. Basemaps and other online ArcGIS files created by ESRI or other users may also be included allowing common features to be shared in multiple projects. Data is created on ArcGIS desktop then published as a service to the web. Difficulties in this process were experienced when dealing with large files including high resolution aerial photographs. It is recommended to create a tile package (.tpk) of the basemap in question and directly transfer it to the Collector directory rather than uploading to ArcOnline and downloading onto the tablet.

Terrasync

Terrasync in many ways is Trimble's response to ArcPad by ESRI. It is specifically for mobile devices and can easily be adapted for any type of data collection. Like ArcPad an amount of time is necessary for setting up a data dictionary before commencing fieldwork. Personally I found writing the data dictionary to be easier than setting up the same features in ArcGIS but the popularity of the latter program means that many users will already be experienced with this. However the Terrasync data dictionary does offer a much more intelligent set up allowing users to created nested fields based on 'either or' questions. There is no built in capability for creating new files in the field but generic point, line, and polygon fields are automatically generated and may act as a safety net. The program is also capable of including a photo field within feature generation automatically linking photos taken on the GeoXT to the correct datapoint. Terrasync experiences similar drawbacks to ArcPad in terms of loss of efficiency when negotiating the various screens in the user interface however this is mostly negated by the fact that the GeoXT has such high locational accuracy that constantly checking your location on the basemap is unnecessary. With such confidence in the spatial accuracy a user can simply stay in the data collection screen for the majority of data collection and only deal with refreshing the basemap when comparison to imported

features is desired.

C.4 Digital Compass clinometers

FieldMove Clino

FieldMove Clino is a compass clinometer app designed for smartphones by Midland Valley. According to Valley (2014), since its release in April, 2014, it has proven to be very popular amongst field geologists (10,000+ downloads). The app uses smartphone compass and orientation sensors to measure the orientation of planar and linear features in the field. Field tests showed dip and dip azimuth measurements taken with FieldMove Clino were generally comparable to those taken by a hand-held compass. However, it was noted that FieldMove Clino often required calibration before giving accurate readings and it also takes several seconds to stabilize when taking measurements. Further to this, a recent list discussion on the GeoTectonics mailing list (JISCM@IL, 2014) has raised several important issues regarding sensor accuracy across different platforms and compatibility with different devices. In an uncontrolled experiment (calibration of devices was not required) participants tested measurement of a known orientation using FieldMove Clino on a variety of iPhones and Android smartphones reading a spread of 60°in strike with a best accuracy of ± 5° from true strike. It was assumed the variable quality of smartphone sensors was responsible; for example it was noted the iPhone 4S consistently performed well while the iPhone 5S sensors are well known for being problematic. Finally, it was mentioned that FieldMove Clino is only supported for smartphones and iPads (some users also experienced difficulty getting accurate readings on iPad devices) but no other tablets severely restricting larger-screen options.

C.5 Conclusion

There were pros and cons experienced with all the options looked at in this pilot study. Given that most major lineaments (e.g. faults, veins) had been identified on the basis of aerial photos (Chapter 4), the main aims of structural mapping in this project were to collect orientation measurements from individual locations, and link these to field photos and notes. Based on the pilot study, Terrasync running on the GeoXT was the preferred software-hardware combination for fieldwork (Tables C.2 and C.3). This combination outstrips any of the competition in terms of usability

and accuracy. Geopaparazzi is the only contender in terms of efficiency as the user interface is specifically designed for small screens but the versatility, ruggedness, and high precision of the GeoXT offers users a degree of flexibility and confidence in data quality which is unmatched.

Appendix D

Samples

Table D.1: List of all rock samples collected from Akatore coast and the diferent analytical techniques applied; polished thin section (PS), carbon-coated thin section (SEM), carbon and oxygen stable isotopes (C-Iso) with the final amount of powdered material in µg for dirty samples (C%weight), strontium isotopes, and trace elements.

OBJECTID	Name	Type	Strike	Dip	Dip_dir	Notes	Time	Date	Updated	ddfSource	PS	SEM	Powdered	C-Iso	C%weight	Strontium	Trace elements
12	AK-01		0	0						1	y						
11	AK-02		150	32						1	y	y					
10	Ak-03	Breccia	170	14		Sample site	12:40:12am	2014-10-23	11:40:12am	2	y	y					
5	Ak-04a	Vein	158	12	NE	dipping ne - upper half of sample	03:19:47am	2014-10-30	03:19:47am	3	y	y	y	Y			
5	Ak-04b	Vein	158	12	NE	dipping ne - lower half of sample	03:19:47am	2014-10-30	03:19:47am	3	y	y	y	Y			
6	Ak-05	Breccia	40	36	SE	dipping se	04:00:54am	2014-10-30	04:00:54am	3	y	y					
7	Ak-06	Breccia	328	18	NE	dipping ne	04:12:50am	2014-10-30	04:12:50am	3	y	y					
8	Ak-07	Breccia	46	80	SE	strike of clast alignment, clasts sub vertical dipping se	04:16:13am	2014-10-30	04:16:13am	3	y	y					
52	AK-07s	Schist				Host schist near sample 7	04:16:13am	2014-10-30	04:16:13am		y						
9	Ak-08	Breccia	178	12	E	dipping e	04:48:20am	2014-10-30	04:48:20am	3	y	y					
4	Ak-09	Vein	79	18	SE	Sample site	04:31:55pm	2014-12-13	04:31:55pm	4	y	y					
2	Ak-10	Breccia	84	68	NW	Sample site	12:56:13pm	2015-01-08	12:56:13pm	4	y						
3	Ak-11	Breccia	85	66	SE	Sample site	03:06:43pm	2015-01-08	03:06:43pm	4							
1	Ak-12	Vein	206	42	SE	Sample site	02:15:58pm	2015-02-22	02:15:58pm	4							
49	Ak-13	Vein	0	0		vein in fractures between foliation parallel veins	10:35:04am	2015-04-04	10:35:04am	5			y				
50	Ak-14	Vein	0	0		calcite in low strain breccia	10:41:57am	2015-04-04	10:41:57am	5	y		y	Y			
51	Ak-15	Vein	0	0		foliation parallel vein	10:48:11am	2015-04-04	10:48:11am	5			y	Y			
25	Ak-16	Vein	0	0		quartz calcite vein with green alteration	10:55:55am	2015-04-04	10:55:55am	5			y	Y	~250		
26	Ak-17	Breccia	0	0		low strain breccia + milky calcite	11:02:25am	2015-04-04	11:02:25am	5			y	Y		Y	Y
27	Ak-18	Breccia	0	0		breccia from low relief channel	11:10:11am	2015-04-04	11:10:11am	5			y	Y	~400		
28	Ak-19	Vein	0	0		foliation parallel vein	11:17:00am	2015-04-04	11:17:00am	5			y		~350		
29	Ak-20	Vein	0	0		foliation parallel	11:28:39am	2015-04-04	11:28:39am	5			y		~250		
30	Ak-21	Vein	0	0		milky calcite in e-w vein	11:42:46am	2015-04-04	11:42:46am	5	y		y	Y			
31	Ak-22	Breccia	128	45	S	calcite rich vein	12:40:09pm	2015-04-04	12:40:09pm	5							
32	Ak-23	Breccia	137	70	N	upstanding piece from large breccia zone where nw-se and sw-ne breccia sets cross	12:45:51pm	2015-04-04	12:45:51pm	5			y	Y	~400	Y	Y
33	Ak-24	Vein	0	0		milky calcite in dilational jog	12:55:58pm	2015-04-04	12:55:58pm	5	y		y	Y		Y	Y
34	Ak-25	Vein	0	0		foliation parallel	01:08:00pm	2015-04-04	01:08:00pm	5			y		~250		
35	Ak-26	Vein	0	0		foliation parallel	01:23:28pm	2015-04-04	01:23:28pm	5			y (a,b,c)	Y (a,b,c)			
36	Ak-27	Vein	0	0		foliation parallel milky calcite	01:30:49pm	2015-04-04	01:30:49pm	5	y		y				
13	Ak-28	Vein	0	0		foliation parallel	10:01:23am	2015-04-05	10:01:23am	5			y	Y			
14	Ak-29	Breccia	50	24	E	Sample site	10:26:28am	2015-04-05	10:26:28am	5							
15	Ak-30	Vein	68	86	SE	milky calcite breccia around green quartz vein	10:53:09am	2015-04-05	10:53:09am	5			y	Y			
16	Ak-31	Vein	0	0		milky calcite in jog between joints	11:04:45am	2015-04-05	11:04:45am	5			y	Y			
17	Ak-32	Breccia	86	80	SW	large continuous breccia zone	11:37:30am	2015-04-05	11:37:30am	5			y		~300		
18	Ak-33	Breccia	0	0		from large anastomosing breccia set with some milky calcite	11:55:12am	2015-04-05	11:55:12am	5			y	Y	~300	Y	Y
19	Ak-34	Vein	0	0		foliation parallel	12:23:52pm	2015-04-05	12:23:52pm	5			y	Y		Y	Y
20	Ak-35	Breccia	73	84	NW	long continuous breccia	12:31:02pm	2015-04-05	12:31:02pm	5			y		~350		
21	Ak-36	Breccia	99	76	N	breccia	12:36:09pm	2015-04-05	12:36:09pm	5							
22	Ak-37	Vein	0	0		foliation parallel vein in large channel	12:40:31pm	2015-04-05	12:40:31pm	5			y	Y	~250		
23	Ak-38	Breccia	63	34	NW	breccia in large channel	12:46:06pm	2015-04-05	12:46:06pm	5			y	Y	~250		
24	Ak-39	Vein	0	0		foliation parallel	12:51:27pm	2015-04-05	12:51:27pm	5			y	Y			
37	Ak-40	Vein	0	0		large foliation parallel vein through major breccia zone	10:57:06am	2015-04-06	10:57:06am	5			y	Y		Y	Y
38	Ak-41	Breccia	37	38	E	breccia from large almost gouge zone	11:01:53am	2015-04-06	11:01:53am	5			y	Y	~300		
39	Ak-42	Vein	0	0		quartz calcite vein	11:24:08am	2015-04-06	11:24:08am	5			y	Y		Y	Y
40	Ak-43	Vein	0	0		foliation parallel	11:36:41am	2015-04-06	11:36:41am	5			y (a,b)	Y (a,b)			
41	Ak-44	Vein	0	0		foliation parallel	11:56:41am	2015-04-06	11:56:41am	5							
42	Ak-45	Breccia	66	64	E	breccia at side of channel	12:03:57pm	2015-04-06	12:03:57pm	5							
43	Ak-46	Breccia	23	50	NE	breccia from middle of channel	12:15:15pm	2015-04-06	12:15:15pm	5			y	Y	~300		
44	Ak-47	Breccia	46	66	W	breccia from side of channel	12:23:31pm	2015-04-06	12:23:31pm	5							
45	Ak-48	Vein	0	0		foliation parallel	12:30:07pm	2015-04-06	12:30:07pm	5			y				
46	Ak-49	Breccia	0	0		upstanding continuous breccia	12:41:40pm	2015-04-06	12:41:40pm	5			y	Y	~400		
47	Ak-50	Vein	0	0		milky calcite in breccia zone	01:06:22pm	2015-04-06	01:06:22pm	5	y		y	Y			
48	Ak-51	Breccia	121	62	N	breccia in large (25cm?) offset fault	01:15:13pm	2015-04-06	01:15:13pm	5			y	Y	~400		

Appendix E

Sr Isotope Data

Table E.1: $^{87}Sr/^{86}Sr$ and estimated $^{87}Rb/^{86}Sr$ values of individual sample runs.

Sample	Track #	est $^{87}Rb/^{86}Sr$	$^{87}Sr/^{86}Sr$	Feature type
AK-33	1	0.0001	0.705944	Breccia
	2	0.0016	0.706016	
	3	0.0002	0.705961	
	4	0.0001	0.706041	
	5	0.0003	0.706065	
AK-17	1	0.0150	0.706286	Breccia
	2	0.0259	0.706362	
	3	0.0574	0.706412	
	4	0.0502	0.706401	
	5	0.0005	0.706221	
AK-23	1	0.0373	0.706354	Breccia
	2	0.1481	0.706918	
	3	0.0157	0.706462	
	4	0.0254	0.706257	
	5	0.0004	0.705976	
AK-34	1	0.0001	0.706342	Foliation-parallel vein
	2b	0.0000	0.706059	
	2c	0.0000	0.706115	
	3	0.0000	0.706013	
	4	0.0000	0.706105	
	5	0.0020	0.706266	

AK-24	1	0.0000	0.706315	Botryoidal calcite
	2	0.0000	0.706343	
	3	0.0000	0.706306	
	4	0.0000	0.706383	
	5	0.0000	0.706286	
AK-40	1	0.0001	0.705859	Foliation-parallel vein
	2	0.0002	0.705890	
	3	0.0002	0.705914	
	4	0.0002	0.705816	
	5	0.0002	0.705974	
AK-42	1	0.0007	0.705798	Quartz-calcite vein
	2	0.0001	0.705739	
	3	0.0019	0.705855	
	4	0.0003	0.705884	
	5	0.0003	0.705890	